Optical coherence tomography for quantitative analyses of cerebral vessel morphology and hemodynamics

Wei Wei

A dissertation
submitted in partial fulfillment of the
requirements for the degree of

Doctor of Philosophy

University of Washington
2019

Reading Committee:

Ruikang Wang, Chair

Jonathan Liu

Ying Zheng

Program Authorized to Offer Degree:

Bioengineering

University of Washington

Abstract

Optical coherence tomography for quantitative analyses of cerebral vessel morphology and hemodynamics

Wei Wei

Chair of the Supervisory Committee:

Ruikang Wang

Professor of Bioengineering and Ophthalmology
WRF/David and Nancy Auth Innovator of Bioengineering

Department of Bioengineering

The brain plays a crucial role in life-sustaining activities of human, including consciousness, logical thinking, emotional feeling, memory storage, somatic movement, and communication. As the most complex but least understood organ, brain has attracted rising efforts in science and technology to reveal its functions and mechanisms. However, unlike many other organs, the energy consumption of brain is extremely high, accounting for ~20% of entire metabolism in the living body, well above its weight fraction of ~2% [1]. Moreover, brain has no relevant energy storage capacity, which makes it strongly relies on the continuous supply of oxygen and glucose by

cerebral blood flow [2], as metabolism of glucose is the only source of energy for brain except after prolonged starvation [3]. Therefore, one of the most promising area in brain research is through the cerebral blood supply that fuels the cerebral cell metabolism, i.e. the investigation of the cerebrovascular system.

Optical coherence tomography (OCT) based angiography has developed as one of the most powerful and invaluable tool for fast volumetric imaging of cerebral vasculature *in vivo* [4]–[9]. As one of the earliest proposed OCT angiography techniques, optical microangiography (OMAG) demonstrates high potential in detecting OCT signal variations caused by moving red blood cells down to individual capillaries. To further resolve the quantitative flow information (e.g. the blood flow speed), an OCTA-based velocimetry technique was recently proposed to quantify the capillary blood flow within mouse cerebral cortex [10], and accordingly analyze the cortical capillary transit parameters [11]. The background knowledge of OCT angiography and OCT velocimetry are introduced in chapter 1 of this thesis.

One popular paradigm for understanding the brain energy budget is through neurovascular coupling, which correlates the spatiotemporally varying cerebral blood flow with the metabolic needs evoked by local neuronal activities [12][13]. Nowadays, neurovascular coupling and associated hemodynamic responses have been one of the hottest topic in neuroscience. Taking advantage of the high spatial and temporal resolutions of the OCT velocimetry technique (introduced in chapter 1), the capillary hemodynamics within mouse cerebral cortex, as a key factor in the cerebral oxygen diffusion [14]–[16], is thoroughly investigated and discussed in chapter 2. This chapter describes a couple of new findings about the microvasculature and capillary hemodynamics in neurovascular coupling, including the mean capillary transit velocity, temporal fluctuation bandwidth, and variations of such during electrical stimulation, along with a Monte

Carlo numerical model to simulate the spatiotemporally-coupled capillary transit parameters, allowing for better understanding of the neurovascular coupling and functional hyperemia.

Apart from the capillaries, the penetrating vessels, which bridge the subsurface microvascular bed with the mesh of surface communicating vessels, are usually lack of characterization. Moreover, in contrast to the surface and subsurface vasculatures, the penetrating vessels are highly devoid of anastomoses [17], [18], which makes them the anatomical bottleneck in cerebral blood supply [19], [20]. Clinically, the degeneration and dysfunction of penetrating vessels appear to be direct related to Alzheimer's disease, cerebral amyloid angiopathy, perceptual deficit, and stroke. In chapter 3, we propose a statistical cerebral penetrating vessel mapping approach that is innovatively redesigned from OCT velocimetry. This method allows for automatic quantification of penetrating arterioles and ascending venules from large volume OCT angiography data, and accordingly contributes to the topological and morphological analyses of cortical vasculature in functioning brains.

As the "main street" of the cerebral vascular architecture, the surface communicating vessels play a leading role in the cortical tissue development in both normal and pathological conditions. For instance, the redundancy in cortical surface vessels supports persistent cerebral blood flow [21], and the anastomosis of surface vessels in stroke further protects cortical tissue from ischemic injury [22]. On the other hand, the functioning of the surface communicating vessels is highly related to their morphological properties, including vessel diameter, vessel torutosity, vessel branching angle et. al. In chapter 4, we present a comprehensive framework for quantitative characterization of the cortical surface vessels, with newly-designed methods for automated vessel diameter measurement and vessel tracing. The proposed algorithmic approach is highly adaptable,

and can easily be extended to other imaging modalities, making it of great value in multiple clinical settings.

Other than the cerebral blood flow, as a high-sensitive approach to resolve signal variations, dynamic OCT processing may provide subtle information of cortical cell dynamics. In the future, we plan to image and quantify the subcellular motion of neuron cells in the brain *in vivo*. Some of the preliminary results have been drafted in chapter 6. The successful characterization of cortical cell metabolism and cerebral blood flow with OCT may prove its high potential in future studies of neurovascular coupling.

List of journal publications

Part of this dissertation has been published in the selected journal papers from the list below.

**: equally contributed co-authors

[1] **W. Wei** et al, Dynamic imaging and quantification of subcellular motion with ED variance analysis, *submitted to J. Biophotonics.* (Partly used in Chapter 6 of this thesis)

[2] **W. Wei** et al, Automatic vessel diameter quantification and vessel tracing, *In revision*. (Partly used in Chapter 4 of this thesis)

[3] **W. Wei** et al, Spatial and temporal heterogeneities of capillary hemodynamics and their functional coupling during neural activation, *IEEE Trans. Med. Imaging*, DOI: 10.1109/TMI.2018.2883244. (Partly used in Chapter 2 of this thesis)

[4] **W. Wei** et al, Mapping and quantitating penetrating vessels in cortical brain using Eigen-decomposition of OCT signals and subsequent principal component analysis, *IEEE J. Sel. Top. Quantum Electron*, 25 (1), 1-9, 2019. (Partly used in Chapter 3 of this thesis)

[5] **W. Wei** et al, Automatic motion correction for *in vivo* human skin optical coherence tomography angiography through combined rigid and nonrigid registration, *J. Biomed. Opt.*, 22(6), 066013, 2017.

[6] **W. Wei** et al, Inter-volume analysis to achieve 4D optical micro-angiography for observation of dynamic blood flow, *J. Biomed. Opt.*, 21(3), 036005, 2016. (Partly used in Chapter 1 of this thesis)

[7] **W. Wei** et al, Removal of patterned motion artifacts in *en face* OCT angiography with eigen-decomposition, *In preparation*.

[8] Y. li **, **W. Wei** **, and R. K. Wang, Capillary flow homogenization during functional activation revealed by optical coherence tomography angiography based capillary velocimetry, *Sci. Rep.* 8, 4107, 2018. (Partly used in Chapter 1 of this thesis)

[9] **W. Wei** **, W. J. Choi **, and R. K. Wang, Microvascular imaging and monitoring of human oral cavity lesions *in vivo* by swept-source OCT based angiography, *Lasers Med. Sci.*, 33(1), 2018.

[10] Z. Xie **, **W. Wei** **, P. Tang, and R. K. Wang, Depth-resolved monitoring of pulsatile blood flow *in vivo* with swept source optical coherence tomography angiography, *In preparation*.

[11] J. Xu, **W. Wei**, S. Song, X. Qi, and R. K. Wang, Scalable ultra-wide-field optical coherence tomography based angiography for *in vivo* imaging applications, *Biomed. Opt. Express*, 7(5), 1905, 2016.

[12] S. Song, **W. Wei**, B. Y. Hsieh, I. Pelivanov, T. Shen, M. O'Donnell, and R. K. Wang, Strategies to improve phase-stability of ultrafast swept source optical coherence tomography

for single shot imaging of transient mechanical waves at 16 kHz frame rate, *Appl. Phys. Lett.*, 108(19), 2016.

[13] U. Baran, **W. Wei**, J. Xu, X. Qi, W. O. Davis, R. K. Wang, Video rate volumetric OCT-based angiography achieved by 18 kHz MEMS scanner with 1.6 MHz swept laser source, *Opt. Eng.*, 55(4), 040503, 2016.

[14] Y. Li**, W. J. Choi**, **W. Wei**, S. Song, Q. Zhang, J. Liu, R. K. Wang, Aging-associated changes in cerebral vasculature and blood flow as determined by quantitative OCT angiography, *Neurobiol. Aging*, 70, 148-159, 2018.

[15] J. Xu, S. Song, **W. Wei**, R. K. Wang, Wide field and highly sensitive angiography based on optical coherence tomography with akinetic swept source, *Biomed. Opt. Express*, 8(1), 420, 2017.

[16] M. Redd, N. Zeinstra, W. Qin, **W. Wei**, A. Martinson, Y. Wang, R. K. Wang, C. Murry and Y. Zheng, Patterned human microvascular grafts enable rapid vascularization and increase perfusion in infarcted rat hearts, Nat. Commun., 2019, 10: 584.

[17] Z. Zhi, W. Qin, J. Wang, **W. Wei**, R. K. Wang, 4D optical coherence tomography-based micro-angiography achieved by 1.6-MHz FDML swept source, *Opt. Lett.*, 40 (8), 1779-1782.

[18] S. Men, C. Chen, **W. Wei**, T. Lai, S. Song, R. K. Wang, Repeatability of vessel density measurement in human skin by OCT based microangiography, *Skin Res. Technol.*, 23 (4), 607-612.

[19] C. Methner, A. Mishra, K. Golgotiu, D. Yanez, Y. Li, **W. Wei**, B. V. Zlokovic, R. K. Wang, N. Alkayed, S. Kaul, J. Iliff, Pericyte constriction underlies capillary de-recruitment during hyperemia in the setting of noncritical arterial stenosis, submitted to *Am. J. Physiol. Heart Circ. Physiol.*

Acknowledgements

I would like to thank all my colleagues, collaborators and the entire committee for their help and support during my Ph.D studies.

First and foremost, I wish to express my sincere gratitude to my thesis advisor, Prof. Ruikang (Ricky) Wang, for his great guidance, caring and encouragement. I'm very grateful to him for giving me this chance of learning the state-of-the-art OCT techniques and gaining those invaluable hands-on skills. Additionally, the atmosphere of freedom he built in our lab helped me explore my own research of interests, but meanwhile keep stepping forward without deviation from the main topic. Also, his dedication and passion for scientific research have been a long-term inspiration to me, which motivated me to be innovative and productive.

I would like to show my special thanks to my PhD dissertation committee members who spent their valuable time to review my work. Prof. Ying Zheng instructed me about blood flow mechanics, and opened a wonderful collaboration environment through the microfluidic imaging and cardiovascular imaging projects. Prof. Jonathan Liu and Prof. Dan Fu instructed me about optical imaging and biophysics with their insightful questions, and guided me to think deeply about the clinical applications of our developed techniques. The big picture they guided me to visualize and the skills of logical thinking from a perspective of a scientist will benefit me a lot in my future research career.

Many thanks to my collaborators, lab members and friends who made my life in the university memorable. With Dr. Woo June Choi, Ms. Yuandong Li, Dr. Utku Baran, and Dr. Anthony Deegan, we collaborated a lot on cerebral imaging that led to interesting findings and publications. With Dr. Qinqin Zhang and Mr. Yuxuan Cheng, we always had fruitful discussions about the development of OCT data processing algorithms. Dr. Wan Qin and Dr. Jingang Wang have been

extremely helpful in all aspects, sharing their experiences on both research and life. Dr. Shaozhen Song, Dr. Jingjiang Xu, Dr. Woo June Choi and Dr. Zhongwei Zhi helped me maintain and modify our systems. Ms. Yuandong Li and Dr. Xiaoli Qi provided nice animal cranial window surgery for our *in vivo* experiments. With Kanheng Zhou, Mitch Kirby, Peijun Tang, Zhiying Xie, we've been discussing a lot about our future plans of subcellular dynamics and pulsatile dynamics. Great thanks to Sam Rayner, Caitlin Howard, and Meredith Redd in Prof. Zheng's lab, for their nice collaborations in microfluidic fabrication and animal cardiovascular imaging. I was also very fortunate to work with and learn from experienced clinical researchers Dr. Wenri Zhang, Dr. Wenbin Zhu, Ms. Kirsti Golgotiu, and Prof. Nabil Alkayed from School of Medicine at OHSU, and Dr. Suzan Dziennis, Dr. George Burwood, and Prof. Alfred Nuttall from Oregon Hearing Research Center at OHSU.

I wish to highlight my trainings from my master advisor Prof. Xingyu Zhang in Shandong University, who taught me about identifying, analyzing, and solving research problems in practice. Prof. Dechun Li in Shandong University was also a great mentor who guided me into the early days of research date back to my junior year. My previous colleagues Dr. Shaojie Men and Mr. Fupeng Wang who reunited with me in Prof. Wang's lab have been particularly supporting, and together we made plenty of research progressions.

Finally, my mom Xiaolin Liu and my dad Rongchang Wei deserve my utmost appreciation. They taught me to be decisive and optimistic, even in the most difficult times. I should also thank my beloved wife Dr. Qiurong Shi, who's always there rooting for me, through the good and bad days. I would never make this without their selfless and endless love and support.

To my dear parents and my wife,

Table of contents

List of figures

Figure 6.4. (a) Phantom made by adding yeast suspension into gelatin/TiO_2 water solution before solidification. (b) *En-face* OCT dynamic image of the solidified phantom in the red square in (a), in which the yellow arrows indicate thin-layer yeast clusters peeled off due to surface tension. (c) The OCT structure image crossing the boundary between gelatin/TiO_2 and yeast, in which two regions of interest are respectively marked by green and red squares. (d) Corresponding to the regions, the averaged static power ratios are plotted along the time axis, and exponentially fitted in green and red, respectively. The fitted damping coefficient is -0.088 /s (R^2 = 0.96) for the gelatin/TiO_2, and -0.216 /s (R^2 = 0.97) for the yeast.

Figure 6.5. Dynamic imaging and ED variance analysis of cortical tissue *in vivo* for a mouse brain subject to ischemic injury.

Chapter 1. Introduction

1.1 Optical coherence tomography

Optical coherence tomography (OCT) is a rapid evolving imaging modality with tremendous technological advances in the last two decades. Analogous to ultrasound, OCT performs fast three-dimensional imaging of biological tissue samples by measuring echoes of the back-reflected light, while the resolution of which is in the range of 1-15 μm, one to two orders of magnitude finer than conventional ultrasound [23]. Here, we will introduce the basic principle of OCT, especially the spectral domain OCT that commands the largest OCT market share due to its advantages in system sensitivity and stability.

1.1.1 Principle of OCT

OCT is based on low-coherence interferometry that detects the interference between the back-reflected optical fields. The schematic setup of a typical time domain OCT system (Michelson type interferometer) is shown in Fig. 1.1(a), which is consisted of a broad-band light source, a beam splitter, a reference arm with a mirror, a sample arm with the tissue of interest, and a photodetector.

In the system, light emitted from the source is first divided by the beam splitter into the reference arm and the sample arm. Reflected light from the reference mirror recombined with the back-scattered light from different tissue layers, and then detected by the photodetector. The detected OCT signal can be expressed by the following equation,

$$I(Z) = \rho\langle|E_R + E_S|^2\rangle_\tau, \tag{1.1}$$

where ρ is the quantum efficiency; τ is the integration time; Z is the axial position; E_R and E_S are the optical fields of the reference arm and the sample arm, respectively. As the interference can only be formed when the optical path length difference between two arms is within the coherence

length of the light source, a micrometer-scale axial (depth) resolution can be achieved by adopting sources of wide spectral bandwidth. By axially moving the reference mirror, an interferogram containing a burst fringe-pattern that corresponds to a depth measurement of the tissue sample (A-line) is obtained with each depth position matching its corresponding reference path length, as shown in Figure 1.1(b). However, due to the mechanical movement of the reference mirror, time domain OCT can only reach an A-line rate of ~8 kHz, whose *in vivo* application is therefore highly limited.

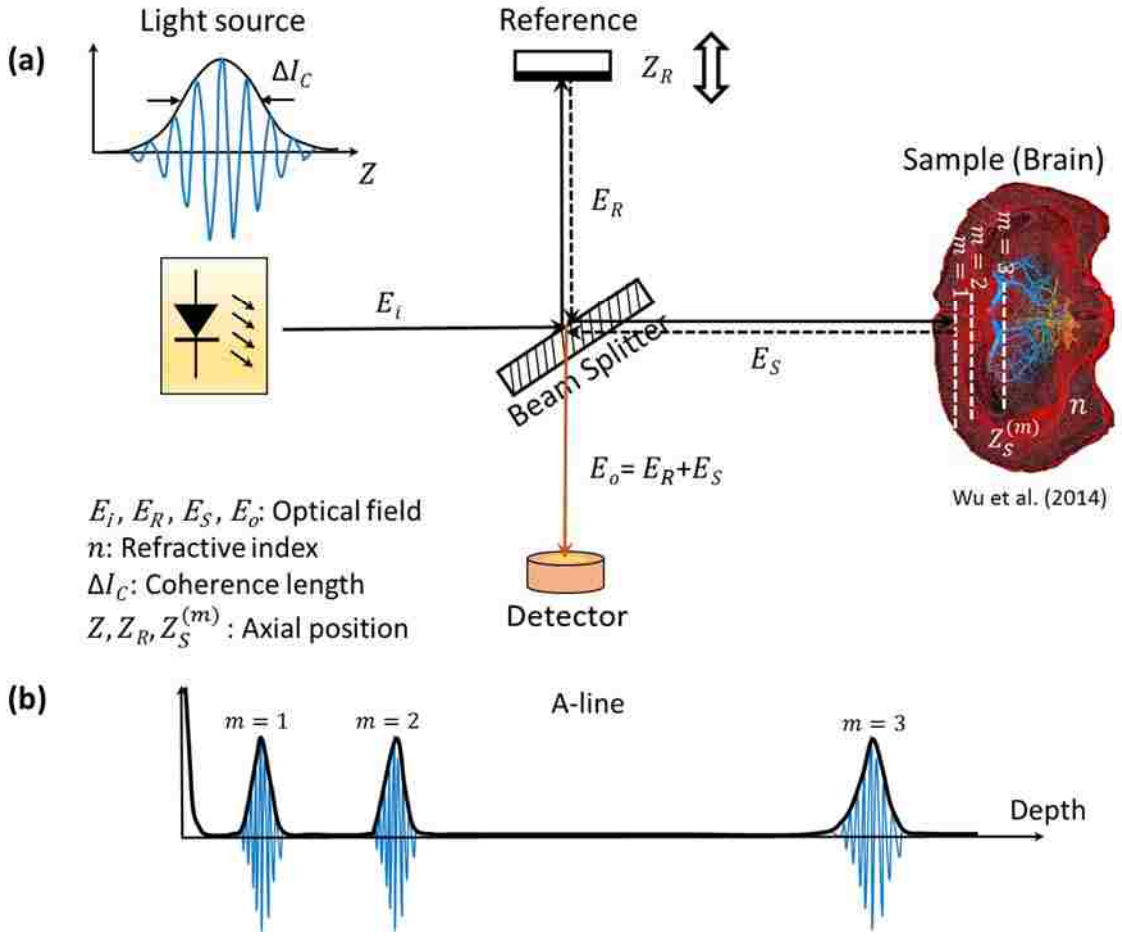

Figure 1.1. (a) schematic setup of a typical time domain OCT system and (b) a representative A-line signal

1.1.2 Spectral domain OCT

Spectral domain OCT (SD-OCT), which shares a similar concept with the time domain OCT, is however capable of extracting the depth-resolved information without any movement of the reference mirror. As shown in Figure 1.2 (a), by replacing the photodetector with a high-speed spectrometer, the depth measurement is directly recorded as a function of the light wavelength, called OCT interference spectrum. In this scenario, equation (1.1) can be rewritten as:

$$I(\lambda) = \rho\langle|E_R|^2 + |E_S|^2 + 2|E_R||E_S| \cdot cos[2n(Z_S - Z_R) \cdot K]\rangle_\tau \quad (1.2)$$

where λ is the light wavelength, and K is the wavenumber that equals to $2\pi/\lambda$. According to equation (1.2), the optical path length difference and the wavenumber K are Fourier transform pairs. Therefore, the A-line signal equivalent to the profile in Figure 1.1(b) can be obtained through fast Fourier transform (*FFT*) of the interference spectrum. The OCT interference spectra of three representative tissue layers and the corresponding depth profile are conceptually illustrated in Figure 1.2 (b). Finally, either in conventional time domain OCT or in spectral domain OCT, two- or three- dimensional (2D/3D) data are generated by laterally scanning the light beam and sequentially piling up multiple depth scans into a cross-section (B-frame) or a volume.

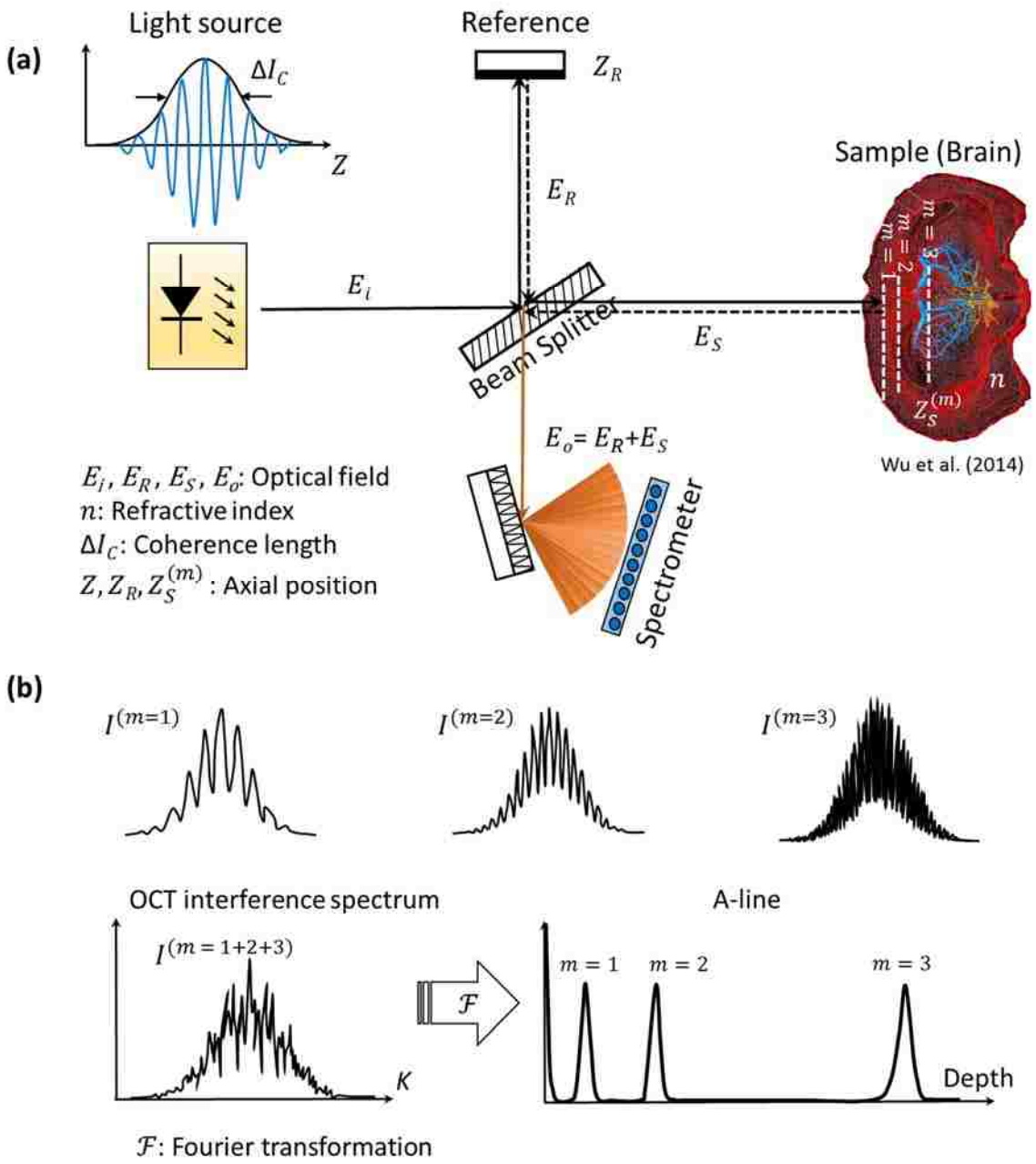

Figure 1.2. (a) schematic setup of a typical spectral domain OCT system and (b) OCT interference spectra of three representative tissue layers and the corresponding depth profile (A-line)

As the speed of SD-OCT is mainly determined by the exposure time of the CCD camera, it can provide an A-line rate of 100 – 200 kHz, much faster than that of the time domain system. Additionally, assuming the system is shot-noise limited, the camera can be regarded as an array of photodetectors with same noise floor (parallel detection). Therefore, in each A-line, the total

number of photons collected in SD-OCT is *M* (number of elements in the detector array) times that of the time domain OCT, resulting in a typical sensitivity advantage of 20 – 30 dB for the former [24]. As compared to another popular OCT setup, the swept source OCT, that requires continuous frequency-tuning in the light source, SD-OCT has a significant advantage in its phase stability due to its stable light source, which is extremely important in the quantitative study of cerebral blood flow and hemodynamics. Therefore, the entire thesis will be based on the development and usage of SD-OCT systems.

1.1.3 Data acquisition in SD-OCT

The data acquisition in SD-OCT is achieved following several main steps as shown in Figure 1.3. Initially, the scanning protocol (including sampling rate, field of view, lateral sample spacing et al.) is designed and used as the system control waveform. Then, 2D/3D data are acquired through synchronously triggering the galvo scanners, the camera, and the frame grabber. As in SD-OCT the interference is split by a grating into different frequency components that are further captured by the line-scan camera. Resampling of the captured data (*K*-space linearization) is required in order to correct for the nonlinear spatial mapping of wavenumbers. A well-accepted method for *K*-space linearization usually involves estimating the phase-frequency relation via Hilbert transformation, calculation of instantaneous phase angle and phase unwrapping [25]. After subtraction of the background and *K*-space linearization, the depth profile of the structural information can be reconstructed by performing *FFT* operation with respect to each A-line.

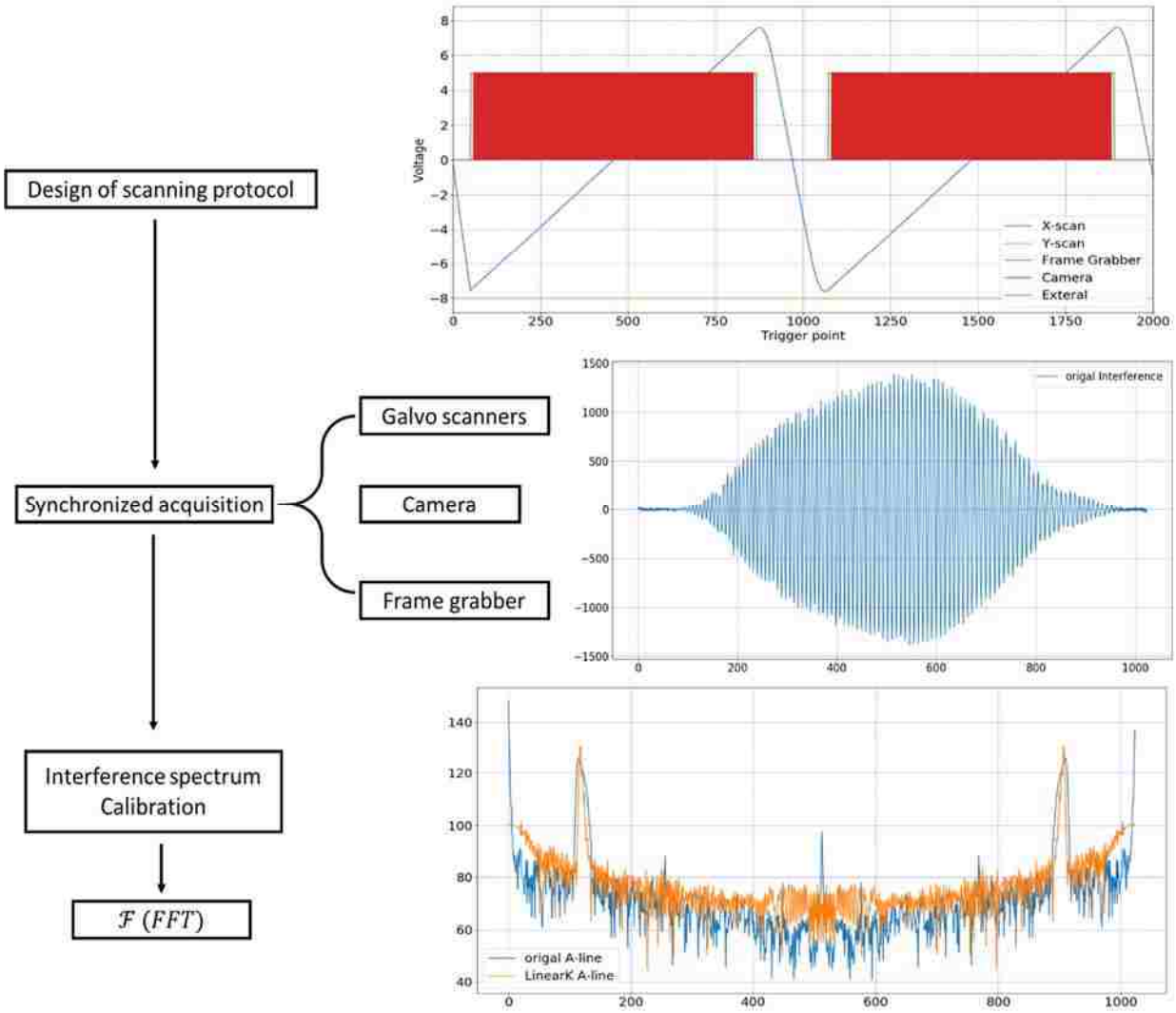

Figure 1.3. SD-OCT data acquisition flow. Right top: scanning protocol; Right middle: a representative background-subtracted interference spectrum; Right bottom: *FFT* of the representative spectrum (blue), *FFT* of the representative spectrum after *K*-space linearization (orange)

1.2 Optical coherence tomography angiography (OCTA)

As a functional extension of OCT technique, OCT-based angiography has been increasingly becoming clinically important due to its ability to provide volumetric microvascular networks *in vivo* without a need of exogenous contrast dyes. Based on repeated scanning (repeated A-lines, B-frames or 3D volumes) and high-pass filtering, numerous OCTA algorithms have been proposed to contrast functional microvasculature in the brain, such as optical micro-angiography (OMAG) [6], [26], speckle variance [27], phase variance [28], and correlation mapping [29]. By using

ultrahigh sensitive OMAG (UHS-OMAG), an unprecedented sensitivity to 4 μm/s was achieved [30]. As with high tolerance to bulk tissue motion (i.e. with no need of phase compensation for bulk motion [31]), a complex OCT signal based eigen-decomposition (ED) clutter filtering algorithm was proposed to effectively suppress the static tissue structure while preserving the flow information [32].

For 3D data acquired by SD-OCT, the temporal resolution of OCTA depends on the camera speed that defines the system A-scan rate, and scanners that dictate how fast the probe beam can be scanned to achieve 3D imaging. On the other hand, the sensitivity of OCT angiography techniques to blood flow measurement is directly related to the time interval Δt for analysis. The shorter Δt translates to a lower sensitivity of flow measurement. In practice, one often selects to use Δt in a range ~2 to 5 ms for angiographic data analysis to contrast slow blood flows, e.g. in capillary vessels, within tissue *in vivo* [33].

1.3 Optical coherence tomography velocimetry (OCTV)

Based on the ED-OCTA technique, a model-based ED-OCTV was proposed to statistically estimate the mean capillary flow velocity (proportional to the mean frequency of the power spectrum of the dynamic blood flow) and the temporal flow fluctuation (proportional to the bandwidth of the power spectrum) from the coherent optical signals.

The frequency analyses were firstly conducted using the covariance matrix R_x of grouped A-line OCT signals expressed as

$$R_x = Expect\{xx^{*T}\} \tag{1.3}$$

where $x = [x(1), x(2), \dots x(N)]^T$ is the repeated complex A-lines with N represents the total number of repeats and T represents the matrix transpose, $Expect\{\}$ is an operation to calculate

expectation; x^* represents the complex conjugate of x. According to discrete Karhunen-Loeve transform (DKLT), the correlation/covariance matrix of x can be decomposed as eigen values λ_i and eigen vectors e_i that represent different frequency components, as expressed by

$$R_x = E\Lambda E^{*T}, \text{ with } \Lambda = \begin{bmatrix} \lambda_1 & 0 & \cdots & 0 \\ 0 & \lambda_2 & \cdots & 0 \\ \vdots & \ddots & \cdots & \vdots \\ 0 & 0 & \cdots & \lambda_{N_D} \end{bmatrix} E = \begin{bmatrix} e_1(1) & e_2(1) & \cdots & e_{N_D}(N) \\ e_1(2) & e_2(2) & \cdots & e_{N_D}(N) \\ \vdots & \ddots & \cdots & \vdots \\ e_1(N) & e_2(N) & \cdots & e_{N_D}(N) \end{bmatrix} \quad (1.4)$$

where Λ is the diagonal eigen value matrix, E is the eigen vector matrix, and N_D is the number of repeated A-lines. On the other hand, the DKLT can be considered as a generalization of conventional Fourier analysis for nonstationary random processes [10]. Therefore, with the static component removed through clutter filtering [34], the power spectrum of the signal (i.e. Fourier transform of the correlation function according to Wiener-Khinchin theorem) can be calculated by the eigen decomposition of the correlation/covariance matrix. The spectral moments ω_k are calculated through first lag-one autocorrelation of the remaining eigenvectors as

$$\omega_k = \frac{FPS/2}{2\pi} \arg\left\{ \frac{1}{N_D - 1} \sum_{m=0}^{N_D-2} e_k^*(m) e_k(m+1) \right\} \quad (1.4)$$

where FPS denotes the sampling frequency, arg{} is calculation of the phase angle, e_k (m+1) and $e_k^*(m)$ are the k^{th} eigenvector from the (m+1)$^{\text{th}}$ A-line and the complex conjugate of the k^{th} eigenvector from the m^{th} A-line. The mean frequency that is related to the mean capillary flow velocity is calculated by a weighted normalization as:

$$\bar{\omega} = \frac{\int \omega_k G(\omega_k) d\omega_k}{\int G(\omega_k) d\omega_k}, \quad (1.5)$$

where $G(\omega_k)$ is the power of corresponding spectrum component. The linear relationship between the measured mean frequency and the mean velocity in individual capillaries have been proved by the quantitative results of designed microfluidic flow channels [10]. Moreover, the bandwidth of the frequency that is related to the temporal flow fluctuation of transit RBCs can be expressed as:

$$\Delta\omega = \sqrt{\frac{\int(\omega_k - \bar{\omega})^2 G(\omega_k) d\omega_k}{\int G(\omega_k) d\omega_k}}. \quad (1.6)$$

Feasibility of these two parameters ($\bar{\omega}$ and $\Delta\omega$) in quantification of cerebral capillary flow have also been demonstrated in [10].

1.4 Scope of the thesis

The objective of my research is seeking OCT solutions for characterizing the cerebral vasculature and hemodynamics, and understanding how the cerebral circulation adapts in different physiological states. The solutions include but not limited to the quantification of blood flow parameters, the numerical modeling of capillary hemodynamics, the statistical analysis of vascular patterns, controlled phantom validations, and the OCTA associated artifact reduction and system development. Specific objectives are achieved through the following aims:

Aim 1: Characterize the cerebral microvascular network and capillary hemodynamics by 1) applying OCTA and OCTV to the microcirculatory tissue bed; 2) quantitatively analyzing the hemodynamic parameters and their correlations; 3) establishing a Monte Carlo simulation model based on the experimental findings; 4) resolving the spatiotemporally-coupled hemodynamics through the control of individual parameters in the simulation model.

Aim 2: Characterize the cerebral penetrating vessel network by 1) developing an innovative penetrating vessel mapping (PVM) approach that eliminates the artifacts in the prior art; 2) integrating the PVM with multiple OCT techniques for comprehensive cerebral diagnosis; 3) applying the developed algorithm to investigate the vasculature remodeling and penetrating vessel adaption after ischemic stroke.

Aim 3: Characterize the cerebral surface vasculature by 1) developing an automatic vessel diameter quantification method that overcomes the drawbacks in current clinically-used approach;

2) developing a modified A* path searching algorithm to trace vessel branches, and accordingly evaluating averaged vessel diameter, vessel tortuosity and bifurcation angle; 3) validating the proposed methods with well-characterized microfluidic flow phantoms; 4) applying the proposed methods to investigate the morphological properties of cortical surface vessels *in vivo*. 5) integrating all the proposed methods into a comprehensive graphic user interface (GUI) platform for OCT angiography vasculature analysis.

Chapter 2. Quantitative investigation of cerebral capillary hemodynamics with OCT velocimetry

In this chapter, the topic of interest is the cerebral capillary blood flow. I will first introduce the basic parameters of capillary hemodynamics and how their changes affect the capillary oxygen extraction during functional hyperemia. By taking the advantages of high temporal resolution of OCT velocimetry discussed in chapter 1 section 1.3, I further investigate the mean RBC velocity and temporal RBC fluctuation, as well as variations within such in the cerebral cortex. In the investigation, statistical correlation analysis and newly designed Monte Carlo simulations (based on the experimental results) are adopted that provides a thorough and quantitative representation of capillary transit characteristics. Although the entire demonstration is on healthy mouse cortex, the proposed quantitively methods can be applied to investigate the hemodynamic responses in cerebral pathological conditions such as stroke and Alzheimer's diseases.

2.1 Introduction

The interwoven nature of capillary network supports crucial functions in tissue metabolism through the exchange of oxygen, substrates, and metabolites with proximal cells. Such functionality can be observed in the brain, when a localized increase in blood perfusion is provoked during neural activation to serve the demands of glycolytic metabolism and oxygen consumption via a complex process termed neurovascular coupling [35]. This interactive hemodynamic response is generally summarized as functional hyperemia, with some controversy surrounding its origin; that is, whether it is regulated through arterioles and downstream capillaries [36], [37] or directly controlled by pericytes [38], [39]. In either case, the increase in cerebral blood flow (CBF) exceeds that of oxygen consumption, meaning the tissue oxygen extraction fraction (OEF) is

decreased whilst CBF increases [40]–[42]. As net oxygen consumption is proportional to the product of OEF and CBF, the reduction in OEF would work to counteract the effects of augmented CBF, suggesting that other factors may be responsible for the metabolic benefits of hyperemia. Moreover, recent report indicated that during activation brain metabolism proceeds even without the increase of CBF, confirming that the metabolism of activated neurons should be attributed to a compensation mechanism in OEF [43]. One explanation suggests that recruitment of previously quiescent capillaries [44] increases the available surface area for oxygen diffusion and consequently reduces oxygen diffusion distance [45], [46]. However, increasing microscopic evidence reveals no capillary recruitment during functional hyperemia, especially in the cerebral cortex [47]–[51]. An alternative theory is established by Jepersen and Østergaard, which describes the relationship between net oxygen extraction, i.e. the product of OEF and CBF, with the use of capillary transit time heterogeneity (CTTH) [14]. In this theory, capillary transit time homogenization, i.e. decreased CTTH, is proposed as a vital mechanism to compensate inherent OEF reduction stemming from augmented CBF and to ensure sufficient capillary oxygen extraction during episodes of hyperemia.

To validate the process of capillary transit time homogenization, a two-photon microscopy-based bolus tracking technique was adopted to quantify changes in the plasma mean transit time and the CTTH during forepaw stimulation [52]. Whilst the premise of the study was positive, the imaging was directly applied to plasma rather than RBC), inevitably introducing measurement flaws [53]. Furthermore, the limited numbers of capillaries that can be imaged with two-photon microscopy and the long acquisition time required to sample multiple capillary segments, hinder the simultaneous investigations of both spatial hemodynamic distributions and temporal

hemodynamic fluctuations. Solving this problem requires a more powerful tool capable of imaging large ensembles of capillaries with high spatiotemporal resolution within a short period of time.

In recent years, the benefits of RBC flux and speed measurements were demonstrated using OCT over a large field of microcirculatory bed [54]–[58], thus giving an opportunity to characterize hemodynamic response for the first time in a more quantitative manner [56]. Li *et al*. investigated the RBC flux at the baseline and during hypercapnia [59], and characterized RBC flux homogenization as the increase of lower end values while upper limit is kept constant. Moreover, RBC flux variability was shown to be proportionate to absolute mean flux. While promising, several concerns have not been fully addressed. 1) The reported relative flux change, whereas indicating the level of variation normalized to baseline flux, could not be directly used to characterize the capillary transit performance because transit heterogeneity is quantified based on the absolute transit time/velocity/flux. 2) The temporal resolution of 667 Hz that was used in the study is not fast enough for mapping temporal fluctuations against flux with the inter-B-frame scanning protocol. 3) The contributions from temporal RBC fluctuations to the OEF, other than those owing to selective flow acceleration, is uncovered.

Here, by taking the advantages of the high temporal resolution (20 kHz) of OCT velocimetry, designed with eigen-decomposition (ED) statistical analysis [10], we investigate temporal RBC fluctuation within mouse cerebral cortex, representing them as temporal fluctuation bandwidths (TFB) of RBC flow velocities. The bandwidth before and during hind-paw electrical stimulations are analyzed to resolve alterations in capillary flow patterns. The results extend our current understanding of spatial and temporal hemodynamics through presenting: 1) during electrical stimulation, both mean capillary transit velocity (mCTV) and temporal RBC fluctuation (i.e. TFB) increase; 2) the degrees of augmentation in mCTV and TFB both negatively correlate with resting

mCTV, with TFB also negatively correlating with resting TFB. Furthermore, a spatiotemporal-coupled Monte Carlo model is constructed to simulate the hemodynamic behavior and the changing processes of CTTH during neural activation, highlighting the increase of mCTV and TFB as the driving force. Our results indicate that the heterogeneous acceleration of flow speed and the heterogeneous increase of temporal fluctuation synergistically diminish the spatial CTTH; therefore, ensuring sufficient oxygenation during functional hyperemia.

2.2 Materials and Methods

2.2.1 Phase stable OCT system and imaging protocol

To acquire the complex OCT signals that carry information about mCTV and TFB, a phase stabilized spectral domain OCT system was employed [10]. Briefly, the system comprised a super luminescent diode with a central wavelength of 1340 nm and a bandwidth of 110 nm, which provided an axial resolution of ~7 μm. For resolving microscale tissue features, a 10X objective lens was adopted in the sample arm that provided a lateral resolution of 7 × 7 μm, the full width at half maximum (FWHM). The angiographic image was acquired using an ultrahigh sensitive OMAG protocol [60], which consisted of 400 A-lines along the fast axis (X) at 92,000 A-lines/sec, and 3,200 B-frames along the slow axis (Y) at 180 frames/sec with 8 repeated cross-sectional scans per location, covering a field of view of 3.5 × 3.5 mm. With capillary velocimetry, for balancing the trade-off between temporal sensitivity and temporal resolution [6], [57], the acquisition speed was set to 20,000 A-lines/sec, and 50 repeated A-lines were acquired at each of the pre-assigned 200 × 100 lateral positions, covering a field of view of 1.5 × 0.75 mm (X × Y).

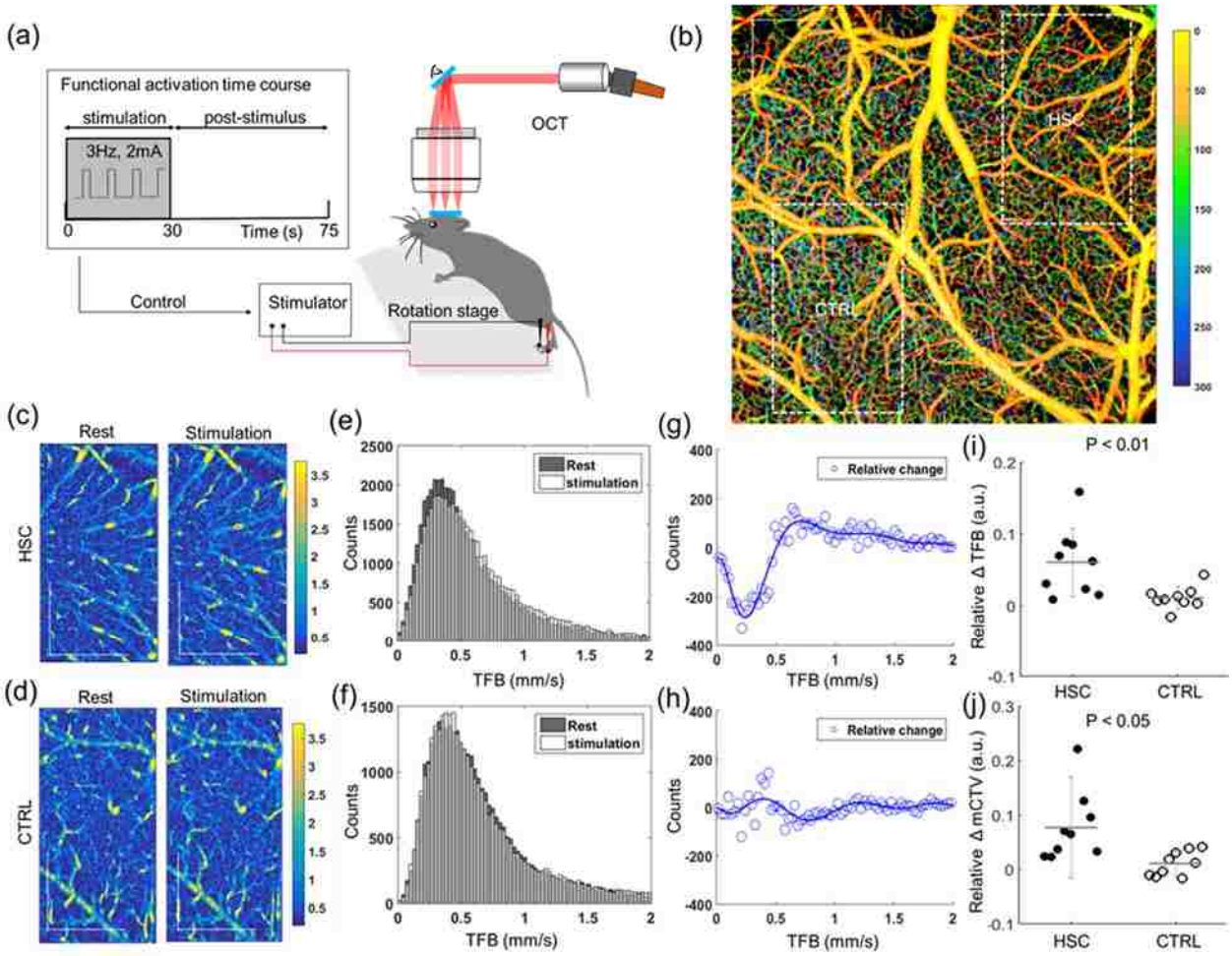

Figure 2.1. Temporal fluctuation bandwidth (TFB) of the capillary blood flow within activated cortical region increases during electrical stimulation. (a) Schematic diagram of imaging during electrical stimulation. (b) A representative 3.5 × 3.5 mm *en face* vascular image, showing a responsive somatosensory cortex region (HSC) and a non-responsive control region (CTRL), in white boxes respectively. The image is generated by projecting the vessels onto x-y plane from 0 mm to 300 um in depth from the cortical surface. (c) and (d), the velocimetry maps of TFB displaying the temporal heterogeneities before (rest) and during (stimulation) neural activation in HSC and CTRL, respectively. (e) and (f), The histogram distributions of TFB from selected regions, with additional blue scatters and polynomial fitted curves indicating shifts in bandwidth distributions after stimulation as in (g) and (h), respectively. (i) Relative changes in TFB at the HSC and CTRL regions of each animal. The statistical difference reaches a significance level of $P < 0.01$. (j) Relative changes in mCTV at the HSC and CTRL regions of each animal. The statistical difference reaches a significance level of $P < 0.05$. In (i) and (j) each dot represents an individual animal, and the horizontal bar represents the mean with standard error. All scale bars represent 500 μm. a.u.: arbitrary unit.

2.2.2 Animal preparation and neural activation

The animal experiments outlined here were approved and supervised by the IACUC committee at the University of Washington. Please refer to [11] for the detailed procedures and protocols for animal handling and neural activation. In brief, C57BL/6 mice (n = 9, male, ~2 months, ~25 g)

were prepared via cranial window surgery under isoflurane anesthesia and investigated at resting state and during functional activation. As shown in Figure 1(a), the activation was evoked by applying an electrical stimulus (repetition rate 3 Hz, amplitude 2 mA, duration 0.3 ms) to the left hind-paw of the mouse over a period of 30 sec. Correspondingly, the contralateral hind-paw somatosensory cortex (HSC) was imaged through our velocimetry scanning protocol, with an additional acquisition procedure being carried out on a control region (CTRL) away from the HSC. The detection and justification of these two regions were also detailed in [11] by using laser speckle contrast analysis of tissue oxygenations. To avoid potential interference from long-term stimulations, a 20-min recovery time was assigned between data-collections at HSC and CTRL regions while the animals were kept anesthetized.

2.2.3 Optical micro-angiography and vessel area density

The delineation of flow signals, i.e., OMAG imaging, was realized through regression filtering to remove a number of eigenvalues (first two in this work) that represent the static components [32]. This flow signal extraction method can be applied to either the typical angiography datasets through inter-B-frame analysis or the velocimetry dataset through inter-A-line analysis. *En face* angiograms were obtained by maximum intensity projection of the morphological flow signals onto the X-Y plane. We calculated vessel area density (VAD) [61] based on *en face* angiograms derived from velocimetry datasets. In brief, VAD was calculated as the percentage of area occupied by vessels with respect to the entire scanned region (200 × 100 pixels) [61]. For visualization purpose, the mapping of VAD was further accomplished by pixel-wise shifting a sampling window with 25× 25 pixels, calculating VAD in each window, resizing the calculated map to its original size, followed by spatial Gaussian smoothing with a kernel size of 3 × 3 pixels. The window size

and the smoothing kernel size were empirically selected to balance the lateral sample spacing and the total sample numbers.

2.2.4 Capillary velocimetry analysis

The inter-A-line capillary velocimetry analysis was achieved by representing a collective of OCT signals as eigenvalues and eigenvectors, and evaluating the frequency of moving RBCs through first lag-one autocorrelation of corresponding eigenvector pairs, as detailed in chapter 1 (equations (1.4) – (1.6) are rephrased here for the consistency of this chapter). Briefly speaking, the mean frequency is written by a weighted normalization:

$$\bar{\omega} = \frac{\int \omega_k G(\omega_k) d\omega_k}{\int G(\omega_k) d\omega_k}, \tag{2.1}$$

where ω_k is the spectral moment derived from the k^{th} eigenvector and $G(\omega_k)$ is the power of corresponding spectrum component. The ω_k can be derived by lag-one autocorrelation of the eigenvector pairs as:

$$\omega_k = \frac{FPS/2}{2\pi} \arg\left\{\frac{1}{N_D-1}\sum_{m=0}^{N_D-2} e_k^*(m) e_k(m+1)\right\} \tag{2.2}$$

in which *FPS* represents the sampling frequency (*FPS* = 20,000 Hz), arg{} is an operation that evaluates the phase angle, N_D is the number of repeated A-lines (N_D = 50), e_k (m+1) and $e_k^*(m)$ respectively represent the k^{th} eigenvector from $(m+1)^{\text{th}}$ A-line and the complex conjugate of k^{th} eigenvector from m^{th} A-line. Moreover, the movement of RBCs is a time-varying signal. The bandwidth of the power spectrum that is related to the temporal heterogeneity of transit RBCs can be expressed as:

$$\Delta\omega = \sqrt{\frac{\int (\omega_k - \bar{\omega})^2 G(\omega_k) d\omega_k}{\int G(\omega_k) d\omega_k}}. \tag{2.3}$$

On the ground of Brier's reconciliation theory that dynamic speckle signal is equivalent to laser Doppler [62], the mCTV ($\bar{v}$) and the TFB (σ) are directly proportional to the mean frequency of the dynamic OCT signal ($\bar{\omega}$) and its power spectral bandwidth ($\Delta\omega$), respectively:

$$\bar{v} = \rho\bar{\omega}\ , \tag{2.4}$$

$$\sigma = \rho\Delta\omega\ , \tag{2.5}$$

in which the scale factor ρ is empirically selected as 0.002 mm according to a phantom experiment [10]. Variations or changes in mCTV and TFB are calculated by subtracting resting state parameters from those of the stimulated, and the relative changes are obtained by further normalizing variations against the resting parameters.

2.2.5 Spatial distribution of capillary transit time

Here we adopt the theory in previous modeling study [14] to parameterize the probability density function of the spatial capillary transit time distribution, expressed as:

$$f(\bar{t}) = \frac{1}{b^a\Gamma(a)}\,\bar{t}^{\,a-1}e^{\frac{-\bar{t}}{b}}, \tag{2.6}$$

where $\Gamma(a)$ represents a complete gamma function; *a* and *b* represent the shape parameter and the scale parameter, respectively. Then, the averaged capillary transit time is determined as ab, and the CTTH (i.e. the heterogeneity of transit times among multiple capillary paths) is quantified by the standard deviation $\sqrt{a}b$ [14], [52].

2.3 Experimental findings

2.3.1 Temporal fluctuation bandwidth increases during electrical stimulation

OMAG imaging was first performed to visualize the 3D cerebral vascular networks within cortex for each animal at resting state. A representative vascular OMAG map is shown in Figure 1(b) that was depth-color coded to 300 μm below the cortical surface, where the responsive region (HSC) and non-responsive control region (CTRL) to the hind-paw stimulation are highlighted by white boxes for comparative purposes. Then, the animal was subjected to the electrical stimulation protocol. TFB of the HSC and CTRL at resting state and under stimulation are respectively mapped in Figs. 1(c) and 1(d). Figs. 1(e) and 1(f) display the histogram distributions of TFBs, with relative changes displayed as hollow scatters in Figure 1(g) and 1(h), respectively. A reduction in lower TFB counts (TFB < 0.5 mm/s) and an increase in higher TFB counts (TFB > 0.5 mm/s) are visualized in the HSC region, whereas the trend in the CTRL region remains almost constant.

Figure 2.1(i) summarizes relative changes in temporal bandwidth at both the specified regions. Taken together, there is an average of 6% increase in TFB at the HSC region (0.72 to 0.77 mm/s) through the electrical stimulation, whereas no increase (0.72 to 0.73 mm/s) was seen at the CTRL region. Statistical analysis (paired *T*-test) shows a significant difference between the HSC region and the CTRL region ($P < 0.01$). A similar significant difference ($P < 0.05$) was observed for the mCTV as displayed in Figure 2.1(j), in which an average increase of 7.7% (1.30 to 1.40 mm/s) was obtained at the HSC region compared with a negligible change of 1.33 to 1.35 mm/s at the CTRL region.

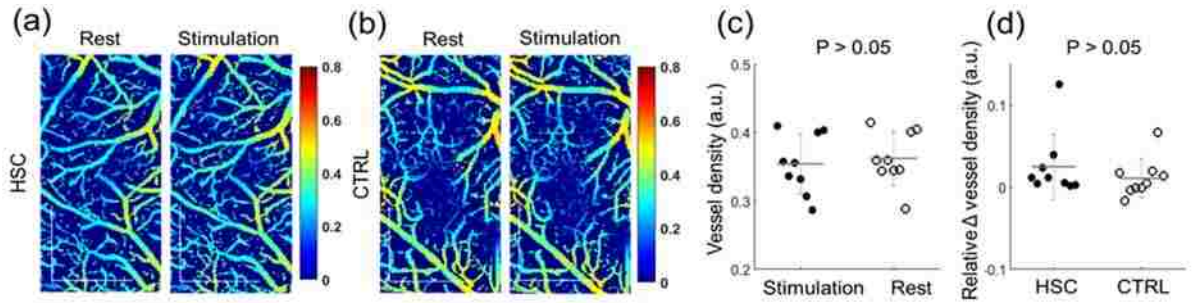

Figure 2.2. Electrical stimulation does not involve the capillary recruitment. (a) and (b) Representative vessel density maps, corresponding to Figure 1 (c) and (d), showing no visible capillary recruitment in either HSC or CTRL regions. (c) Statistical analysis of vessel density comparing resting and stimulated states in the HSC regions of each animal ($p = 0.15$). (d) Statistical analysis of relative changes in vessel density for inter-region comparisons between the HSC and CTRL regions of each animal ($p = 0.45$). In (a) and (b), the colorbar represents the quantified vessel area densities. In (c) and (d), each dot represents an individual animal, and the horizontal bar represents the mean with standard error. All scale bars represent 500 μm. a.u.: arbitrary unit.

2.3.2 Electrical stimulation-evoked functional activation involves no capillary recruitment

Although the capillary recruitment theory [45] has been known for some time now, recent microscopic evidence reveals that the role of the capillary bed is promoted without *de novo* recruitment of previously quiescent capillaries [44]. Here, we observed no change in VAD, as presented in Figure 2(a) and (b) for the HSC and CTRL regions, respectively. Statisitical analyses corroborate these findings, as shown in Figure 2(c) and (d), and in the paired *T*-test: $p = 0.15$ (>> critical value of 0.05) by comparing resting and stimulated states at the HSC region; $p = 0.45$ (>> critical value of 0.05) by comparing relative changes in vessel density between the HSC and CTRL regions. This observation is also supported by a study conducted by Göbel *et al* [63].

2.3.3 Changes in TFB correlate linearly with those in mCTV

Figure 2.3(a) shows the coordinated scattering plot of the changes in TFB with the changes in mCTV at the HSC region, in which four quadrants separately stand for the characteristics of capillary flow: I, both mCTV and TFB increase; II, mCTV decreases but TFB increases; III, both mCTV and TFB decrease; IV, mCTV increases but TFB decreases, with population probabilities of 44%, 15%, 29% and 12%, respectively. Comparatively, a scattering distribution at the CTRL

region is shown in Figure 3(b), with quadrant distribution probabilities of 38%, 12%, 37% and 13%, respectively. One noticeable phenemenon is that the population correlation coefficients (Corr) indicate a strong linear relationship between changes in mCTV and TFB in both HSC and CTRL regions (Corr = 0.64, $P < 0.01$ for both). Additionally, in accordance with Figure 1, the changes appear to favor the HSC region with a population in quadrant I outnumbering that of III by ~15%; in contrast, the CTRL region is more homogeneous with only a difference of ~1%. With that, continued exploration into stimulation-evoked changes in TFB and mCTV via further data mining was applied to the HSC region only.

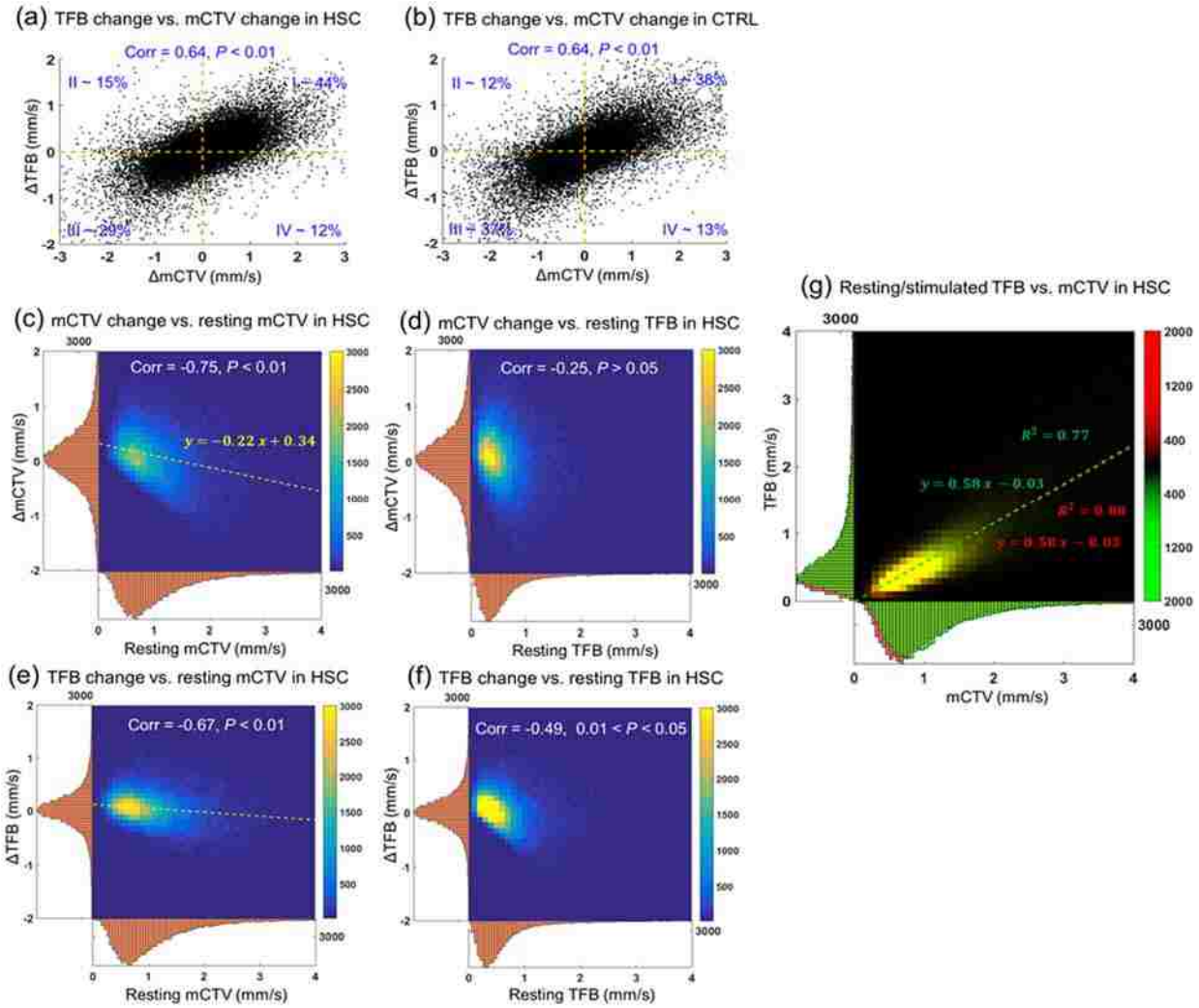

Figure 2.3. Statistical analysis of correlations between temporal fluctuation bandwidth, capillary transit velocity, and the changes of such during stimulation. (a) and (b) The distributions of TFB change along with mCTV change in the

HSC and CTRL regions, respectively, in which four quadrants (I, II, III, IV) denote the distribution probabilities within the region. The population correlation coefficient (Corr = 0.64) indicates a strong linear relationship between samples with a *T*-test probability of $P < 0.01$. Velocimetry data from the HSC region are further mined and presented in (c) – (g). In (c) – (f), histogram distributions of mCTV changes, TFB changes, resting state mCTV, and resting state TFB are respectively plotted in orange. (c) The joint distribution of mCTV changes against resting state mCTV showing a negative correlation (Corr = -0.75, $P < 0.01$). (d) The joint distribution of mCTV changes against resting state TFB showing no significant correlation (Corr = -0.25, $P > 0.05$). (e) The joint distribution of TFB changes against resting state mCTV showing a negative correlation (Corr = -0.67, $P < 0.01$). (f) The joint distribution of TFB changes against resting state TFB showing a negative correlation (Corr = -0.49, $P < 0.05$). (g) The histogram distributions of TFB at rest (red) and during stimulation (green) against those of mCTV. The joint distributions for rest and stimulation are color coded into red and green channels, respectively, with the yellow color indicating overlap. The linear fittings of data before and after stimulation marked by red/green perforated lines denote that TFB is proportional to mCTV for any state. R^2 represents coefficient of determination. Each scatter in (a) and (b) represents a spatial capillary sample. Colorbar in (c) – (g) represents the counts of capillary samples.

2.3.4 Changes in mCTV negatively correlate with resting state mCTV

Figure 2.3(c) is a histogram distribution of mCTV changes with regard to resting state mCTV (coded in orange), as well as their joint population distributions (coded in parula colormap). Consistent with the trend noted by Li *et al*. [59], during electrical stimulation, lower mCTV values in resting state increased while upper values remained relatively unchanged; thereby forming a significant negative correlation (Corr = -0.75, $P < 0.01$) between mCTV changes and resting state mCTV. These heterogeneous velocity augmentations ultimately result in spatial capillary transit velocity homogenezation, contributing to the maintainence of OEF[14]. Yet, a statistically relevent connection between mCTV changes and resting state TFB (Corr = -0.25, $P > 0.05$) can not be established, as shown in Figure 3(d).

2.3.5 Changes in TFB negatively correlate with both the mCTV and TBF at the resting state

Similar to changes in mCTV, alternations in TFB also showed strong negative correlation with the mCTV (Corr = -0.67, $P < 0.01$) at the resting state, with the majority of bandwidth broadening occurring at a speed below the averaged mCTV, as shown in Figure 3(e). In addition, TFB alternations also show negative correlations to the TFB at the resting state (Corr = -0.49, $P < 0.05$), as shown in Figure 3(f).

2.3.6 TFB is proportional to mCTV at the resting state and with this trend continuing during activation

Figure 2.3(g) displays the histogram distributions of absolute mCTV and TFB at rest (red) and during stimulation (green). Compared with the increased average TFB (0.05 mm/s, from 0.72 to 0.77 mm/s), the average mCTV across the whole capillary bed presents a twofold elevation (0.10 mm/s, from 1.30 to 1.40 mm/s). However, relative changes in mCTV and TFB are comparable. Joint distributions during resting and stimulated states are color coded into red and green channels, respectively, with the overlap coded in yellow, in which linear fittings are adopted to denote the direct proportion between mCTV and TFB either at rest (slope = 0.58, R^2 = 0.80) or during stimulation (slope = 0.58, R^2 = 0.77). The correlating changes between mCTV and TFB (Corr = 0.71, $P < 0.01$) further begs for the question: in addition to the contribution of heterogeneous flow acceleration, is heterogeneous bandwidth broadening associated with oxygen extraction during functional hyperemia?

2.4 Monte Carlo simulation for spatiotemporal-coupled capillary transit parameters

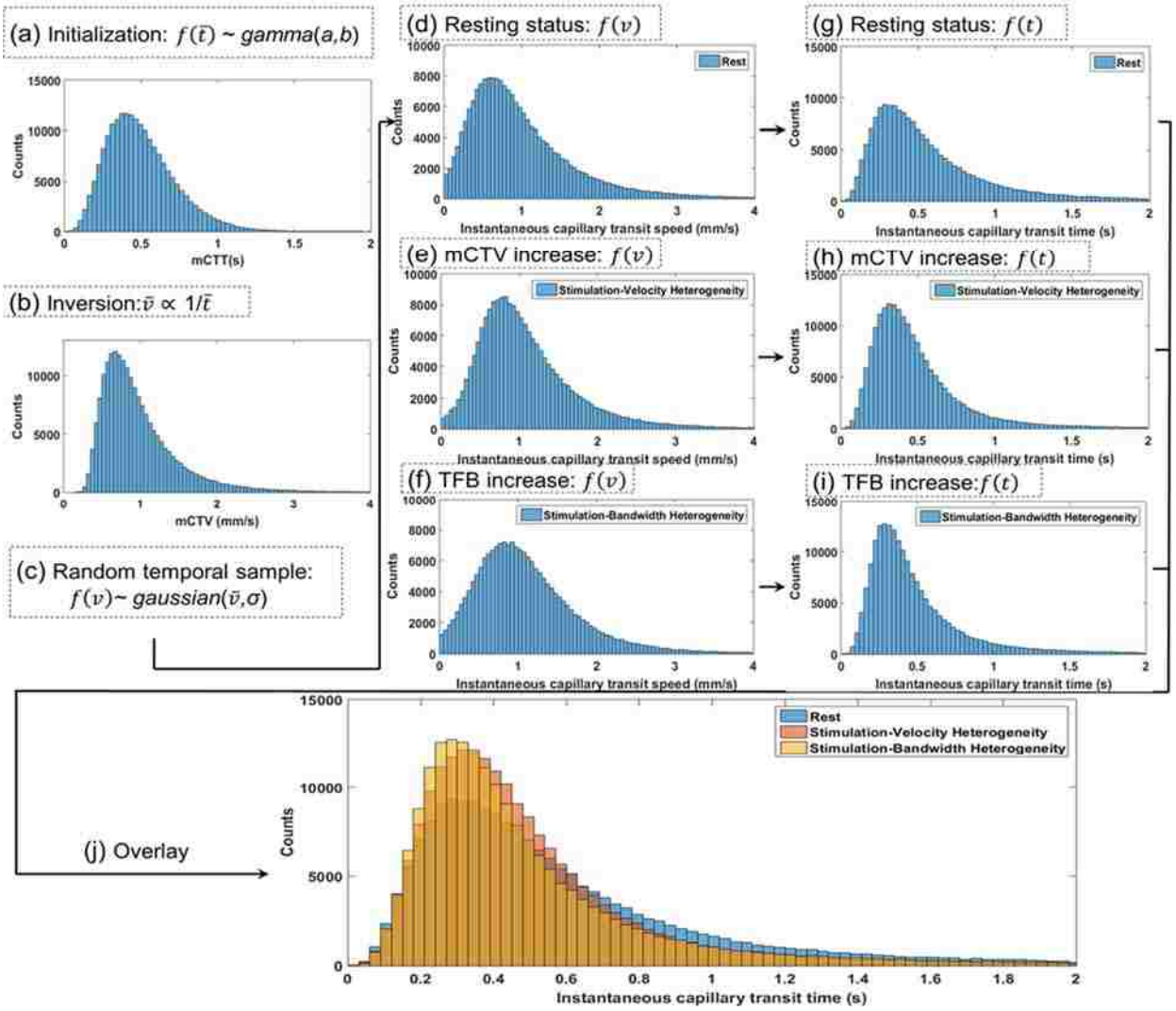

Figure 2.4. Monte Carlo simulation reveals the contributions of capillary transit velocity and temporal fluctuation bandwidth to capillary transit time homogenization during stimulation.

To characterize the synergistic behavior of mCTV and TFB during stimulation, we applied a Monte Carlo simulation to those transit parameters as an extension to the current capillary transit time homogenization model [14]. As the hemodynamic behavior is spatially and temporally coupled in *in vivo* experiments, here the simulation would be useful to separately investigate the contributions of mCTV and TFB on the spatial distributions of capillary transit time. The simulation flow chart is listed in Figure 4. A total sample size of 200,000 positions is selected, corresponding to 10 simulated animals with 200 × 100 positions in each.

Initially, we derive two (spatial and temporal) universal distributions for the capillary transit speed regardless of the resting/stimulation states. First, the spatial distribution of mean capillary transit time (mCTT or $\bar{t}$) is parameterized through the gamma probability density function in equation (2.6). Second, we use the inverse proportion between mCTV ($\bar{v}$) and $\bar{t}$ with a constant capillary transit path L = 0.4 mm [14], expressed as:

$$\bar{v} = L/\bar{t}, \tag{2.7}$$

to describe the spatial mCTV as an inverse gamma distribution. The obtained distribution histograms of $\bar{t}$ and $\bar{v}$ are plotted in Figure 4(a) and (b). Third, we assume a temporal Gaussian process for the instantaneous capillary transit speed (v) [64], expressed as:

$$f(v) = \frac{1}{\sqrt{2\pi\sigma^2}} e^{-\frac{(v-\bar{v})^2}{2\sigma^2}}, \tag{2.8}$$

where σ represents the TFB. Consequently, random events of v can be generated when σ and $\bar{v}$ are known.

Subsequently, by substituting a = 5 and b = 0.1 into equations (2.6) and (2.7), a population of resting state mCTTs ($\bar{t_r}$) and mCTVs ($\bar{v_r}$) can be simulated. Those initial parameters (a and b) are selected according to previous publications [11], [14], where most of the mCTTs are around 0.5 and the CTTHs are about 0.25. Furthermore, based on our experimental results showing that σ is proportional to $\bar{v}$, while the TFB variations ($\Delta\sigma$) and mCTV variations ($\Delta\bar{v}$) are negatively correlated to $\bar{v_r}$, a series of linear approximations are added to calculate mCTV during stimulation ($\bar{v_s}$), bandwidth at resting state (σ_r) and during stimulation (σ_s) from the simulated $\bar{v_r}$, as follows:

$$\bar{v_s} = \bar{v_r} - \alpha \cdot \bar{v_r} + \beta, \tag{2.9}$$

$$\sigma_r = \gamma \cdot \bar{v_r}, \tag{2.10}$$

$$\sigma_s = \gamma \cdot \bar{v_s}, \tag{2.11}$$

where $\alpha = 0.2$, $\beta = 0.3$ and $\gamma = 0.5$ are assigned empirically according to the fitting lines in Figs. 3(c) and (g). It's worth noting that the same proportion coefficient γ is utilized for both rest and stimulation, and here $\gamma < 1$ guarantees that σ_r and σ_s vary slower than $\overline{v_r}$ and $\overline{v_s}$.

By gradually changing the temporal distribution parameters from ($\overline{v_r}$, σ_r) to ($\overline{v_s}$, σ_r) and to ($\overline{v_s}$, σ_s), we obtain the instantaneous capillary transit speed and delineate the speed distribution for the resting state (Figure 4(d)), the distribution with consideration of heterogeneous flow acceleration (Figure 4(e)), and the distribution that considering heterogeneous bandwidth broadening (Figure 4(f)). By re-using the inverse relation in equation (2.7), the corresponding instantaneous transit time distributions were respectively calculated and displayed in Figs. 4(g) – (i). For comparison purpose, we overlay the distributions in (g) – (i) resulting in Figure 4(j), in which a capillary transit time homogenization is achieved mainly ascribed to coordinated alterations in mCTV (pink) and TFB (yellow).

The averaged capillary transit parameters, including those of mCTV ($\bar{v}$), TFB (σ), instantaneous transit speed (v), instantaneous transit time (t) and instantaneous spatial CTTH (δ), are listed in Table 2.1. First, together with the 10% mCTV increase during stimulation, the instantaneous transit speed increases ~ 10% and the instantaneous transit time decreases ~14%. Second, stemming from broadening of the temporal bandwidth, the averaged TFB increases ~10%. Consequently, the first factor contributes a 16% reduction in CTTH and the latter factor contributes an additional 13% reduction. Therefore, the functional benefits of spatiotemporal-coupled hemodynamic changes during hyperemia are interpreted through a decoupled step-by-step capillary transit time homogenization process that ensures sufficient cerebral oxygen delivery [14].

Table 2.1: The averaged capillary transit parameters in the Monte Carlo simulation

Capillary transit parameters	Rest	Velocity heterogeneity	Bandwidth heterogeneity
$\bar{v}$ (mm/s)	0.9987	1.0990	1.0990
σ *(mm/s)*	0.4994	0.4994	0.5495
v *(mm/s)*	0.9981	1.0986	1.1019
t *(s)*	0.5572	0.4809	0.4789
δ *(s)*	0.3401	0.2848	0.2488

2.5 Discussion and conclusion

Previous study using ED-based velocimetry analysis has revealed the phenomenon of capillary flow homogenization (spatial velocity heterogeneity reduction) during neural activation in mouse brain, which supports the important role of microcirculatory adjustment in brain oxygenation along with functional hyperemia [11]. However, temporal fluctuation patterns in capillary vessels, which is critical to achieve the flow homogenization, was not included. In this study, we investigated cerebral capillary hemodynamics and its spatiotemporal adjustment during neural activation *in vivo* through mCTV, TFB, and variations within such. Our capillary velocimetry analyses prior to and during stimulation have demonstrated a concurrent increase in mCTV and TFB due to functional hyperemia arising from metabolically-demanding neural activities, consistent with previously published literature [13], [65]–[68]. Here, we have taken advantage of the high spatial and temporal resolution of OCT velocimetry (~50 μs), much faster than previously reported (milliseconds range) [59], [65], [69]. Consequently, one can expect more accurate velocity measurements in this study because of the higher upper limits for measurable velocities, according to the theoretical analysis discussed by Choi *et al* [70]. Additionally, total dwelling time at each spatial location was just 2.5 ms, which is short enough to exclude any possible motion artifacts due to respiration (261–750 ms) and/or heartbeat (71–194 ms)[21].

Further correlation analyses revealed that temporal fluctuations were proportional to transit velocity during both resting and stimulated states, with growth rates for both velocity and

fluctuation bandwidth negatively correlating with resting state mean transit velocity. On this foundation, linear approximations of resting TFB, stimulated TFB, and stimulated mCTV with regard to resting mCTV were used to model spatiotemporal-coupled transit parameters through a Monte Carlo simulation [71]. The linear approximations were made on solid experimental bases and the simulated results correlated well with experimental data. Although promising, the exact relationship between said parameters has not yet been fully explored. For instance, the saturation effect of high mCTV flow during activation may introduce nonlinear dependence [59], and the fact that cerebral functional connectivity regulates regional capillary blood flow in the brain [72]–[74] may add complexity with possible uncertainties. These correlations should be rigorously investigated in future studies.

It is noted that certain limitations do exist in the current experimental setup. First, due to system sensitivity fall off along the imaging depth and Rayleigh optical focusing, the OCT signal and subsequent velocimetry signal diminished along the imaging depth, degrading the lateral resolution for those capillaries that are out of the focus. This consequently limited our research scope to the superficial cortex (~300 μm, corresponding to layers I – III). Second, inhalational anesthetic (e.g. isoflurane) is known to affect neuronal activity, cerebral metabolic rate and capillary blood flow speed in a dose-dependent manner [75]. Whilst the physiological parameters of all the animals were carefully monitored throughout this study, the potential effects of isoflurane may still be a confounding factor. The above-mentioned limitations might slightly bias quantification of the absolute transit parameters but are considered insignificant with regards to the relative comparisons between rest and stimulation.

In conclusion, we have innovatively employed ED-based OCT velocimetry with high spatiotemporal resolution to investigate the characteristics of capillary hemodynamics with an

emphasis on temporal RBC fluctuations. A concurrent increase in mCTV and TFB has been observed during a series of electrical stimulations of the mouse somatosensory cortex. Additionally, the absolute values of mCTV and TFB were found in direct proportion with a scaling factor independent of stimulation state. Furthermore, we have observed that the changes in mCTV and TFB are both negatively correlated with resting state mCTV, with the latter too being negatively dependent on resting state TFB. Finally, we have introduced a spatiotemporal-coupled Monte Carlo model to differentiate the contributions of mCTV and TFB to the spatiotemporally-coupled hemodynamics, which provides a means to analytically investigate the biophysical implications of capillary hemodynamics, allowing for the modeling of spatiotemporal-coupled hemodynamics, and for an understanding of the metabolic benefits of functional hyperemia. The experiments and simulations demonstrated in this work are expected to provide a more thorough and quantitative representation of capillary transit characteristics, which can be potentially used to investigate the hemodynamic responses in cerebral pathological conditions such as stroke and Alzheimer's diseases.

Chapter 3. Mapping and quantitating penetrating vessels in cortical brain with eigen-decomposition of OCT signals and subsequent principal component analysis

In this chapter, the topic of interest has moved on to the penetrating vessels in the cerebral cortex. Here, I first introduce the limitations of current methods for penetrating vessel mapping, especially those affiliated with OCT techniques. Targeted at those problems, a quantitative penetrating vessel mapping method is proposed with eigen-decomposition of OCT signals and subsequent principal component analysis. This method is further integrated with other OCT techniques and applied to analyze the vascular adaptations in abnormal neurobiological states.

3.1 Introduction:

In the cerebral cortex, surface and subsurface vascular networks are bridged by penetrating vessels, consisting of penetrating arterioles (PA) that branch from pia arterioles and dive radially into the brain parenchyma, and ascending venules (AV) that drain blood from microcirculatory beds and return to the superficial cortex into the central sinus [76], [77]. In contrast to surface and subsurface vasculatures where substantial collateral circulations and interconnections exist, penetrating vessels appear to be largely void of anastomoses [17], [18], which makes them the anatomical bottleneck for blood supply to the deep capillary beds [19], [20]. Moreover, this highly characterized architecture of penetrating vessels, with their irreplaceable function, would suggest particular vulnerability during the development of neurodegenerative diseases that have vascular involvements [19], [20], [78]. Previous reports have demonstrated that a loss of flow to even a single PA can give rise to columnar microinfarction extending through the whole depth of the cortex [78]–[80]. Severe blood flow reduction and flow reversal are also observed in clotting AVs, highlighting a potential role for cortical venule occlusion in cognitive disorders [20]. Furthermore,

preclinical evidences show that, in hypertensive rodents, penetrating arterioles are induced to perform inward hypertrophic remodeling in response to the increased intrinsic myogenic tone [81]. For those with type 2 diabetes, penetrating vessels are observed to be highly tortuous with significant lumen dilation and branching [82]. In general, the degeneration and dysfunction of penetrating vessels appear to be directly correlated with manifold neurological diseases, such as Alzheimer's disease [83], [84], cerebral amyloid angiopathy [85], perceptual deficit [80], and stroke [86]. Additionally, the accurate identification of penetrating vessels now becomes an important prerequisite for surgical procedures. For instance, the integration of neuroprosthetic devices to treat neurological disorders or investigate brain function requires an accurate visualization and quantification of penetrating vessel structures [87].

For this and other reasons, multiple imaging techniques have been employed to characterize the cerebral penetrating vessels. The most successful approach to date is high-throughput optical histology [88]–[90], which requires considerable efforts for tissue preparation and post-mortem staining. To speed up this process, a technical variation termed micro-optical sectioning tomography (MOST) was introduced to delineate three-dimensional (3-D) microvasculature by simultaneously performing ultrathin sectioning and microscopic imaging [91], [92]. However, the labor-intensive image stitching and vascular reconstruction post-processing remain unavoidable [93], often taking days to complete a single 3-D reconstruction. Moreover, an obvious limitation with histology is that it cannot provide dynamic and longitudinal information about circulations within living tissue, and thus cannot provide information about how penetrating blood flow adapts to metabolic regulation [89]. In this regard, *in vivo* "histology" through the use of functional magnetic resonance imaging (fMRI) [94], [95] has been used to map the penetrating arterioles and venules [96], [97]. However, the lateral resolution of state-of-the-art fMRI is limited to 50 × 50

μm [96], which is beyond the mean size of penetrating vessels [13]. In addition, the limited image contrast precludes the accurate identification and quantitation of penetrating vessels and associated blood flow rates. Recently, two-photon laser scanning microscopy (TPLSM) has been applied to high resolution angiography. While it offers the opportunity to map penetrating vessels together with connected capillary networks in individual penetrating territories [13], [20], [78], [89], [98], [99], the restricted imaging depth (up to 300 μm) and field of view (up to 300 × 300 μm) of TPLSM often poses a challenge to provide statistically powered analyses of cerebral blood flow dynamics in the investigation of neuro-degenerative disorders. In addition, the use of exogenous dyes and the long acquisition time due to its depth scanning protocol has made its translation into the clinic exceedingly difficult.

OCT is currently emerging as a promising non-invasive and real-time imaging technique that can provide volumetric microstructural information with a cellular level resolution and with a wide field of view up to centimeter scale over a living subject. In imaging cortical penetrating vessels, the intrinsic OCT signal is primarily contributed by the axial blood flow that is perpendicular to the tissue surface. Therefore, combined with the Doppler principle, phase-resolved Doppler OCT (DOCT) [100] is developed to achieve flow measurement of penetrating vessels *in vivo* [54], [101]. However, DOCT usually possesses a sizeable noise background due to the heterogeneous optical properties of the interrogated tissue [102]. To counter this limitation, optical coherence tomography angiography (OCTA) has been developed [4]–[9] and integrated with DOCT [57], [58], [103]–[107] for volumetric imaging of the cerebral vasculature. Among them, Doppler optical microangiography (DOMAG) [104], [106] has recently proven its efficiency in the identification of penetrating arterioles and venules from a projection view through manual *en-face* slicing [108]. However, in practice, the projection-tail artifacts originating from surface pia vessels

[109] typically overshadow the penetrating vessels below, which poses a difficulty for DOMAG to identify the penetrating vessels with sufficient accuracy.

In this chapter, we demonstrate an efficient OCTA solution that can automatically map cerebral penetrating vessels, by taking the advantages of the eigen decompensation (ED) frequency analysis and principal component analysis (PCA) upon the 3D OCT datasets. Firstly, the repeated OCT A-lines are acquired from the cerebral cortices of mice *in vivo* according to the OCTA velocimetry protocol [10]. Then, the ensemble OCT A-line signals are recast into a feature space as spectral components of eigenvectors, where the components possess unique distributions for the signals that represent penetrating vessels, surface communicating vessels, vessel-free regions, and territories occupied by enriched capillaries. Subsequently, the PCA is applied to the ED spectral components to identify such specific eigen distributions. On this basis, the penetrating vessels can be distinguished from either the capillary bed or superficial vasculature network, immune to projection-tail artifacts due to the overlaying functional vessels. This feature permits automatic identification of penetrating vessels from large volume OCT datasets. We integrate this method into a unique OCT imaging platform that can provide a comprehensive picture of cerebral blood circulation, including the topology of the microvascular networks, the morphology of penetrating vessels, and the hemodynamics of capillary vessels. To demonstrate its utility, the imaging platform is used to show the functional behavior of penetrating blood flows before and after an ischemic insult in a middle cerebral artery occlusion model of rodent.

3.2 Materials and Methods

3.2.1 System setup and imaging protocol

The OCT system used in this study is a spectral domain system configuration (Figure 1), similar to that reported in [11]. In brief, the system employed a super luminescent diode (LS2000C SLD, Thorlab Inc. NJ, USA) that operated at a central wavelength of 1340 nm and a spectral bandwidth of 110 nm, producing an axial resolution of ~7 μm. In the sample arm, a 10X objective lens (LSM02, Thorlab Inc., NJ, USA) was used to deliver the light into sample, offering a lateral resolution of 7 μm. For detecting the interference signal, a home-made spectrometer that is equipped with a fast line scan camera (SU1024-LDH2, Goodrich Inc., NJ, USA) was used, capable of an A-line rate of up to 92 kHz. The incident power on the sample was 3.5 mW and the system sensitivity was measured to be 105 dB. In consideration of the balance between temporal resolution and temporal sensitivity [6] to detect both fast and slow flow, the A-line speed was adjusted to 20 kHz and kept constant throughout the experiments.

The scanning protocol is shown in Figure 2A, which applies to all the experiments throughout. Specifically, there are 400 × 400 spatial positions designated at the sample surface, covering a region of 2.8 × 2.8 mm, which was achieved by raster scanning the probe beam using a galvo-scanner (6210H, Cambridge technology, MA, USA). At each spatial location, 50 A-lines were repeatedly acquired, i.e. M-mode scan. Thus, a 3D volume consists of 400 × 50 × 400 A-lines.

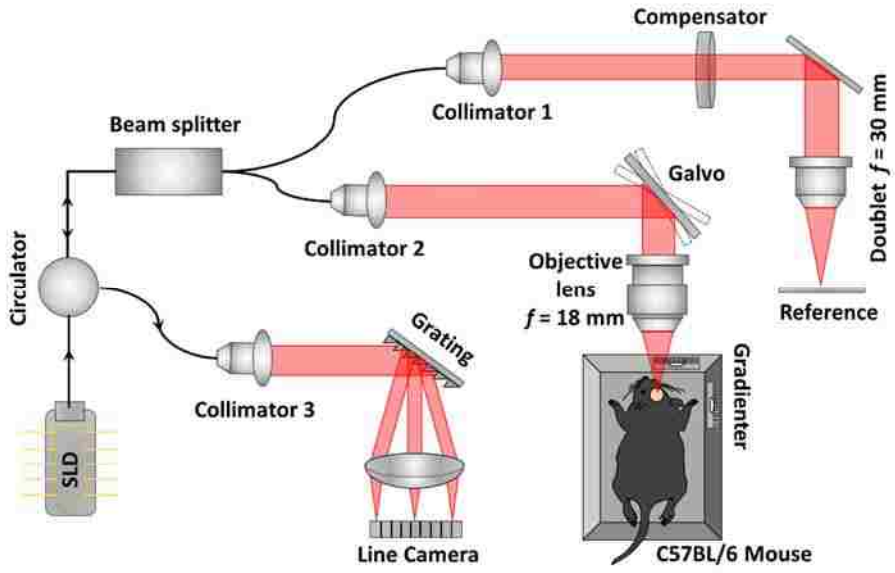

Figure 3.1. Schematic setup of OCT system for penetrating vessel mapping

3.2.2 Animal preparation

Mice (strain: C57BL/6, age: 2 months, weight: 24.4 ± 2.5 g, n = 5) were used in this study to demonstrate the utility of the proposed method. During procedure, the animal was anesthetized through isoflurane inhalation (0.2 L/min oxygen mixed with 0.8 L/min air), and surgically prepared by opening a cranial window above the right sematosensory cortex. The animal was then placed in a stereotaxic frame under the OCT probe. After baseline OCT imaging at resting state, middle cerebral artery occlusion (MCAO) was surgically given to induce permanent regional hypoperfusion state of ischemic stroke [110]. The animal then received second OCT imaging. Throughout imaging, body temperature was maintained at 36.8 ± 0.2 °C via a feedback homeothermic blanket system (50-7220F, Harvard Apparatus). The animal procedures described in this study were reviewed and approved by the Institutional Animal Care and Use Committee (IACUC) of University of Washington.

3.2.3 Penetrating vessel mapping and statistical explanation

The proposed method to map the penetrating vessels within cortical tissue is a continuation of OCTA velocimetry, as detailed in chapter 1 (equation (1.4) are rephrased here for the consistency of this chapter), where the OCT signals were decomposed into eigenvalues and eigenvectors through the ED processing. Following this work, assuming eigenvectors are derived from the ensemble A-lines captured at the same spatial location (Figure 2A), the spectral component of each eigenvector can be obtained by taking its first lag-one autocorrelation, as expressed in equation (3.1)

$$\omega_k = \frac{FPS/2}{2\pi} \arg\left\{\frac{1}{N_D-1}\sum_{m=0}^{N_D-2} e_k^*(m)e_k(m+1)\right\}, \tag{3.1}$$

where *FPS* denotes the sampling frequency (20 kHz in this study), $\arg\{.\}$ is the phase angle, N_D is the number of repeated A-lines (50 in this case), e_k (m+1) and e_k^*(m) are the k^{th} eigenvector from the (m+1)$^{\text{th}}$ A-line and the complex conjugate of the k^{th} eigenvector from the m^{th} A-line. In the following context, the mapping of the spectral components of eigenvectors is referred to as eigen components (EC). Note that in Figure 2B, each EC along *z'*-direction refers to the k^{th} spectral component (ω_k), with a value in the range of [0, 20,000], rather than in the depth scan of spatial domain (*z*-direction in Figure 2A).

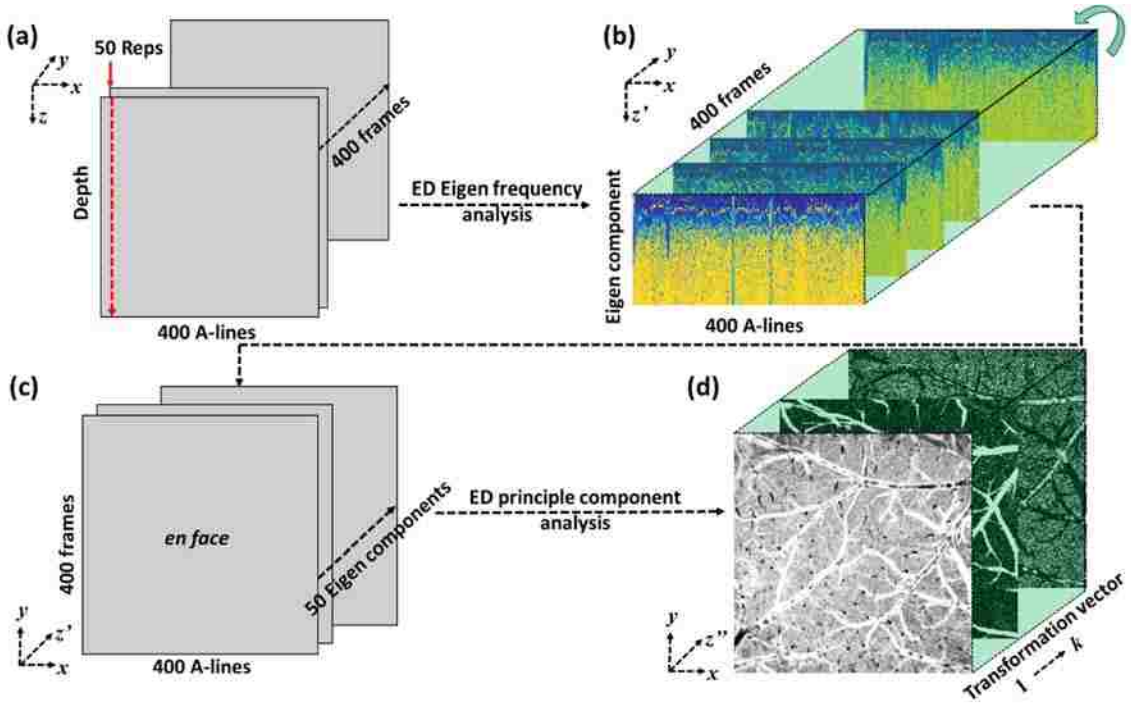

Figure 3.2. Data processing flow chart for mapping penetrating vessels. (A) Data acquisition protocol, where there are 400 × 400 spatial positions, covering a region of 2.8 × 2.8 mm. At each spatial location, 50 A-lines were repeatedly acquired. (B) Eigen component (EC) of the ensemble OCT signals for the dataset shown in (A). (C) Schematic of EC re-arranged from an *en-face* (*x* - *y*) view. (D) Principal component analysis (PCA) transformation vectors of (C), in which the first group reveals the distribution of penetrating vessels. Coordinates *x*: fast scan axis, *y*: slow scan axis, *z*: depth scan axis, *z'*: eigen component axis, *z''*: principle component axis

The derived dataset (Figure 2B) was then rearranged from the perspective of an *en-face* (*x* - *y*) view (Figure 2C). PCA was then applied by taking each eigen component (the same order of ω_k) as the observation and 2-D distribution of the eigen components as the features (i.e. each x-y slice), resulting in:

$$\begin{bmatrix} \lambda^{(1),[1]} & \lambda^{(2),[1]} & \cdots & \lambda^{(k),[1]} \\ \lambda^{(1),[2]} & \lambda^{(2),[2]} & \cdots & \lambda^{(k),[2]} \\ \vdots & \ddots & \cdots & \vdots \\ \lambda^{(1),[k]} & \lambda^{(2),[k]} & \cdots & \lambda^{(k),[k]} \end{bmatrix} = \begin{bmatrix} U_1^{[1]} & U_2^{[1]} & \cdots & U_N^{[1]} \\ U_1^{[2]} & U_2^{[2]} & \cdots & U_N^{[2]} \\ \vdots & \ddots & \cdots & \vdots \\ U_1^{[k]} & U_2^{[k]} & \cdots & U_N^{[k]} \end{bmatrix} \times \begin{bmatrix} \omega_1^{(1)} & \omega_1^{(2)} & \cdots & \omega_1^{(k)} \\ \omega_2^{(1)} & \omega_2^{(2)} & \cdots & \omega_2^{(k)} \\ \vdots & \ddots & \cdots & \vdots \\ \omega_N^{(1)} & \omega_N^{(2)} & \cdots & \omega_N^{(k)} \end{bmatrix}, \quad (3.2)$$

where the subscripts 1, 2, …, *N* denote spatial position index ($N = 400 \times 400$) , superscripts (1), (2), …, (*k*) denote ranks of eigen components [(k) = 50], and superscripts [1], [2], …, [k] denote ranks of principle components after PCA [[k] = 50]. λ denotes the dimensionality reduced principle components of the EC, i.e. the second matrix in the right side of Eq. (2). Note that the dimension

shrinks from ($N\times k$) to ($k\times k$)). U denotes the PCA transformation coefficients, implying the contribution of each element in U to each element in λ. According to the definition of PCA, λ gives the first k dimensional approximations of the EC, with the first principle component $\left(\lambda^{(1),[1]}, \lambda^{(2),[1]}, \dots, \lambda^{(k),[1]}\right)$ containing most of the information. Correspondingly, the first group of the transformation vector $\left(U_1^{[1]}, U_2^{[1]}, \dots, U_N^{[1]}\right)$ indicates the best linear combination of the first principle component, which inversely correlates with the penetrating vessels, giving the information about the spatial morphology of penetrating vessels from the *en-face* (x-y) view. The transformation vectors grouped according to the principle components 1, 2, …, k are schematically shown in Figure 2D with dynamic range scaled into [0, 255]. Statistical analyses of why $\left(U_1^{[1]}, U_2^{[1]}, \dots, U_N^{[1]}\right)$ can be used for mapping penetrating vessels (PVM) are detailed in the next paragraph.

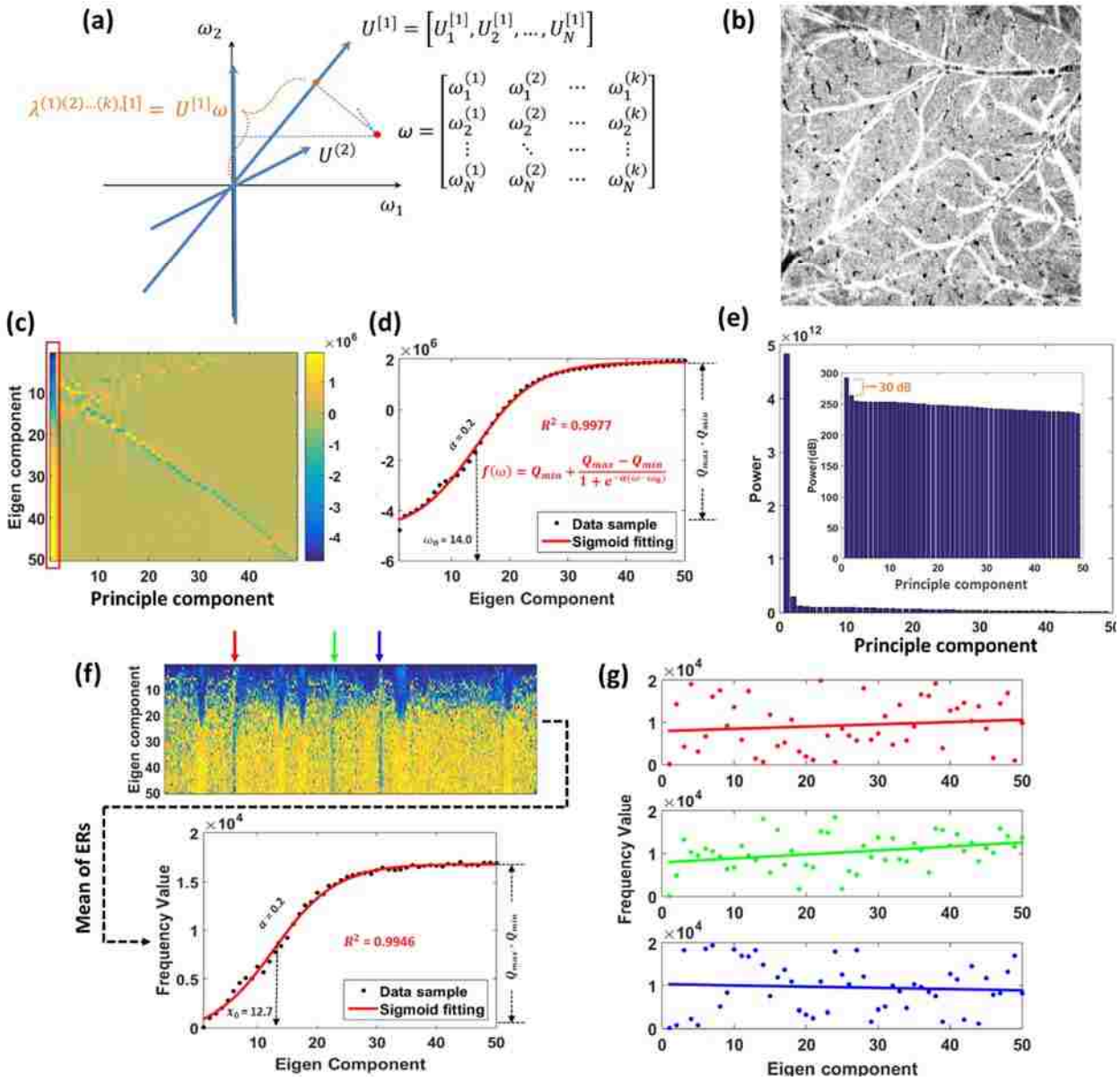

Figure 3.3. Statistical explanation of PCA transformation of EC of the captured OCT datasets for mapping the penetrating vessels. (A) Schematic diagram of EC data projection towards its most likely distributed direction along $U^{[1]}$. (B) 2-D mapping of the PCA transformation vector $U^{[1]}$, i.e. penetrating vessel map. (C) Dimension-reduced EC data expressed as principle components, in which the first component, marked by the red square, represents the dominant eigen distribution. (D) Sigmoid fitting of the first principle component reveals that the eigen distribution mainly follows a subtle logistic curve. (E) Power analysis of (C) indicating the dominance of logistic distribution in the EC of cerebral OCT data. (F) Representative B-frame used to additionally validate the logistic distribution (lower panel) by averaging ECs in one B-frame (upper panel). In the upper figure, the arrows indicate three regions with penetrating vessels resulting in uniform eigen distributions as in (G) top to bottom, respectively.

Here, PCA transformation is equivalent to projecting EC data in new directions based on their distribution probability, and sorting the new data components in descending order. The data projection towards the most likely distribution direction is schematically shown in Figure 3A with

the corresponding transformation vector re-mapped in Figure 3B, i.e. the penetrating vessel map. After this transformation, the first principle component (red square in Figure 3C) represents the most likely eigen distribution, which follows a logistic curve, as approximated through sigmoid fitting in Figure 3D. The fitting curve is also presented in Eq. (3) with center eigen component ω_0 = 14.0, slope α = 0.2, maximum Q_{max} = 1.9 × 10^6, and minimum Q_{min} = -4.2 × 10^6. In doing so, an excellent fitting coefficient of determination R^2 = 0.9977 is obtained.

$$f(\omega) = Q_{min} + \frac{Q_{max} - Q_{min}}{1 + e^{-\alpha(\omega - \omega_0)}}. \quad (3.3)$$

Moreover, the first principle component holds the highest quantity of frequency information, as characterized by the power analysis in Figure 3E and its subgraph (power in logarithmic scale). The first principle component has a power over 30 dB higher than the second one, highlighting the dominance of this well-defined logistic eigen distribution. This dominance is also supported by showing EC of one randomly selected B-frame and averaging over each line, which also yields a logistic distribution with a center ω_0 = 12.7, a slope α = 0.2 and a fitting R^2 = 0.9946, as shown in Figure 3F. Note here that it is not necessary for Q_{max} = 1.7 × 10^4 and Q_{min} = 0.1 × 10^4 to be close to those in Figure 3D, since the two expressions represent different amounts of power. However, as marked by the arrows in Figure 3F, since the penetrating flow has a similar speed along each A-line, the existence of penetrating vessels gives a uniform eigen distribution that locally breaks the sigmoid/logistic approximation, as shown in Figure 3G. By revisiting Eq. (2), we discovered that this local disruption of logistic distribution can be generalized as low values of certain elements in $\left(U_1^{[1]}, U_2^{[1]}, \dots, U_N^{[1]}\right)$, which provides a unique opportunity to map the penetrating vessels in the cortical tissue.

3.2.4 Quantification of penetrating vessel density

Mapped penetrating vessels above (i.e. Figure 3B) provides an opportunity to quantitate these vessels. Here, we propose a metric of penetrating vessel density (PVD) to indicate the number of active penetrating vessels within the scanned tissue volume. To provide PVD, two methods were employed in this study. The first was to use human-guided, semi-automatic vessel counting [111], which is however time consuming but can be regarded as an accurate quantification method. The second was an automatic approach which is more desirable for practical applications. Below are the steps to achieve automatic assessment of PVD: (1) smoothing the penetrating vessel map (e.g. Figure 3B) by a 2-D median filter with a kernel size of 3 × 3 pixels; (2) binarizing the result by assigning an empirical threshold of 100 in our study; (3) removing small regions with a size of 5 pixels or below from the map, based on the facts that the lateral spacing of 7 μm and the typical lumen diameter of penetrating arterioles of 18 μm [80]; (4) identifying pixel connectivity and counting centroids of the connected pixels; and finally (5) PVD was calculated by taking the ratio of the amount of the centroids to the scanned area.

3.3 Results:

3.3.1 Validation of the proposed penetrating vessel mapping PVM

Here, we compare the spatial locations of penetrating vessels identified by PVM with those identified by the OCT structures and OCTA angiograms (by OMAG algorithm) [10]. The representative B-frame EC and *en-face* view of penetrating vessel map are re-arranged and shown in Figure 4A and 4B, respectively. Figure 4A represents the B-frame EC located at the spatial location marked as the dashed line in Figure 4B. Slicing through the cross-sectional frames in the 3D OMAG angiograms and OCT structures, 5 consecutive frames located at the vicinity of Figure

4A were selected to show the 3D appearance of penetrating vessels, which are given in Figure 4C and 4D, respectively. Vessels that have well-defined penetration can be identified in Figure 4A, denoted by the interlinking arrows, and marked by the corresponding arrows in Figure 4B, and squares in Figs. 4C and 4D, respectively. Here, we can appreciate that the penetrating vessels are distinguished from surrounding pia vessels (representatively marked by "P") and capillary beds (marked by "C"), which would generally be difficult to differentiate in a single cross-sectional image, either structure or angiogram. For better visualization of the penetrating vessels, an x - z maximum intensity projection (MIP) of flow cross-sections from Figure 4C is provided in Figure 4E. A more elaborate analysis of Figure 4E indicates that the penetrating vessels are those directly connected with the surface vessels (i.e. trunks of the penetrating trees) with no involvement of slender branches. Such feature makes the quantification of PVD much easier from the PVM images.

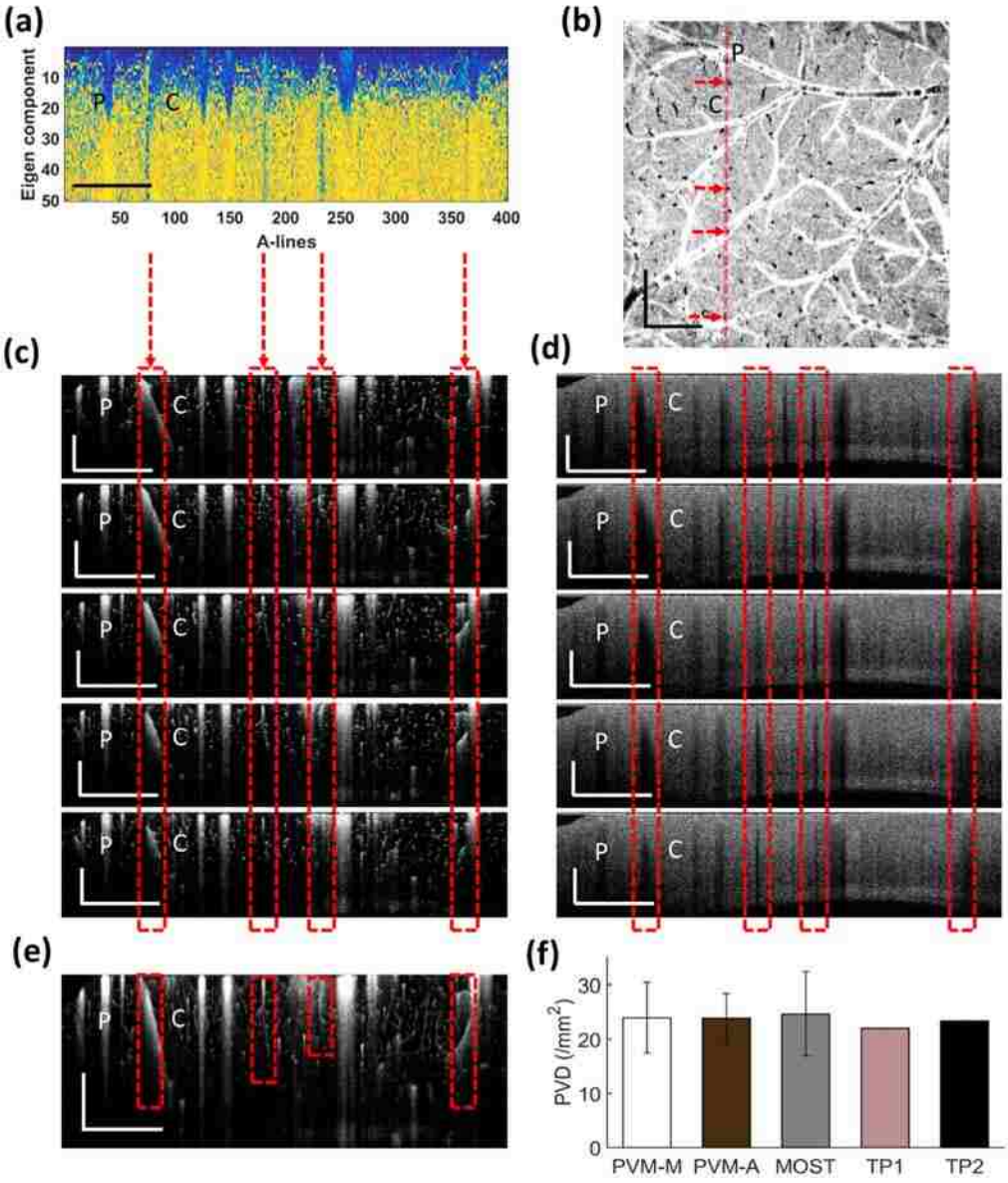

Figure 3.4. Validation of penetrating vessel mapping. (A) Representative B-frame eigen component. (B) The *en-face* view penetrating vessel map, where the dashed line indicates the position of (A). (C) 5-successive cross-sectional angiograms around the B-frame (A), which are taken from the 3D OMAG dataset. (D) The same location as in (C) but the structure OCT B-frames. (E) *x* - *z* MIP of 5 angiograms in (C). The four identifiable penetrating vessels in (A) are marked by squares in (C) – (E). The "P" in (A) – (E) denotes a typical surface pia vessel. The "C" denotes a typical capillary bed without involvement of big vessels. (F) Comparison of the PVD values among different imaging approaches where PVM-M, semiautomatic manual approach; PVM-A, automatic approach; MOST, micro-optical sectioning tomography; TP1 and TP2; two-photon laser scanning microscopy in two different studies. Scale bar = 500 μm.

We calculated the PVDs for volume scans obtained from all animals (n = 5) using both automatic and semi-automatic quantification methods, where the former gives mean PVD = 23.9 and standard deviation (STD) = 4.6, while the latter gives mean PVD = 23.9 and STD = 6.5.

Agreement between these values validates the automatic assessment. These values are also agreed well with those reported in prior literatures. For example, mean = 24.6 and STD = 7.7 (n = 5) were reported using MOST [20]. Using TPLSM, mean PVD = 22.0 in one study (n = 9, STD not available) [80] and 23.4 in another study (n = 6, STD not available) [20] were reported. For easier comparison, these results are also plotted in Figure 3.4F.

3.3.2 Comprehensive OCT cerebral analysis achieved by a single volumetric scan

In the analysis, the OCT derived results, including penetrating vessel maps, were first cropped to remove the regions near the cranial window edge to improve the fidelity of the measurement. One example of the cropped map of Figure 4B is shown in Figure 5A. Being the sources to transit blood vertically, penetrating vessels have intimate connection with the interwoven capillary networks, whose topology and hemodynamics are fundamental to the understanding of neurovascular coupling and the interpretation of brain functions [56], [89], [112]. In order to analyze the microvascular properties (i.e. capillary morphology, topology and blood flow dynamics) corresponding to the spatial locations of penetrating and pia vessels, we applied multiple OCTA algorithms to the same dataset. We used the prevailing OMAG algorithm [10], to achieve the structure (Figs. 5B) and vasculature images (Figure 5C), and the OCTA capillary velocimetry [10] to reveal the capillary flow speeds (Figure 5D). With these OCT derived cerebral vascular maps, it is relatively straightforward to provide more informative maps to illustrate the relationship between penetrating vessels and cerebral pia vessel networks. For example, the PVM map (Figure 5A) can be combined with OCTA map (Figure 5C) to form a single color-map as Figure 5E, where the penetrating vessels are coded in red color. As well, the combined image in Figure 5F represents the penetrating vessels of Figure 5A (red), the surface pia vessels of Figure

5B (green), and the normalized capillary flow velocity of Figure 5D (purple). These combined images represent an innovative way to study the neural degenerations [89]; for instance, Figure 5E would be useful to explore capillary density within certain columnar penetrating territory, or Figure 5F can be helpful in the investigation of the spatial dependence of capillary blood flow on the topology of penetrating and pia vessels.

In addition, DOMAG processing [106] of the same OCT dataset was also performed to provide an *en-face* view of bidirectional flow map (Figure 5G), where the green color indicates flow penetrating towards deep brain and the red indicates flow ascending to brain surface. To prevent the analysis of PVM from involving pia vessels, a classical method for DOMAG-based penetrating vessel identification was to use *x-y* slicing through the 3-D dataset (Figure 5H), and selecting the penetrating vessels at a given depth (e.g. ~50 μm from cortical surface (Figure 5I), where red represents penetrating flow and blue represents ascending flow). Although DOMAG provides an alternative way of mapping penetrating vessels, it has practical limitations: (1) the tailing artifacts originating from surface vessels may shadow the underneath penetrating flow; (2) the penetrating vessel identification tends to be subjective and sensitive to tissue surface topology; and (3) the slices at certain depths are also affected by secondary or lower rank penetrating branches that can give ambiguous measurable Doppler signals.

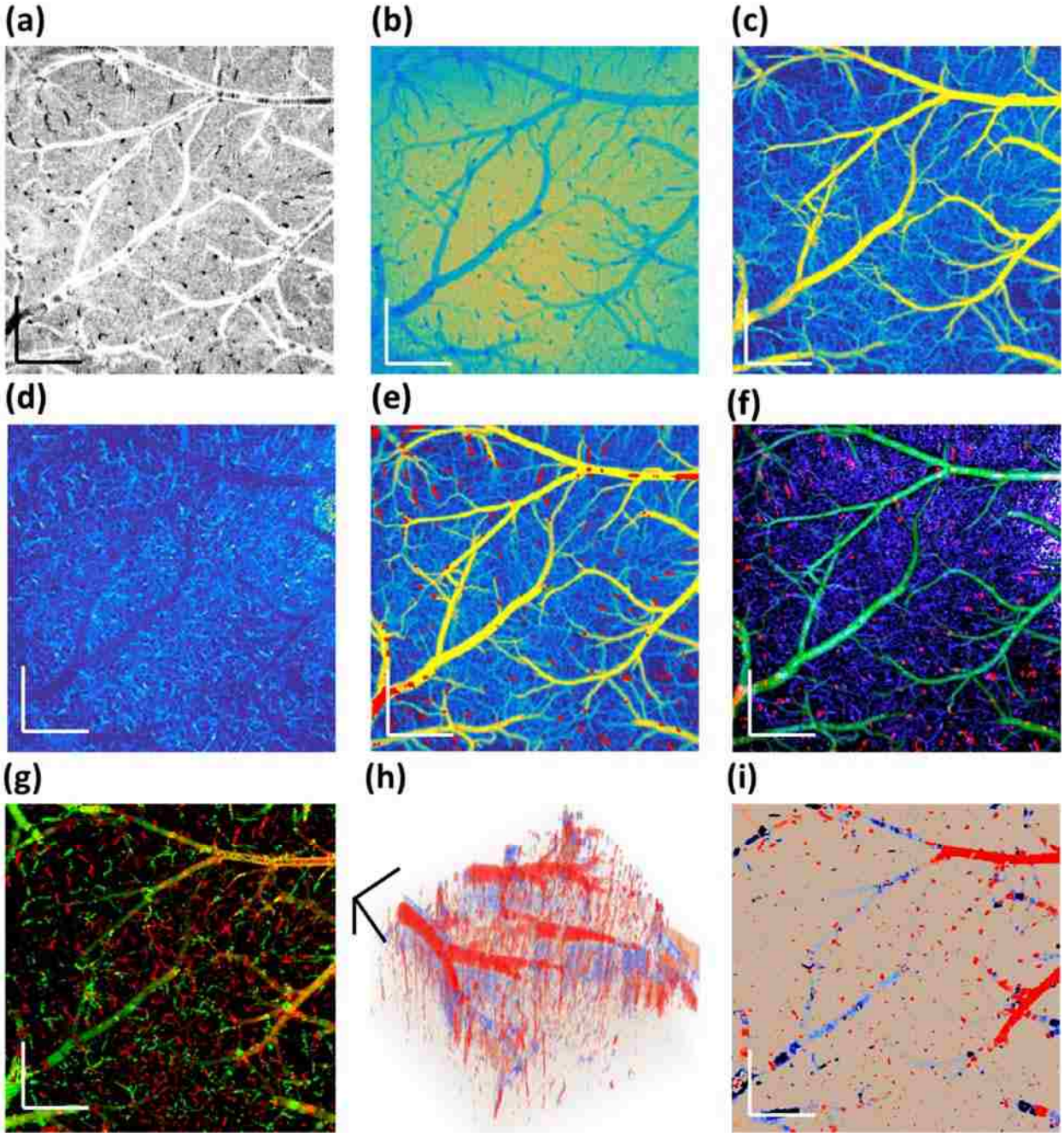

Figure 3.5. Comprehensive OCT cerebral analysis achieved by a single volumetric scan. (A) Penetrating vessel map, where black dots indicate the locations of penetrating vessels. (B) *En-face* view of tissue anatomy by mean intensity projection of 3D OCT structural signals. (C) *En-face* view of cerebral vasculature by mean intensity projection of 3D OMAG angiogram. (D) *En-face* view of capillary flow velocity normalized to [0, 1] obtained from OCTA velocimetry. (E) Composite image by overlying (A) on (C) to show the relationship of the penetrating vessels (red) with cerebral vascular networks. (F) Composite image by rendering penetrating vessels (in red), surface pia vessels (in green) and normalized capillary flow velocity (in purple) into one single color image. (G) Bidirectional DOMAG map with green representing the flow penetrating towards deep brain and red representing flow ascending to brain surface. (H) 3-D visualization of the DOMAG result. (I) An *x-y* slice from (H) at a depth of ~50 μm from cortical surface. In (H) and (I), the blue represents penetrating flow and red represents ascending flow. Scale bar = 500 μm.

3.3.3 The utility of cerebral PVM diagnosis in diseased status:

Penetrating vessels are reported to correlate with various neural degeneration disorders [83]–[86], among which acute ischemic stroke is of vital importance. In this study, a MCAO stroke model was carried out and the OCT-derived cerebral vasculature before and after MCAO were compared to investigate neurovascular adaption during stroke. Figure 6A and Figure 6B are *en-face* views of cerebral OCTA angiograms of the same region of mouse cerebral cortex before and after MCAO, respectively. In experiments, after the MCAO surgery, it became difficult to re-position the mouse exactly in the same way as baseline. However, it is required for the results to be co-registered between different time points. To meet this requirement, we applied an automatic affine registration [113] to co-register the results between Figure 6A and Figure 6B, resulting in a spatially-aligned image (Figure 6C) with regard to Figure 6A, where the un-aligned regions near the edge are zero-padded. The same was also applied to the PVM maps before and after MCAO (Figs. 6D – 6F). Scrutinizing through the co-registered images, both the perfused capillary beds (Figure 6C compared to Figure 6A) and the number of penetrating vessels (Figure 6F compared to Figure 6D) are observed to reduce dramatically due to the induced ischemic stroke. Moreover, the active arterio-arterial anastomosis (AAA) were evoked by ischemia in the infarct region (arrow heads in Figure 6C). To show the reduction of the numbers of penetrating vessels in cross sectional images, we selected representative EC maps at the same cortical location for comparison, which is shown in Figure 6G corresponding to the equivalent B-frames located at the dashed line in Figs. 6D and 6F. Each of the penetrating vessels identified by circles in Figs. 6D and 6F are marked by an arrow in Figure 6G. In this cross section, only two out of the six penetrating vessels are preserved after MCAO. A more comprehensive quantification is accomplished by calculating PVD across the maps of 6D and 6F, the results of which are plotted in the bar graph in Figure 6H. A

35% reduction in PVD was observed in this particular animal. Overall, an average of 41% reduction in PVD was observed for all 5 animals post-MCAO, as shown in Figure 6I.

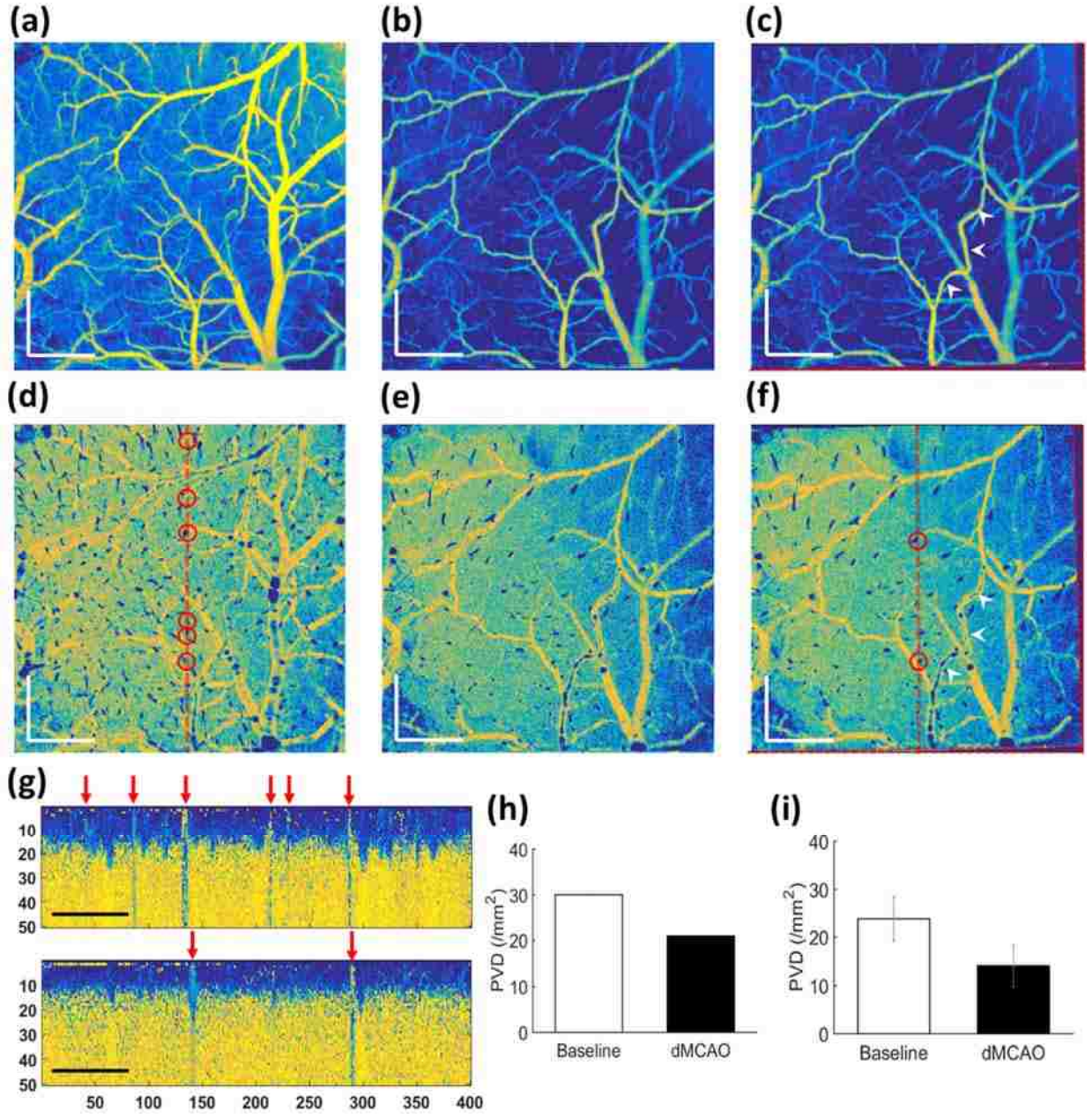

Figure 3.6. PVM-based cerebral vascular analyses of animals subject to MCAO. (A) *En-face* view of OCTA angiogram of a representative mouse cerebral cortex at baseline. (B) *En-face* view of OCTA angiogram of the same animal post-MCAO. (C) Affine registered OCTA (B) in reference to (A). (D) and (E) Penetrating vessel maps of the same region before and after MCAO, respectively. (F) Affine registered map of (E) with respect to (D). Adjusted edges after affine registration are marked by red dashed triangles in (C) and (F), respectively. (G) B-frame ECs corresponding to the dashed lines in (D) (upper) and (F) (lower). Each of the identified penetrating vessels is marked by a circle in (D) and (F) and an arrow in (G). (H) and (I) The bar graphs of automatically quantified PVD before and after MCAO, for this single animal and the statistics across 5 animals, respectively. Scale bar = 500 μm.

3.4 Discussion and conclusions

In this chapter, we have proposed and demonstrated a useful technique to map and quantitate the cortical penetrating vessels in animal models *in vivo*. Compared with conventional approaches relying on TPLSM, this OCTA-based PVM can identify individual penetrating vessels within a wider field of view, without any involvement of exogenous contrast agents. Moreover, compared to Doppler based OCTA approaches, like DOMAG, PVM takes the advantages of the unique statistical characteristics of cerebral vasculature, which is proven to be free from the tailing artifacts that are prevalent in almost any OCTA and DOCT variations. Furthermore, the eigen decompensation analysis and principal component analysis in the PVM are performed on an A-line basis. In other words, the vessel penetration information implied in the entire A-line is statistically projected onto the *en-face* (x-y) plane, independent from the depth selection that Doppler based approaches are usually subject to. In future, the detection of 3D vessel orientations [114] and the 3D vessel tracing can be adopted to extend current PVM to delineate the 3D architecture of penetrating vessels from volumetric OCT datasets.

To demonstrate the pre-clinical potential of PVM method, we conducted a controlled experiment utilizing a MCAO stroke model in mice. A significant decrease in PVD (41% overall, n = 5) has been observed after ischemic stroke through automatic quantification. Interestingly, local to the infarct region, more penetrating vessels are visualized around the AAA territory and its connected arterioles, as indicated by the white arrow heads in Figure 6F. Also, the survived penetrating vessels appear to have increased vessel lumen diameters (comparing Figure 6F with Figure 6D). This is probably due to a passive neurovascular response to the induced ischemic stroke, which minimizes flow resistance from an otherwise anatomical bottleneck - the penetrating vessels, providing augmented blood flow to the capillary beds. In addition, PVM is also useful in

revealing vessel damage information during stroke, as indicated by regions with intensities lower than their co-registered baseline counterparts but higher than those of penetrating vessels. A reasonable interpretation may be that the stroke-induced ischemia alters the statistical properties of the local microcirculatory tissue beds, which also undermines the dominant logistic eigen distribution to some extent in the ED and PCA analysis of the OCT signals. The delineation of vessel damages may need further optimization, which is beyond the scope of the current topic.

Although the PVM is technically promising, several limitations should be addressed in future development. As described by Kozai and colleagues, large penetrating vessels do not penetrate into the cortex exactly perpendicular from the surface, but deviate slightly from the normal axis in a statistically predictable manner [115], which seemingly makes our A-line-based identification difficult. However, we observed in our study that most of the regions occupied by penetrating vessels have the appearance of "commas" shape instead of "round dots", suggesting the robustness and some degree of tolerance of the proposed statistical projection in dealing with the slanted appearance of large penetrating vessels. Another limitation of our method is the lack of directional information, i.e. incapable of distinguishing between penetrating arterioles and ascending venules. In order to overcome this shortcoming, one possible solution could be to utilize the phase information in the complex OCT signal to calculate the +/- signed lag-one autocorrelation of eigenvectors in the ED analysis. The study of the direction-resolved PVM is currently ongoing. Other concerns may exist with the MCAO model as it directly works on the upstream middle cerebral artery rather than the penetrating vessels. Without loss of generality, however, the occlusion of an upstream artery is equivalent to blocking groups of penetrating arterioles downstream, resulting in a comparable cerebral capillary ischemia through the vascular hierarchy.

Typically, the study of small vessel diseases is achieved by occluding individual penetrating vessels through photothrombosis [19], [80], [89], which has been listed in our future plans.

In conclusion, we have developed an OCT-based mapping of penetrating vessels to assess cortical vessels and their possible remodeling under ischemic stroke. Eigen decompensation frequency analysis was employed to recast the spatiotemporal OCT signals as eigen representations in a feature space domain. The principal component analysis-based feature dimension reduction was consequently adopted to statistically project the eigen representations onto an *en-face* x-y plane, upon which the penetrating vessels can be identified and mapped based on the fact that the penetrating vessels locally break the subtle eigen distributions defined by the lateral-flow-dominated cerebral tissue beds. The PVM allows for the rapid, automatic identification of penetrating vessels from large volume OCT datasets acquired from cortical tissue with a wide field of view, free from comet-tail artifacts. A reduction in PVD and the remodeling of penetrating vessel patterns after MCAO were observed and quantified, which may be useful in improving our understanding of vascular adaptations to meet the metabolic requirements of abnormal neurobiological states. This technique may additionally prove useful in providing clinical and pre-clinical guidance for rational design of intracerebral probes, neuroprosthetic devices, and surgical procedures to minimize localized cerebral bleeding.

4. Morphological investigation of cortical surface vessels with automatic vessel diameter quantification and vessel tracing in OCT angiography

In this chapter, the topic of interest has been shifted to the cortical surface vessels mainly consisted of large communicating arteries and veins, whose functions are highly related to their morphological properties. To systematically analyze the vasculature, I built a comprehensive vasculature analysis framework including an innovative way of vessel diameter quantification and a novel approach for vessel tracing. The algorithms are first validated with well-characterized microfluidic flow phantoms, and then applied to cortical surface vessels *in vivo*. All the quantified results agree well with the microscopic findings in the literatures.

4.1 Introduction

The vasculature plays an important role in tissue development and remodeling under both normal and pathological conditions. For instance, in neurology, dysregulated angiogenesis is implicated in stroke, Alzheimer's disease and motor neuron disease [116]; in ophthalmology, evidence of vascular remodeling provides a critical indication of disease progression [117]; in oncology, the study of irregular tumor vessels can inform drug delivery approaches [118]; and during wound healing, specific vessel parameters have been shown to correlate with wound recovery time [111]. Rigorous investigation into the properties of specific vascular beds, therefore, has the potential to further understanding of disease pathogenesis, and lead to novel methods for the prevention and treatment of human disease.

OCT is a promising non-contact and high resolution 3-dimensional imaging technique that utilizes backscattering light to image tissue structures *in vivo* [119]. Its functional extension to OCT-based angiography (OCTA) has proven to have a high clinical significance, allowing

mapping of vascular networks directly from intrinsic OCT signals without requiring the use of exogenous dye [4], [6]. Since the initial applications of OCTA within the field of ophthalmology, numerous methods have been reported to measure the geometrical and morphological parameters of blood vessels from the acquired angiograms [61], [120]. Similar techniques have also been applied to small animal studies that demonstrate good correlations between vessel morphology and blood flow dynamics [11], [121]. To systematically quantify the vasculature, a common approach is to extract the key vascularity matrices, including vessel area density [55], [61], [121], vessel diameter [61], [122]–[124], vessel tortuosity [125]–[127], and vessel branching angle [124], [128]. Vessel diameter, in particular, allows the morphologic assessment of blood transport dynamics, by characterizing changes within the vascular bed (i.e. dilation or contraction) that directly relate to differences in blood flow. As a pilot clinical study, Goldenberg et al. reported a method for the manual measurement of retinal vessel diameter from cross-sectional OCT structural images [123]. Based on the results from manual segmentation, Pilch et al. further developed a statistical shape model that utilized supervised learning for automatic vessel segmentation and diameter quantification [129]. However, only big arterioles or venules were measured from the raster-scanned cross-sectional images. In an alternate approach, diameter distributions of *en face* choroidal vessels were quantified through a multi-scale morphological analysis with adaptive segmentation windows [130]. This method of quantification relies on assigned window sizes, however, requiring further optimization steps to improve its accuracy. In 2015, Yousefi et al. proposed a hybrid segmentation technique by combining Hessian filtering and OCTA intensity signals through a weighted average scheme, and accordingly quantified the vessel radius through distance transformation [122]. While promising, distance transformation, by simply estimating the distance to the nearest unidirectional boundary, does not accurately predict vessel radius (in most

cases, it will underestimate the radius especially for small vessels), and therefore the quantified values will likely be inconsistent even within the same vessel branch. This method of quantification is therefore limited in its application to clinical settings. Recently, the same group reported a clinically acceptable approach achieved by a series of vessel binarization, skeletonization, block-wise box counting (BWBC) and Gaussian filtering [61]. Using this method, significant difference in vessel diameter were reported when comparing control subjects with those suffering from macular telangiectasia type 2. Without consideration of vessel morphology, however, this method cannot provide consistent and robust measurement down to individual vessel branches. It is necessary to map the diameter of each specific vessel rather than the average diameter of an arbitrary block.

In this chapter we present an automated framework for the quantitative characterization of blood vessel diameter, down to the level of individual capillaries, using a gradient-guided mimimum radial distance (MRD) measurement. We validated this method by imaging and quantifying channel parameters within well-characterized microfluidic flow phantoms. Compared to the clinically well-accepted method in [61], our approach demonstrated superior consistency and accuracy, as well as a high tolerance to rotation of the vasculature patterns. We next developed a modified A* algorithm to trace vessel branches and calculate the diameter of each branch. Our rationale for using A* tracing was based on the key observation that blood cells always flow through the shortest vascular path between bifurcations. Following initial validation in flow phantoms, we applied our proposed algorithms to the analysis of mouse cortical vasculature *in vivo*. The values obtained appear to obey Murray's law [131] until reaching the capillary level, correlating well with previously published data [132], [133]. After tracing, vessel tortuosity and

vessel branching angle were automatically measured, establishing our approach as a comprehensive vasculature evaluation framework.

4.2 Material Preparation and Imaging

4.2.1 System setup

A spectral domain OCT system was developed and utilized for imaging. The schematic setup is presented in Figure 1. The system contained a broadband super luminescent diode (LS2000C SLD, Thorlab Inc.) with a central wavelength of 1310 nm and a spectral bandwidth of 110 nm, which provided an axial resolution of ~ 7 μm in the air. In the sample arm, a 10X objective lens was used to focus light onto the sample, corresponding to a lateral resolution of ~7 μm at full wide of half maximum. The interference signals were detected by a spectrometer that adopted a high-speed line scan camera (SU1024-LDH2, Goodrich Inc.) working at 92 kHz. With an incident light power of 3.5 mW, the system sensitivity was measured to be ~105 dB.

4.2.2 Microfluidic fabrication and animal preparation

For validation of our algorithms, image acquisition was carried out both *in vitro* within flow phantoms, and *in vivo* within a murine model, as shown in Figure 1. We devised 3 microfluidic patterns to mimic the real cerebral vasculature: a healthy vasculature, an ischemic vasculature with thoroughfare channels, and an ischemic vasculature with vessel dilation. Microfluidic patterns were designed using LayoutEditor software (© Juspertor, 2018) and transferred to silicon wafers via photolithographic patterning of positive photoresist followed by deep reactive-ion etching of exposed silicon. Patterns were then transferred to Polydimethylsiloxane (PDMS) using soft lithographic techniques, as previously described [134], [135]. PDMS was mixed with 0.18% TiO_2

particles prior to fabrication, in order to better mimic the optical properties of human tissue, and all PDMS devices were created with a final height of 1 mm. The microchannels within the flow phantoms were perfused with 1% intralipid solution at 1 mL/hr to mimic moving red blood cells. The intralipid solution was injected from the inlet, flowed through hierarchical vessel trees (with channels representing arterioles, capillaries, and venules), and finally emptied into the outlet reservoir. At each bifurcation point, a higher-order channel split into two equal-width lower-order channels. All tube heights were kept at 40 μm for ease of fabrication and perfusion. For *in vivo* experiments, an anesthetized mouse (strain: C57BL/6, age: 2 months) was surgically prepared through open-skull cranial window technique and carefully positioned in a stereotactic frame under the scanning probe, as in [136]. The animal procedures were reviewed and approved by the Institutional Animal Care and Use Committee (IACUC) of University of Washington.

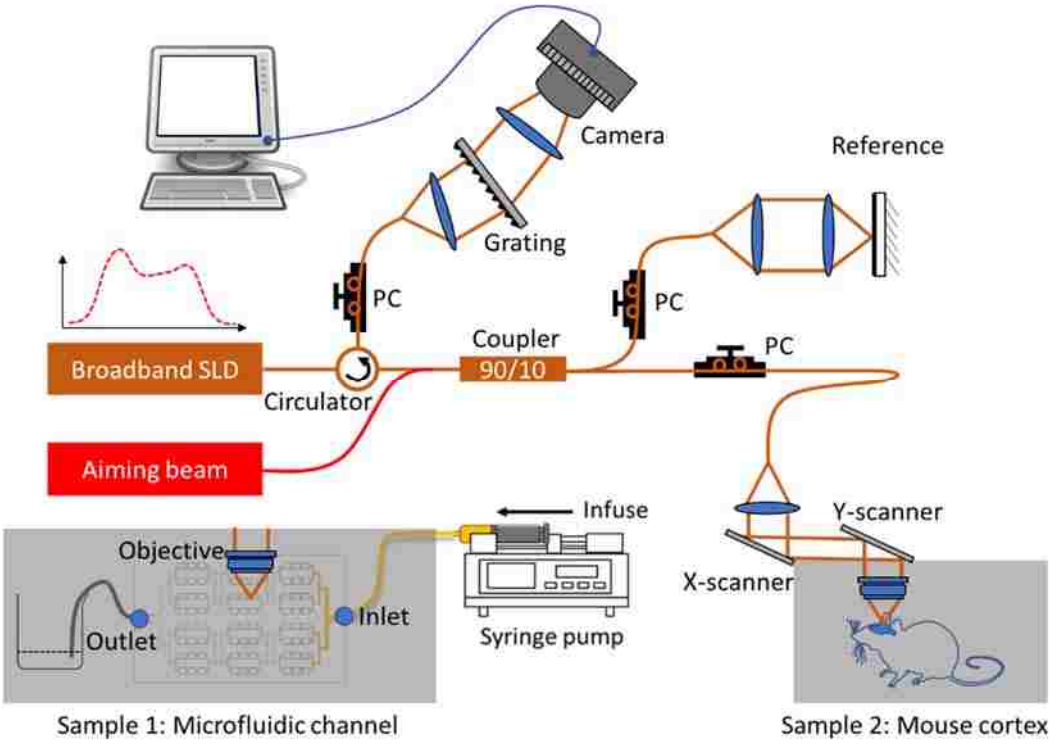

Figure 4.1. Schematic OCT system setup for the demonstration of automatic vessel diameter quantification and automatic vessel tracing

4.2.3 OCTA imaging protocols and data pre-processing

During OCTA data collection, we utilized repeated B-frame scanning protocols. Briefly, for the microfluidic channels, we acquired 738 A-lines along the fast scanning direction to pile into one B-frame, which covered a range of 4.8 mm. In the slow scanning direction, 800 B-frame positions were sampled with 8 repeated frames at each position, covering a range of 5.2 mm. The frame rate was controlled at 90 fps. For the *in vivo* cerebral imaging, a faster repetition rate of 180 fps was used to minimize artifacts from tissue motion. Here, we acquired 400 A-lines along the fast scanning direction, 3200 B-frames (400 B-positions × 8 frame repetitions) along the slow scanning direction, which covered a field of view of 3.5 × 3.5 mm.

After the data acquisition, complex-OCT-signal based OMAG [111] was employed to delineate the flow signal from the static tissue background. Then, the 3D angiography datasets were collapsed into 2D through layer-segmented maximum intensity projection (MIP) [113].

4.3 Vessel diameter quantification

Figure 2(a) shows the layout of the designed healthy vasculature: a highly symmetric pattern with five hierarchical channels (channel widths of 240 μm, 120 μm, 60 μm, 30 μm, and 15 μm) that cover a region of 3.94 × 4.93 mm. The corresponding *en-face* view OCTA vasculature is visualized in Figure 2(b), in which a red line indicates a typical cross-session of the capillary network as shown in the structure and flow images in Figure 2(c) and (d), respectively.

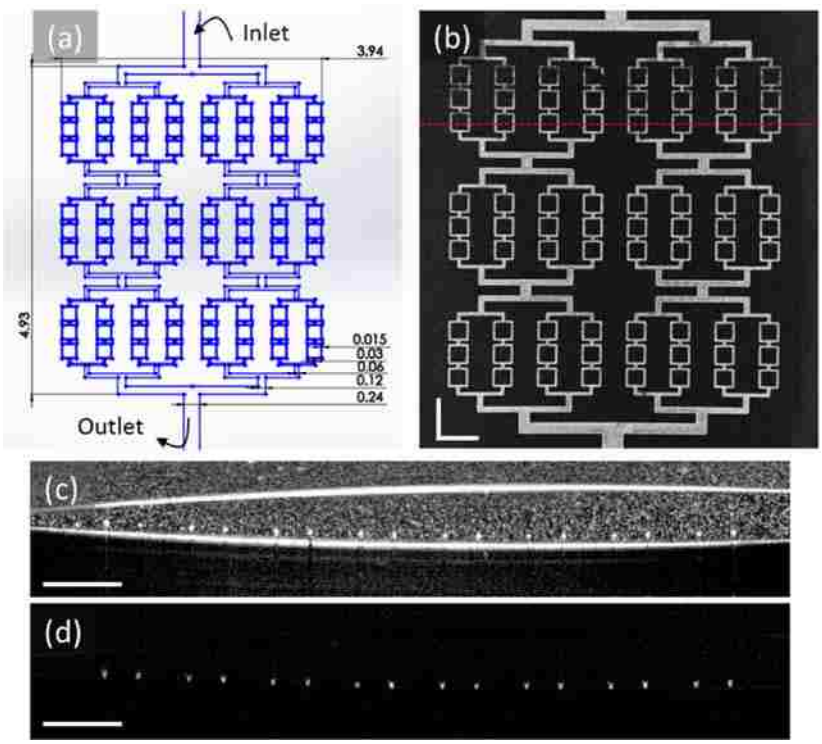

Figure 4.2. Microfluidic channel with healthy vasculature. (a) Layout of the channel pattern consisted of channels with widths of 240 µm, 120 µm, 60 µm, 30 µm, and 15 µm. All sizes in (a) are in millimeters. (b) OCTA *en-face* MIP image of the channel perfused with intralipid solution. (c) and (d) Cross-sectional structure image and flow image of the 15 µm capillary network at the location indicated by the red line in (b). Scale bars: 0.5 mm

The *en-face* vasculature was first binarized through a combination of global thresholding, hessian filtering and adaptive thresholding [122] into a binary vessel map (BVM), as shown in Figure 3(a). In the BVM, white pixels and black pixels represent the vascularized regions and avascular regions, respectively. Then, the BVM was further skeletonized by iteratively shrinking the outer boundary of the vascularized regions to a line with a single pixel width [122], as shown in the vessel skeleton map (VSM) of Figure 3(b). The contours of the channels could also be detected from the BVM through edge detection, as in the vessel perimeter map (VPM) in Figure 3(c). Once the vessel skeleton and vessel perimeter had been extracted, the vessel diameter could be calculated as the summation of radical distances between the skeleton line towards bilateral perimeter boundaries, as in the schematic shown as a subfigure of Figure 4.3(d). The searching direction is defined by the gradient analysis of the skeleton, as shown in the horrizontal and vertical

gradient maps in Figure 3(e) and (f), respectively. Each pixel in the skeleton will generate two reversed searching directions. The positive gradients (white) represent radical search towards the right in (e) and bottom in (f), and vice versa for the negative gradients (black). Following the searching directions, we calculated the minimum distances from the skeleton to its nearest perimeter boundary within the diagnoral searching quadrants (i.e. the 2 searching quadrants partitioned by grouping the horrizontal and vertical gradients) as denoted by the diagonal hatchings in the subfigure of (f), and sumed the two distances originating from the same skeleton pixel as one diameter value, as expressed by the following equation:

$$D = \min_{i \in VPM,Q}\left(\sqrt{(x_i - x)^2 + (y_i - y)^2}\right) + \min_{j \in VPM,\bar{Q}}\left(\sqrt{\left(x_j - x\right)^2 + (y_j - y)^2}\right) \quad (4.1)$$

where D represents the vessel diameter; (x, y) represents coordinate of a typical pixel in the vessel skeleton; (x_i, y_i) and (x_j, y_j) represent coordinates of pixels in the vessel perimater map (VPM) and belonging to the diagonal searching quadrants Q and $\overline{Q}$, respectively. Then, the calculated vessel diameters were applied to the skeletons as a color-coded VSM in Figure 3 (g). As displayed in Figure 3 (h), by projecting each vascularized region in the BVM towards its closest vessel skeleton, we can apply the color-coded diameter values to the entire vasculature pattern, as in Figure 3 (i). The calculated vessel diameters are displayed in parula colormaps and indicated in the colorbars in (g) and (i), respectively. Of note, here the diameter is directly measured from the vessel cross-section perpendicular to the instaneous perfusion flow, rather than the cross-section obtained from orthogonal OCT scanning, therefore providing more accurate quantifications of the physiological diameters, compared with previous approaches in [123], [129].

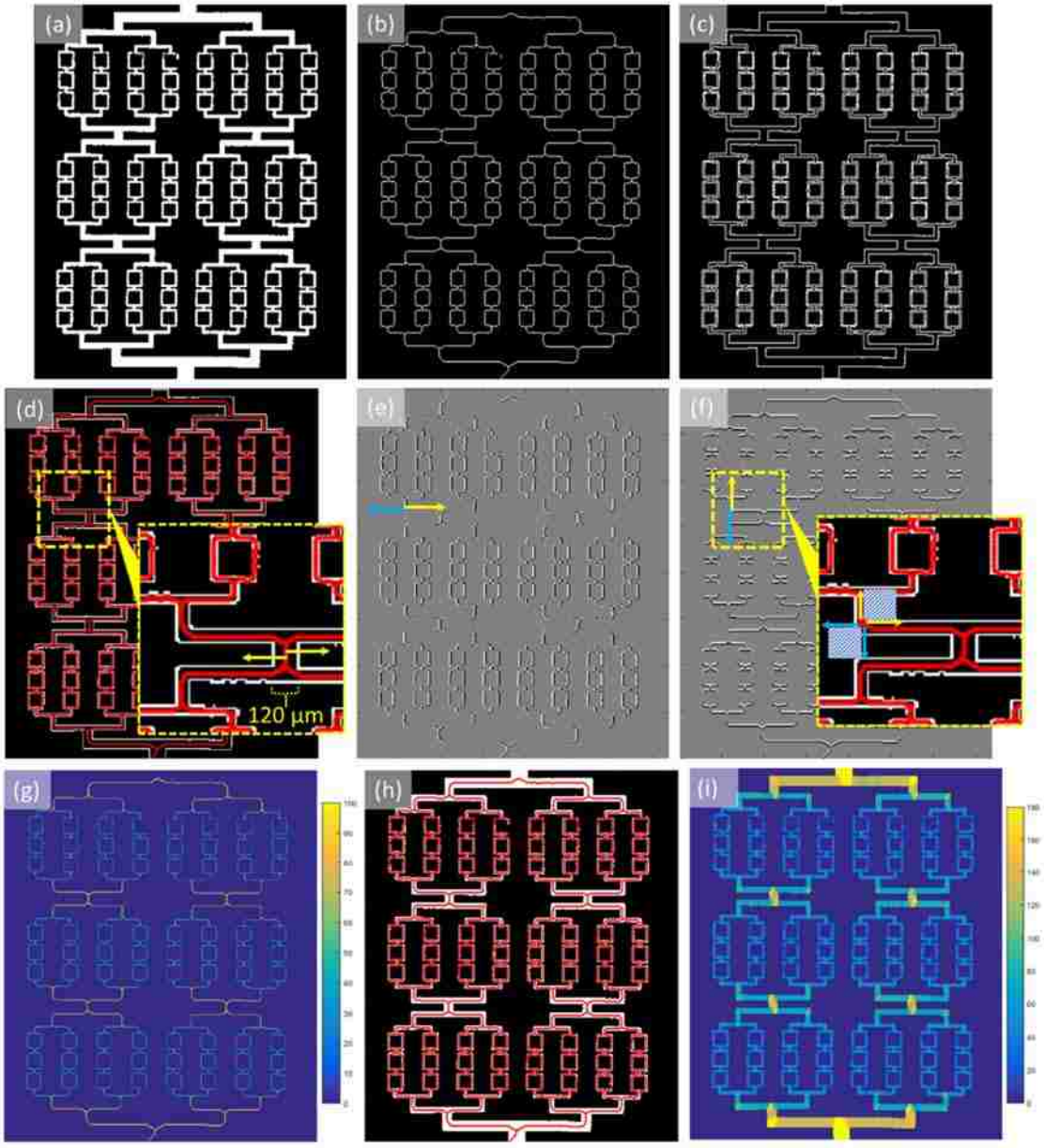

Figure 4.3. Demonstration of MRD automatic vessel diameter quantification of the healthy vasculature pattern. (a) Binary vessel map (BVM). (b) Vessel skeleton map (VSM). (c) Vessel perimeter map (VPM) (d) Overlay between the VPM (white) and the VSM (red). A local region is zoomed to demonstrate that vessel diameter is calculated as the summation of radical distances between the skeleton line towards bilateral perimeter boundaries. (e) Horizontal gradient of the VSM. (f) Vertical gradient of the VSM. The subfigure in (f) shows that practically the diameter is calculated as minimum radical distance within the diagnoral searching quadrants. The arrows in (d), (e) and (f) indicate the radial searching directions. (g) Color-coded vessel diameter parameters on the VSM. (h) Overlay between the BVM (white) and the VSM (red). (i) Color-coded vessel diameter parameters on the BVM.

The conventional way of estimating vessel diameter (i.e. BWBC method) is designed by arbitrarily selecting a block of $n \times n$ pixels, and calculating the averaged vessel caliber inside [61] as:

$$D_b = \frac{\sum_{x_b=1}^{n}\sum_{y_b=1}^{n} BVM(x_b,y_b)}{\sum_{x_b=1}^{n}\sum_{y_b=1}^{n} VSM(x_b,y_b)} \quad (4.2)$$

where D_b represents the block-wise vessel diameter, (x_b, y_b) represents the coordinate of each pixel inside the block, $\sum_{x_b=1}^{n}\sum_{y_b=1}^{n} BVM(x_b, y_b)$ represents the area of the vascularized regions (i.e. white pixels in (a)) within the block, and $\sum_{x_b=1}^{n}\sum_{y_b=1}^{n} VSM(x_b, y_b)$ represents the total lengths of the vessel segments within the block (i.e. white pixels in (b)), where the block size *n* is set as 20 pixels. By applying Eq.(1) to the entire vasculature pattern, a down-sampled block-wise diameter map was obtained, which was further interpolated to the original size of 800 × 738 pixels and Gaussian filtered with a 3 × 3 kernel to generate a quantitative evaluation map [61]. The locally averaged vessel diameters were visulized by integrating this map with binary masks either from BVM or VSM [61]. Indubitably, in the block-wise box counting method, the estimated vessel diameter is subject to the selected block size and the sample spacing, which requires further optimizations for various applications [121].

A series of comparisons between conventional BWBC and MRD were made based on the healthy vasculature pattern. Figure 4(a) and (c) show the quantified vessel diameters integrated with the VSM by using BWBC and MRD, respectively. To test the robustness of two methods, the same vasculature pattern was up-sampled two-fold, and the diameters were recalculated following BWBC and MRD algorithms, respectively, as shown in the right subfigures of (a) and (c). The arrows in (a) indicate that BWBC is subject to the sample spacing, as the block size and Gaussian filter in BWBC don't take vessel morphology into consideration. MRD still provided equivalent results after up-sampling, as indicated by the arrows in (c), with the regional diameter distributions visualized in the color-coded BVM as in Figure 4(b) and (d), respectively. The accuracy and consistency of MRD are superior to that of BWBC when quantifying single vessel branches, as

shown in the vessels with the same diameter of 120 μm indicated by the red dash boxes in (b) and (d).

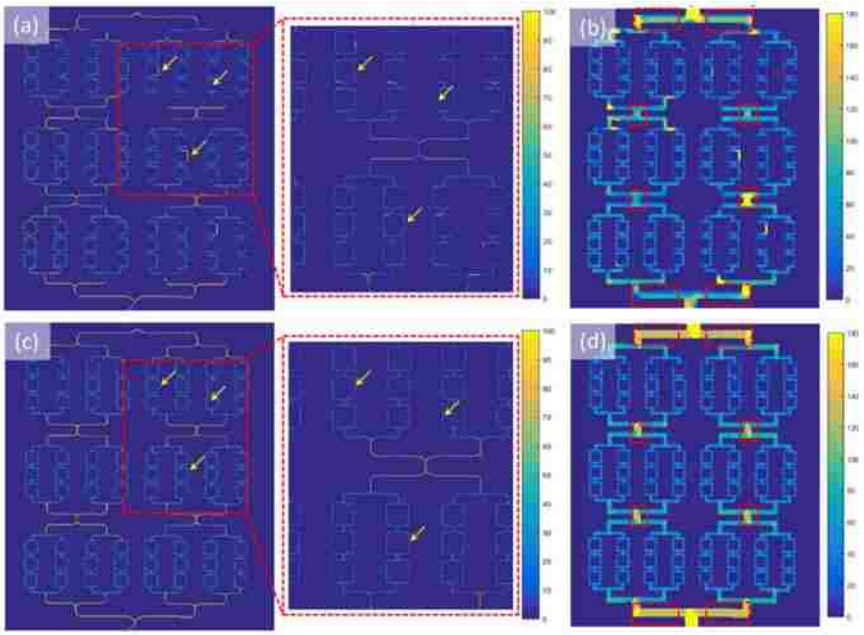

Figure 4.4. Comparison between block-wise box counting (BWBC) and calculation of minimum radical distance (MRD) based on the healthy vasculature pattern. (a) Vessel diameters integrated with VSM by BWBC. (b) Vessel diameters integrated with BVM by BWBC. (c) Vessel diameters integrated with VSM by MRD. (d) Vessel diameters integrated with BVM by MRD. In (a) and (c), the diameters of up-sampled (× 2) vasculature patterns are zoomed as shown in the right subfigures. The arrows indicate that BWBC is subject to the sample spacing, while MRD is still robust after up-sampling. In (b) and (d), the channels with the same diameter (120 μm) are marked by red boxes that reveal the superiority of MRD in quantification accuracy and consistency.

Additionally, we analyzed the vessel diameters of two patterns mimicking ischemic vasculature: both with ~ 1/6 loss of capillaries compared with the healthy vasculature, but one with thoroughfare channels (60 μm) and another one with vessel dilation (doubled vessel diameter at the central zone). For the first pattern, the layout of microfluidic design and corresponding OCTA MIP image are displayed in Figure 5 (a) and (b). The vessel diameter map integrated with VSM and that integrated with BVM by either using conventional BWBC or using MRD are shown in Figure 5 (c) and (d), and (e) and (f), respectively. Similarly, for the second pattern, the layout of the microfluidic design, the OCTA MIP image, the vessel diameter map integrated with VSM, and that integrated with BVM by either using BWBC or MRD are displayed in Figure 5 (g) - (l).

Visually, both BWBC and MRD detect the vessel diameter changes either in the thoroughfare channels or in the dilated capillaries. However, as indicated by the red dash boxes in (d) and (j), the distribution of quantified diameters appears to be shifted for the BWBC algorithm due to the rotation of the obtained OCTA vasculature patterns (~ 3°). In contrast, MRD exhibited high tolerance to pattern rotation, as indicated in (f) and (l).

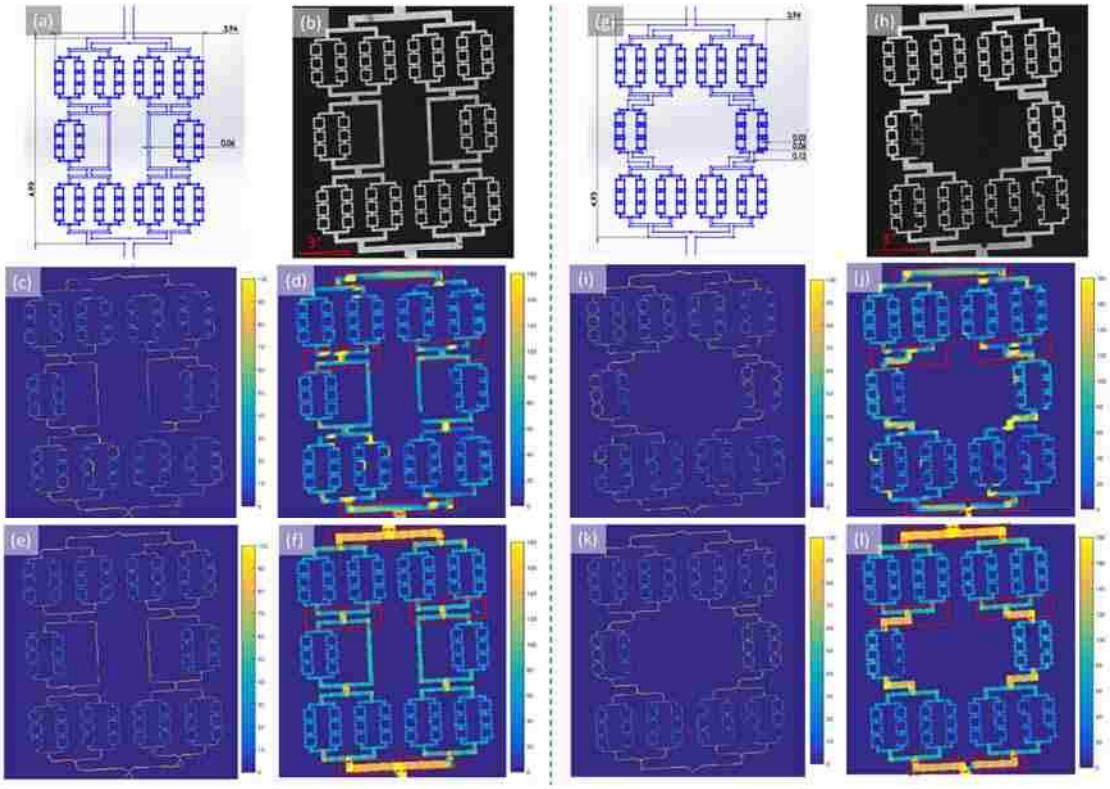

Figure 4.5. Comparison between block-wise box counting (BWBC) and calculation of minimum radical distance (MRD) based on two ischemic vasculature patterns. (a) Layout of the ischemic vasculature with thoroughfare channels. (b) OCTA *en-face* MIP image of the pattern in (a). (c) and (d) the diameter maps of vessels in (a) integrated with VSM and integrated with BVM, as calculated by BWBC. (e) and (f) the diameter maps of vessels in (a) integrated with VSM and integrated with BVM, as calculated by MRD. (g) Layout of the ischemic vasculature with vessel dilation. (h) OCTA *en-face* MIP image of the pattern in (g). (i) and (j) the diameter maps of vessels in (g) integrated with VSM and integrated with BVM, as calculated by BWBC. (k) and (l) the diameter maps of vessels in (g) integrated with VSM and integrated with BVM, as calculated by MRD. During OCT imaging, the vasculatures in (a) and (g) are rotated counter-clockwise by ~3°. All sizes in (a) and (g) are in millimeters. In (d) and (j), the red squares indicate regions that are affected by the rotation of vasculature patterns, while MRD proves high tolerance to the rotation as indicated in (f) and (l).

4.4. Automatic vessel tracing

To trace the vessel branches and accordingly calculate the mean diameter of each branch, we first automatically detected the bifurcations, as indicated by the green dots in Figure 4.6 (b), by applying the following searching equation to each skeleton pixel:

$$\left\{\sum_{i=-1}^{1}\sum_{j=-1}^{1} VSM(x+i, y+j) \geq 4\right\} \cap VSM(x, y)$$

where $VSM(x, y)$ represents a typical pixel of the vessel skeleton, and $VSM(x+i, y+j)$ represents its neighbor pixels. The criterion ≥ 4 is assigned according to an observation that the bifurcation point has more neighbors (≥ 3) compared with the midpiece (neighbor $= 2$) or the terminal (neighbor $= 1$), as representatively indicated by bifurcations a, b and c compared to midpieces d, e and f in (b). For this microfluidic pattern, some corners (e.g. g and h in (b)) were mistakenly detected as bifurcations due to slight skeletonization artifacts for 90 degree corners. Fortunately, those false positive bifurcations will only add vessel segments but not affect the tracing results. Since we extract all the bifurcations, we can automatically trace between any two of them for an overview of the entire vasculature. Practically, however, in clinical scenarios physicians may only care about a small number of branches along a single vessel tree. For this reason, a bifurcation and 3 of its connected branches (yellow dot: starting; red dots: ending) within the red dash box in (c) are selected for demonstration of the tracing process.

As blood flow always travels through the shortest (lowest-resistance) path between two bifurcations, vessel tracing was conducted using an A* path searching algorithm [137]. A* applies an informed searching on all accessible paths to find the one that incurs the smallest cost (least distance travelled in this study). Specifically, A* iteratively selects the path (pixels of the vessel skeleton) that minimizes

$$f(m) = g(m) + h(m) \tag{4.4}$$

where m is the latest selected pixel, $g(m)$ is the distance travelled from the starting, $h(m)$ is the heuristic that estimates the cost of the cheapest path from m to the ending. According to the design of the A* algorithm, the heuristic must never overestimate the actual distance to the ending. Here $h(m)$ was assigned as the straight-line distance (Euclidean distance) that satisfies this criterion. In $g(m)$, each step towards the edge-connected neighbors would be counted as 1, and that towards the diagonal-connected neighbors as $\sqrt{2}$. The searching process is visualized as movie frames in Figure 6(d): (1). initialization of the starting; (2)-(4). tracing towards three surrounding endings, respectively; (5). automatic re-initialization of a new starting at downstream.

By integrating the tracing with BWBC- and MRD-based vessel diameter maps in Figure 4(a) and (c), we calculated the mean diameters of ten vessel branches as marked in numbers in Figure 7(a) and listed in Figure 7(b). To analyze the quantification errors with respect to the true diameter values from the designed layout, we employ two evaluation parameters: the total error and the variance of error as defined by

$$Total\ error = \sum|D - D_t| \tag{4.5}$$

$$Var\ of\ error = \sum(|D - D_t| - \frac{1}{N}\sum|D - D_t|)^2 \tag{4.6}$$

where D represents the quantified diameter, D_t represents the true value, N represents number of the vessel branches (N = 10). The total error suggests that BWBC is more prone to errors (~ 3 times) compared with MRD. The variance of error reveals that the stability of the diameter quantification by BWBC is much worse than that of MRD.

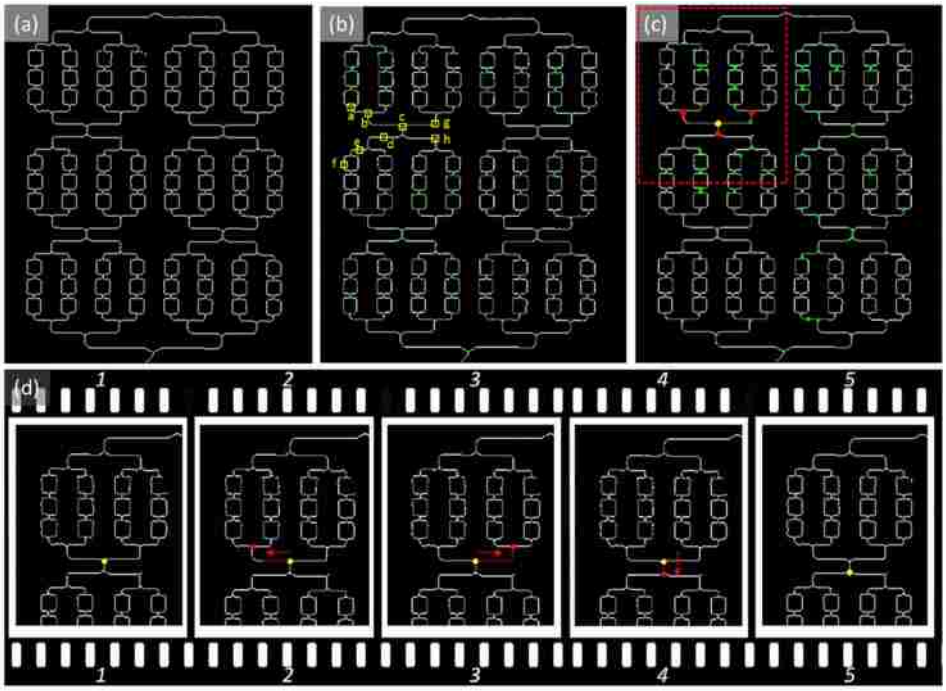

Figure 4.6. Demonstration of automatic vessel tracing based on the healthy vasculature pattern. (a) Vessel skeleton map same as Figure 3(b). (b) The detected bifurcations (green dots) overlaid on the vessel skeleton map. (c) Selection of starting (yellow dot) and ending (red dot) of each vessel branch. (d) Frames taken from an automatic tracing movie of the region marked by a red square in (c): (1). Initialization of the starting; (2)-(4). Tracing towards 3 endings, in which red arrows indicate the tracing direction; (5). One of the downstream ending is automatically re-initialized as the starting.

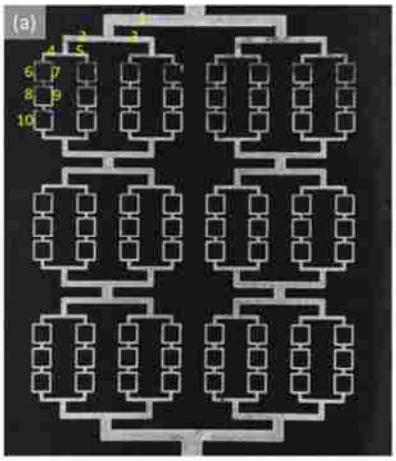

(b)

Vessel branch	True value (μm)	BWBC (μm)	MRD (μm)
1	120	147.2	124.9
2	60	111	66.9
3	60	41.6	59.2
4	30	50.8	39.4
5	30	50.3	34.4
6	15	25.6	21
7	15	32.2	22.5
8	15	39.9	24.2
9	15	22.7	18.8
10	15	15.5	22
Total Error	0	161.8	58.3
Var of Error	0	299.4	8.0

Figure 4.7. (a) OCTA MIP image of the healthy vasculature pattern same as Figure 2(b), in which numbers 1-10 indicate ten branches of a vessel tree. (b) The true vessel diameters of the ten branches, the calculated mean diameters by integrating automatic vessel tracing with BWBC, and the calculated mean diameters by integrating automatic vessel tracing with MRD. The quantification errors are analyzed as total errors and variances of error for BWBC and MRD, respectively.

4.5. Quantitative morphological evaluation of cerebral vasculature in vivo

The automatic vessel diameter quantification and automatic vessel tracing were integrated to evaluate vessel diameters in mouse cerebral cortex *in vivo*. Figure 8(a) shows the microscope image of the mouse cerebral cortex through a transparent cranial window. Correspondingly, we acquired the OCT dataset and extracted the OCTA angiogram (the top 5-μm/1-pixel from the tissue surface) as in Figure 8 (b), where the bifurcations in a superficial vein up to 7 generations are labelled in alphabetical order. First, the angiogram was binarized and skeletonized as Figure 8 (c). Thereafter, the bifurcations were automatically detected as green dots in Figure 8 (d). To ensure the robustness of vessel tracing within this *in vivo* dataset, vessel fragments with low connectivity were excluded from analysis from (c) to (d). In (d), the alphabetically labelled bifurcations are marked as starting (yellow dots), whose surrounding bifurcations are marked as ending (red dots) to trace along each vessel branch. Next, the vessel diameter information was integrated with VSM through BWBC as in Figure 8 (e), and through MRD as in Figure 8 (f). In BWBC, the block size n was reset as 10 pixels to match the lateral samping of 400×400 pixels.

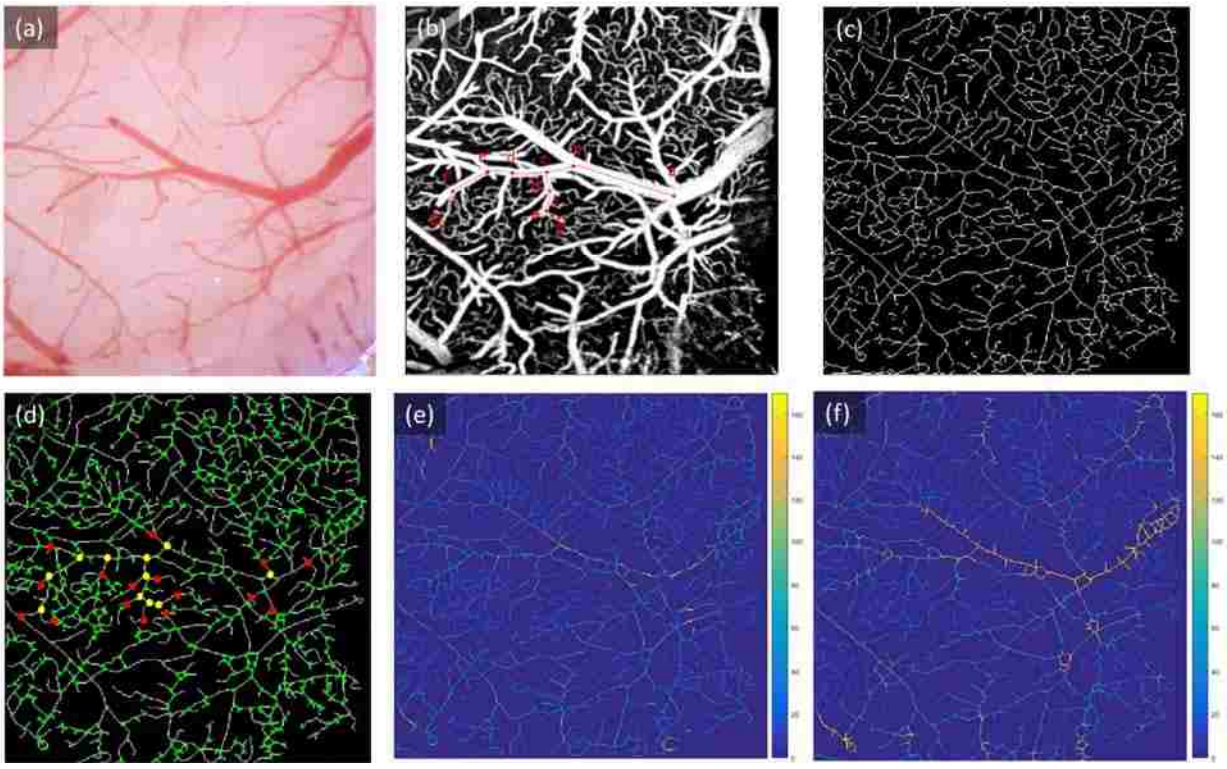

Figure 4.8. (a) The microscope image of mouse cerebral cortex through a cranial window. (b) OMAG *en-face* view image of the surface vasculature. The selected bifurcations up to 7 generations are labelled in alphabetical order, in which (d, e, f, g) and (d', e', f', g') correspond to bifurcations of two big branches on the same level. (c) Vessel skeleton map. (d) Bifurcations (green dots) are automatically detected from the skeleton, in which selected bifurcations in (b) are marked as yellow dots, and the surrounding red dot indicates the ending of each connected vessel branch. (e) Vessel diameters integrated with VSM by BWBC. (f) Vessel diameters integrated with VSM by MRD.

It is conceivable that analysis of vessel diameters at bifurcations is relevant to the understanding the partition of cerebral blood flow in flow-related pathological changes, such as cerebral venous thrombosis [138] and venous insufficiency [139]. The mean diameters of vessel branches that are automatically measured through MRD plus vessel tracing are listed on the OCTA angiogram in Figure 9(a). For comparison purpose, the same branches were also evaluated through BWBC plus vessel tracing, and manually measured by one skilled technician specializing in OCTA imaging (diameter values from these two methods are not listed). Additionally, we introduced two indexes to evaluate the relations in diameters between the parent and the child branches at each bifurcation. The first index is generalized as a cubic dependence as calculated by $\text{Cubic} = (\sum_{i=1}^{N} D_i^3)/D_0^3$

(where D_i represents the diameter of each child branch, and D_0 represents the diameter of the parent branch). According to Murray's law [140]–[142], this cubic dependence should be close to 1, such that the cost for blood transport and maintenance are minimized. The second index is described by the area ratio of vessel calibers (square dependence) as calculated by $\text{Square} = (\sum_{i=1}^{N} D_i^2)/D_0^2$. In our analyses, these two indexes are calculated for each vessel branch and for each measurement approach, as listed in Figure 9 (b) and (c), respectively. The mean cubic dependences obtained from manual measurement (0.978±0.033) and MRD (1.026±0.116) are close to the theoretical standard of 1 that following Murray's law. And, the mean square dependences obtained from manual measurement (1.245±0.056) and MRD (1.247±0.131) are within the range of 1.10 - 1.28 reported for cerebral vessels in the literature [128], [133], [142]. However, significant systematic errors exist in the results from BWBC (1.201±0.187 for cubic dependence and 1.401±0.157 for square dependence).

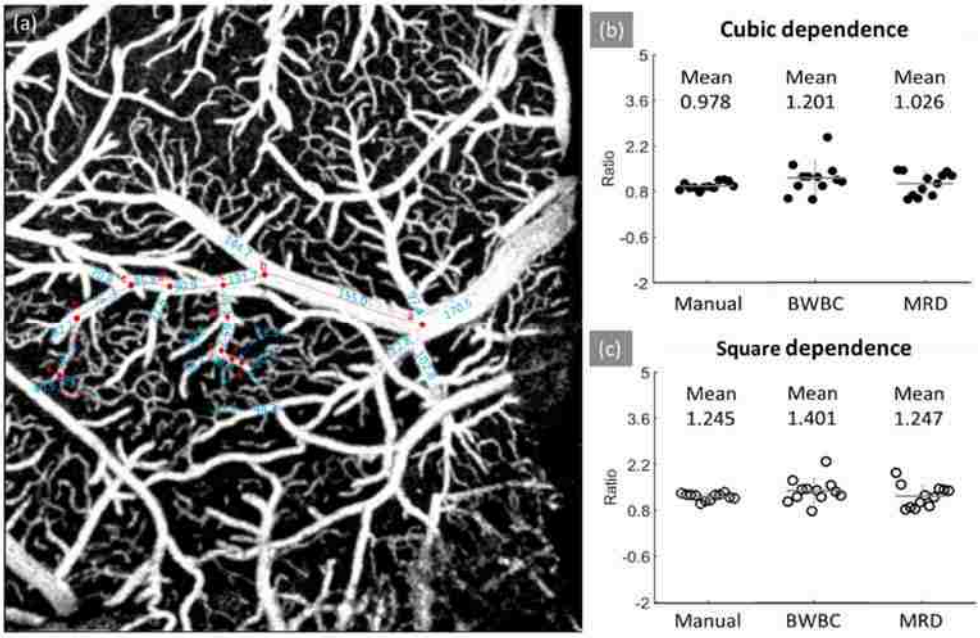

Figure 4.9. (a) OCTA angiogram with labeled mean vessel diameters (cyan) quantified through MRD plus vessel tracing. (b) Cubic dependences $(\sum_{i=1}^{n} D_n^3)\ /D_0^{-3}$ measured with manual measurement, BWBC, and MRD, respectively. (c) Square dependences $(\sum_{i=1}^{n} D_n^2)/D_0^{-2}$ measured with manual measurement, BWBC, and MRD, respectively. In (b) and (c), each dot represents an individual bifurcation, and the horizontal bar represents the mean with standard deviation.

To enable a thorough morphological evaluation of the cerebral vasculature, vessel tortuosity and vessel branching angle were automatically measured after vessel tracing. The length of the vessel branch was measured with each step towards the edge-connected neighbors as 1, and that towards the diagonal-connected neighbors as $\sqrt{2}$. The vessel tortuosity can then be calculated as the vessel length divided by the straight-line distance between two bifurcation points. The measured tortuosities of two arterio-arterial anastomosis vessels are 1.142 and 1.129, as in Figure 10(a) and (b) respectively, within the reasonable range in literature [125]. The vessel branching angle is obtained by selecting the first 10 pixels from each child branch, fitting them to linear approximations, and then calculated by:

$$angle = \text{atan}\left|\frac{k_1 - k_2}{1 - k_1 \times k_2}\right| \tag{4.7}$$

where atan represents the calculation of arc tangent angle, k_1 and k_1 represent the fitted slopes of the instantaneous flow directions for two child branches. As this slope-based calculation doesn't account for angle orientation, we additionally use the length of the selected vessel segments to differentiate between acute angle or obtuse angle:

$$angle = \begin{cases} \text{atan}\left|\frac{k_1 - k_2}{1 - k_1 \times k_2}\right| & if\ L_{01}^2 + L_{02}^2 > L_{12}^2 \\ 180^\circ - \text{atan}\left|\frac{k_1 - k_2}{1 - k_1 \times k_2}\right| & if\ L_{01}^2 + L_{02}^2 < L_{12}^2 \end{cases} \tag{4.8}$$

where L_{01} and L_{02} are the line distances of the 10th pixels in two branches from the starting; L_{12} is the straight-line distance between the two 10th pixels. The automatically measured branching angles are listed in Figure 10(c) - (f), with the data demonstrating that our algorithm performs well throughout a range of different angle orientations, including both acute and obtuse branching angles.

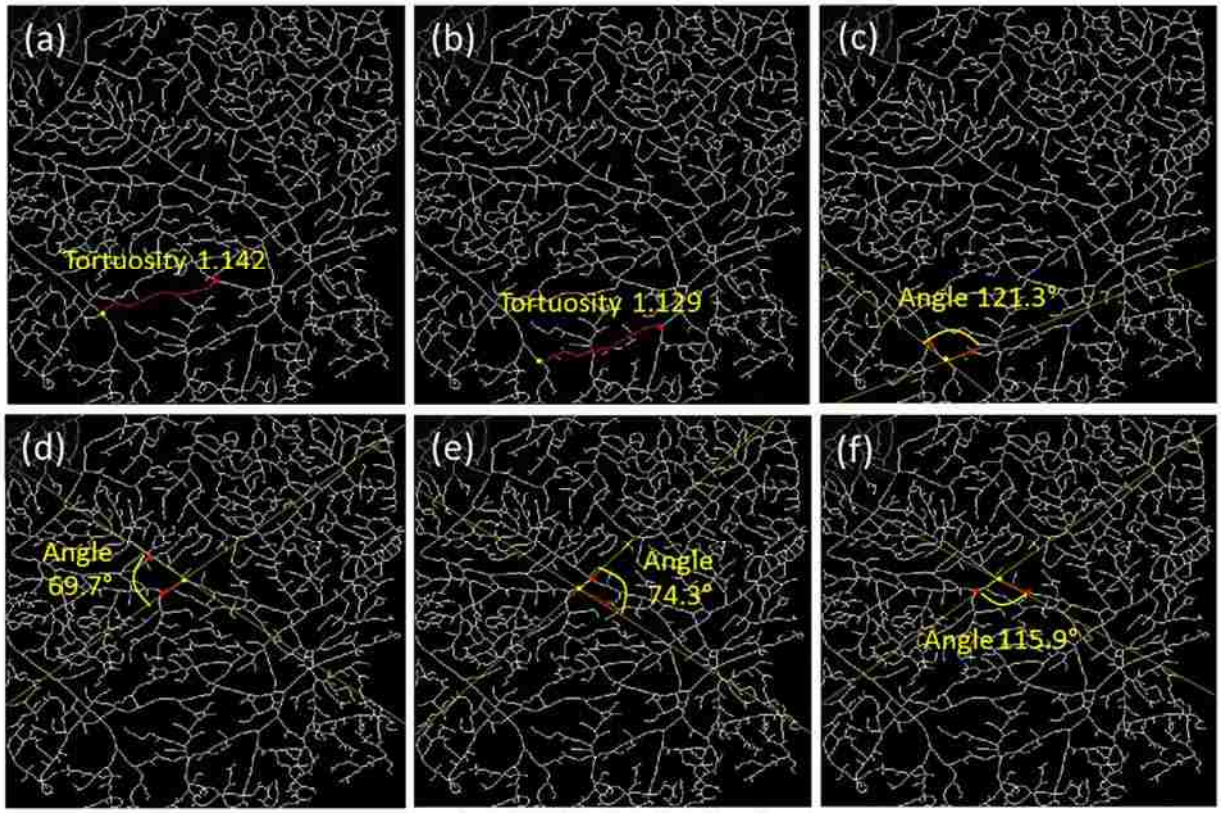

Figure 4.10. (a) and (b) vessel tortuosity analyses of 2 arterio-arterial anastomosis vessels. Red curve: traced vessel branch. (c) - (f) Analyses of branching angles toward four different orientations. Yellow line: linear fitted instantaneous flow direction from the first 10 pixels of each branch. Yellow dot: starting. Red dot: ending.

The demonstrated methods and additional quantitative parameters of the vasculature pattern including vessel area density [61], vessel skeleton density [61] and vasculature fractal dimension [143] have been integrated into a comprehensive GUI vasculature analysis platform, which is written by PyQt5 and Python 3.6. Please refer to the supplementary file (video 1) for more details about the operation flow.

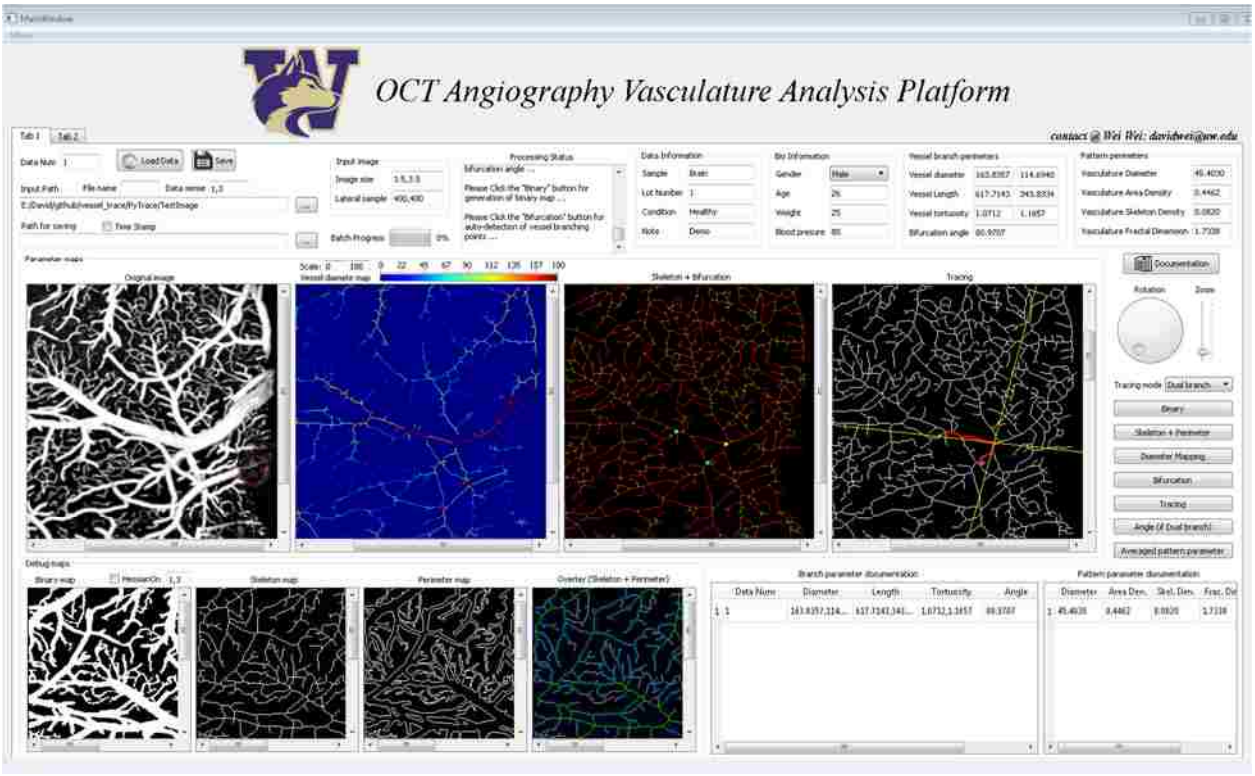

Figure 4.11. GUI OCT angiography vasculature analysis platform.

4.6 Discussion and conclusions

In this paper, we present an innovative approach for analyzing OCTA images through automatic vessel diameter quantification and automatic vessel tracing. The diameter is obtained by gradient-guided measurement of the mimimum radial distance between the vessel skeleton and the vessel perimeter. We prefer to calculate the MRD, instead of calculating the curvature of skeleton segments and radially searching/counting pixel numbers, for the following two reasons. (1) calculating curvature is practically more complicated and inconsistent. For instance, the calculated curvature dramatically fluctuates for the segments shown in the blue boxes in Figure 4.12 (zoomed subfigure). (2) The radical search may severely overestimate the vessel diameters at the corner or branching regions. For example, in Figure 4.12 (zoomed subfigure) the quantified diameter by

MRD (yellow) can be overestimated as the length of vessel segment (green line), if radical searching is directly applied.

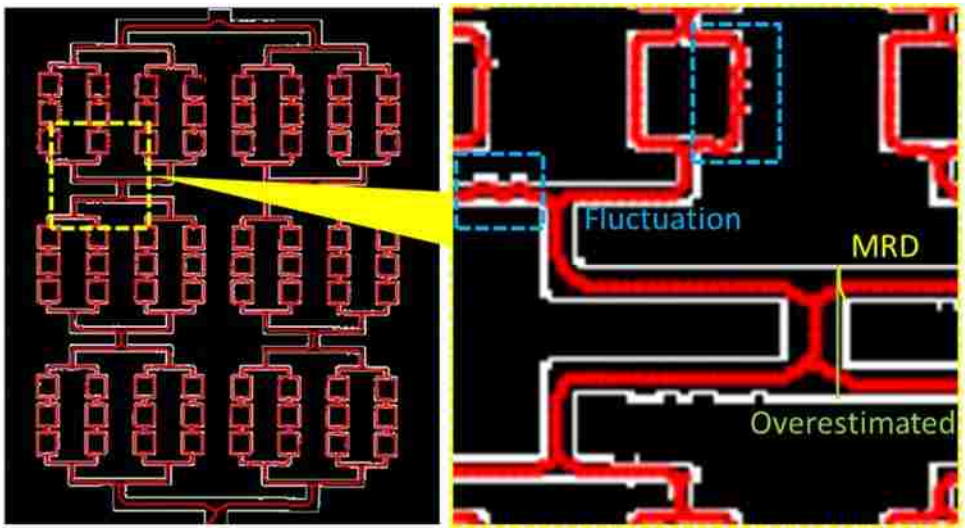

Figure 4.12. The preference of MRD over curvature guided radical searching. Blue boxes: the vessel segments in which the calculation of curvature is inconsistent. Yellow line: the quantified diameter at the branching region by MRD. Green line: the overestimated diameter at the branching region by curvature guided radical searching.

In the diameter quantification, one limitation exists for vessels with 90 degree corners as indicated in Figure 13(a), where the maximum overestimate can be ~20%. However, 1) this overestimate only occurs within a restricted small region, and even within this region the overstimate decreases rapidly following $(1-\cos(\theta'))/2\cos(\theta')$, where θ' is the off-set angle between the radical line and the horizontal line (or its complement angle if it's larger than 45°), as schematically shown in (a); 2) *in vivo*, vessels bend at angles much smaller than 90 degree, in order to maintain smooth blood flow. During vessel tracing, an A* path searching algorithm was applied to the skeletonized vessels. However, as representativly indicated by the blue circles in Figure 13(b) - (c), the vessel skeletonization may fail at regions where large vessels are branching. Therefore, the traced skeleton pixels should be excluded from analysis if located within a given distance from the bifurcation center. In practice, this distance is designed as the maximum radius of connected vessel branches (i.e. half of the blue dashed lines in (b)). This is analogous to the

analysis of conventional microscopic images, where care is generally taken to avoid measurements very close to the branching points [133].

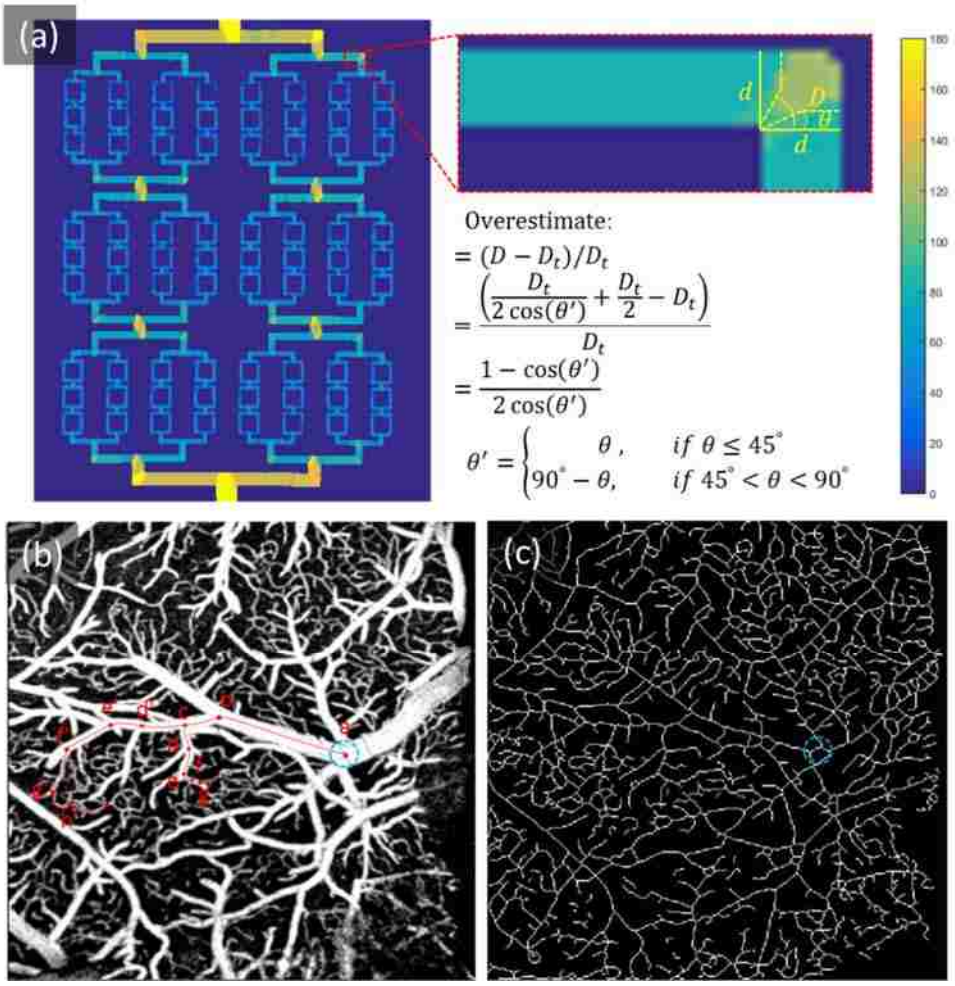

Figure 4.13. Limitation analyses of the proposed diameter quantification and vessel tracing. (a) Redisplayed figure same as Figure 4.3(i), in which a 90 degree corner is zoomed for error calculation. D: quantified diameter; D_t: true diameter; θ: off-set angle between the radical line and the horizontal line. (b)-(c) Redisplayed figures same as Figure 8(b) and (c), in which the blue circle indicates a representative region removed from quantification due to poor vessel skeletonization. In (b), the blue dash line indicates the diameter of the circle which is equal to the maximum diameter of connected vessel branches.

In addition to the algorithms, the use of imported OCTA images for vessel characterization has its own limitations. Due to the restricted lateral resolution of the OCT system, the diameters of small capillaries are likely overestimated to some extent. Despite this limitation, we demonstrated that our algorithm quantifies changes in vessel diameter down to a single vessel branch, with a

degree of accuracy appropriate for clinical use, as visulized in the abnormal cases in Figure 4.5(f) and (l) compared with the healthy one in Figure 4.3(i). Other techniqual developments including using optical coherence microscopy [144] or adaptive optics OCT [145] would provide representation of the vasculature with higher resolution, and therefore improve quantification accuracy.

For the clinical use of our algorithm, the computation cost/time is another important parameter to consider. Vessel diameter quantification and vessel tracing was performed in Python 3.6 on a Dell Pression T7500 with an Intel Xeon E5507 CPU (1 of 4 cores were used). The time cost of diameter quantification was ~ 3 s for the microfluidic device and ~ 5 s for the brain vasculature; the vessel tracing cost was ~1 s for all branches listed in Figure 4.9(a). Further improvements can be achieved by using parallel processing with multiple CPU-cores, or alternatively adopting a GPU, which would reduce the computation time exponentially.

In conclusion, we developed an automated framework to quantitatively characterize vessel diameters down to individual capillaries. We validated our algorithm, and compared it to a clinically well-accepted method, by imaging and quantifying microfluidic flow phantoms with known vascular parameters. Compared with the currently clinically accepted method, our approach quantified vessel parameters with superior consistency, accuracy, and a high tolerance to deviations in vessel orientation. We used an A* algorithm to trace vessel branches, and accordingly calculate the mean diameter of each vessel branch. The heuristic A* algorithm provides an effective and efficient way to get positional information for individual vessels down to the capillary level. Finally, the proposed algorithms were applied to extract vessel parameters from the mouse cerebral vasculature *in vivo*, including vessel diameter, tortuosity, and branching angle, which agreed well with findings in the literature. Our algorithmic approach is highly adaptable,

and can easily be extended to other imaging modalities such as two-photon fluorescence microscopy and photoacoustic microscopy, making it of potential interest for use in multiple clinical settings.

5. Summary and related future plans

5.1. Summary

In this thesis, we developed multifunctional OCT cerebral angiography techniques, including systems, scanning strategies and algorithms, to map the vasculature network and quantitatively analyze the capillary hemodynamics within mouse cerebral cortex. The whole thesis is divided into three parts. Firstly, we applied the state-of-art OCT capillary velocimetry to explore the capillary transit characteristics mainly represented by mCTV, TFB and variations within such upon electrical stimulation, and accordingly interpreted the hemodynamic mechanisms in neurovascular coupling and the metabolic benefits of functional hyperemia (chapter 2). This will expand current understandings about the cerebral microcirculation and contribute to the development of quantitative OCT for brain imaging in the OCT community. Secondly, we designed an OCT penetrating vessel mapping approach allowing for rapid and automatic identifications of cerebral penetrating vessels from large volume datasets, free from the tailing artifacts that is inevitable in other approaches. We then combined this method with other OCT techniques (including OCT angiography and capillary velocimetry discussed in chapter 1) for comprehensive evaluation of the cerebral vascular hierarchy (chapter 3). This fills in the gap where effective penetrating vessel mapping is still missing, when angiography techniques for the surface and subsurface vasculature are maturing. Thirdly, we demonstrated a comprehensive vasculature analysis framework for the morphological investigation of the cortical surface vessels, with newly designed methods for vessel diameter measurement and vessel tracing (chapter 4). The proposed algorithms were used to extract quantitative vascular matrixes from the *in vivo* OCT angiography results, including vessel diameter, tortuosity, branching angle, et al, accelerating the clinical translation of OCT angiography in a more quantitative manner.

5.2. Future plan

For the first part, in the future, a rigorously investigation of the correlations in capillary transit parameters need to be carried out. However, the regulation of capillary blood flow in mouse cerebral cortex is extremely complex, and is additional affected by the experimental conditions, e.g. the dosage for isoflurane anesthesia. In order to minimize the effect of isoflurane anesthesia, we may need to switch to Ketamine injection or even imaging the awake mice with the recently renewed lab protocol. This can be difficult and requires long-term efforts. Another research development is incorporating the electrical stimulation with mouse cortex at abnormal states, for instance the aged brain or the one with ischemia stroke, to investigate the therapeutic benefits of functional hyperemia and their correlations with the capillary transit parameters. Specific aims are listed as follows:

Aim 1: Apply the established quantitative correlation analysis in chapter 2 to study the capillary transit parameters of aged mouse subjects (24-month-old) before and during electrical stimulation; compare the mCTV, TFB and variations within such between the young (data shown in *2.3.1 – 2.3.5* in chapter 2) and the old in the activated somatosensory cortex region. The objective is to see if aging has negative effects on the neurovascular coupling and associated hemodynamic responses in brain.

Aim 2: Apply the established quantitative correlation analysis in chapter 2 to study the capillary transit parameters of mouse subjects (2-month-old) after dMCAO stroke; compare the mCTV, TFB and variations within such before and during electrical stimulation in the activated somatosensory cortex region. The objective is to see if the metabolic benefits of functional hyperemia lead to a therapeutic hemodynamic response in stroke.

For the second part, although our PVM technique shows some tolerance to the vessels with imperfect perpendicular penetration (please see 3.4 in chapter 3 for details), the exact degree of tolerance is still unclear. One of the future work will be 3D printing microfluidic channels to mimic the cerebral hierarchical angioarchitecture for a systematic tolerance test. Another plan is resolving the directional information in the penetrating vessel map, i.e. distinguishing between penetrating arterioles and ascending venules, by utilizing the phase information in the complex OCT signal. Preliminary results about this direction-resolved PVM have revealed decent feasibility but the method requires more mathematical analysis and optimization. Specific aims are listed as follows:
Aim 1: Print 3D microfluidic channels to mimic hierarchical cerebral vasculature, in which penetrating channels should have multiple tilting angles (0°, 10°, 20°, 30°, 40°, 50°) and channel sizes (30 μm, 50 μm and 100 μm); image the channels with intralipid (1%) flowing inside; and resolve penetrating vessel patterns through the method proposed in chapter 3; quantitatively analyze the correlations between penetrating vessel areas and the tilting angles / channel sizes.
Aim 2: Develop add-on algorithms to distinguish penetrating arterioles and ascending venules by utilizing the phase information in the complex OCT signal.

For the third part, we will continue to build an OCT/OCTA package fully written by Python (with documented multi-functional libraries and multi-module GUI platforms), which integrates the SD-OCT data acquisition, the OCTA raw-data processing and the OCTA vasculature analyses.

Apart from the plans related to the studies of cerebral vasculture in chapter 2 – 4, we have an entire new project on-going for the quantification of the subcellular motion of neuron cells in brain *in vivo*. The basic concept of the project is resolving subcellular dynamics from variations of OCT signal with relatively low-resolution optics. Some of the preliminary results will be discussed in the next chapter.

6. Future project: Dynamic imaging and quantification of subcellular motion in cortical brain with eigen decomposition OCT variance analysis

Purpose of this project: Characterize the cortical cell dynamics by 1) developing a high-sensitive approach to resolve OCT signal variations stemming from subcellular motion; 2) validating the proposed method with cell phantoms; 3) applying the developed algorithm to investigate the cortical cells *in vivo*.

6.1. Introduction

The measurement of subcellular motion provides a convenient and effective means in the evaluation of cell metabolism and testing the responses of cells to pathogens and drugs in pharmaceutics [146][147]. Over the past decades, numerous optical imaging techniques have been explored to non-invasively assess the subcellular dynamics, typically through the measurement of spatial and temporal subcellular behaviors [148]. Fluorescence correlation spectroscopy has been used to quantify the diffusive properties in the cells through evaluating the autocorrelation of fluctuations in fluorescent signals [149]. Without a need for exogenous agent, phase contrast microscopy and quantitative phase microscopy have been extensively utilized to investigate subcellular dynamics by resolving optical phase changes due to cell growth, metabolism, and volume/mass changes [150]–[152]. However, the limited field of view and the relative low throughput limit their applications toward massive drug screening in pharmaceutical engineering.

OCT has emerging as an invaluable tool for 3-dimensional imaging of biological tissues/cells through highly-scattering medium with cellular level resolution, high throughput and high efficiency [153]. Since the OCT signals from static tissue structures are relatively constant, the motion signal of interest can be isolated by time varying measurement (i.e. time lapse acquisition)

together with dynamic processing methods. The conventional processing methods include standard deviation (STD) [146], [154], differentiation [6], [155] or decorrelation [156], [157] of signal intensities. As only the intensity is utilized here, these methods may not be sensitive to subtle phase changes in the OCT signals. Recently, more and more attention has been paid to the sensitivity advantages of complex dynamic processing where both the signal intensity and phase are utilized to assess the dynamics [11], [121]. Lee et. al proposed a dynamic light scattering OCT (DLS-OCT) using complex autocorrection and subsequent mathematical modeling to study particle motions [158], [159]. Farhat et. al investigated the DLS-OCT signal to infer the intracellular dynamics as cells underwent apoptosis [160]. Very recently, the use of complex/phase decorrelation of the OCT signal was demonstrated to improve the imaging contrast [161], which has been explored to detect random motions in cornea tissue samples [162].

In this chapter, we report the development of an innovative approach to contrast subcellular motions by using eigen decomposition (ED) based variance analysis of time-varying complex OCT signals. With comparative test on abiotic phantoms made of intralipid and gelatin of different concentrations, the ED based method reveals superior sensitivity to the dynamic signal (i.e. higher contrast to noise ratio (CNR) [6]) compared to that of intensity-based decorrelation (ID) analysis. We then test the proposed approach on purposely patterned samples of yeast powder mixed with gelatin/TiO_2 water solution to demonstrate the ED analysis in revealing subcellular dynamics of yeast cells. To evaluate the decay of complex signal variation, we describe a method to quantify the power of uncorrelated static and dynamic components with the eigen values from ED analysis. Finally, the method is applied to image mouse cerebral cortex *in vivo*, in normal state and when suffering from ischemic stroke, suggesting the potential ability of ED variance analysis to investigate cortical neural activities.

6.2. Materials and methods

6.2.1. OCT system setup

A phase-stable spectral domain OCT system was utilized, similar to that described in [163]. In brief, the system worked at a center wavelength of 1310 nm and a spectral bandwidth of 110 nm, providing an axial resolution of ~ 7 μm. In the sample arm, a 10X objective lens was employed, which provided a lateral resolution of 7 μm at full width of half maximum. With incident light power of 3.5 mW, the system sensitivity was measured to be ~105 dB. The phase stability of the obtained interference OCT signal was optimized to be ~1.5 mrad, providing a sub-nanometer-scale displacement sensitivity (~ 0.16 nm in air). The imaging was operated following multiple designed BM-mode (i.e., repeated B-scans over time) and MB-mode (i.e. B-scan is completed by stepped A-lines, with each step consisting of repeated A-lines over time) scanning protocols. The sampling rate of BM-mode imaging was kept at 180 fps, and that of the MB-mode imaging was 20 kHz. The acquisitions at short time scale that dominated by Brownian motion promise the detection of subcellular dynamics with negligible cellular migration or reorganization [146].

6.2.2 Sample preparations, scanning protocols and data processing

We respectively designed 3 individual experiments for 1) demonstrating the sensitivity advantage of ED algorithm performed on the complex OCT signals of abiotic phantoms; 2) validating the ED-based imaging and quantification of subcellular dynamics in yeast cells; 3) demonstrating the *in vivo* application of the ED quantification on monitoring cortical cell necrosis after stroke.

6.2.2.1 Phantom experiment for sensitivity test

The first set of experiments were designed to demonstrate the sensitivity advantage of the complex ED algorithm [34]. For what follows, we refer this set of experiments to Experiment I for brevity. Here, we sought to use more controllable abiotic phantoms for the reason that it is difficult to directly employ cells whose activities are sensitive to temperature, humidity, pH et al. In the preparation, a series of phantom samples were fabricated with a constant concentration of intralipid scattering particles (particle diameter of ~0.5 μm) but with a varied degree of gelatin concentrations, in which the dynamic behavior of suspended intralipid was used to mimic pedesis-like subcellular dynamics [160]. Specifically, 0.04% titanium dioxide (TiO_2) was mixed with 25% gelatin to mimic the scattering background. At the front side of the background tissue, cone-shape holes were drilled side by side to form solution reservoirs. Next, distilled water and various amount of gelatin powders were blended and heated in a water bath at ~80 °C for 20 min and stirred periodically to prepare gelatin solutions with weight concentrations of 0%, 1%, 2%, 4%, 6%, 7%, 8%, 9%, 12% and 15%, respectively. When the solution samples cooled down to 60 °C, 0.2 mL, each was taken to mix with 0.2 mL 2% intralipid solution, and then poured into the prepared reservoirs and allowed to solidify for 3 min. The phantoms thus prepared were finally subjected to OCT imaging.

In this experiment, we acquired 3D OCT scans from each phantom for later data processing to demonstrate the sensitivity advantages of ED based algorithm. Each 3-D scan was comprised of 400 B-frame positions, 8 frame repetitions at each B-scan position, and 400 A-lines in one B-frame, covering a field of view of 5 × 5 mm. The pedesis-like motions were detected by applying ED [34] and ID [33] analyses, respectively, and the extracted dynamic signals were then projected onto the *en-face* plane through maximum intensity projection (MIP). For comparison purpose, the contrast

to noise ratio (CNR) of resulting images were calculated with respect to each gelatin concentration as [161]:

$$CNR = (\mu_s - \mu_b)/\sqrt{\sigma_s^2 + \sigma_b^2}, \quad (6.1)$$

where μ_s and σ_s are the mean and STD of the signal region of interest (typically a region in the middle of FoV with a radius = 1 mm), and μ_b and σ_b are the mean and STD of the surrounding background region (2 mm < radius < 2.5 mm, which is outside of the intralipid contained reservoir).

6.2.2.2 Yeast experiments to mimic subcellular dynamics

To validate the proposed quantitative ED variance analysis, we prepared and imaged yeast cells, a highly-polarized cell type that is particularly sensitive to mitochondrial activities [164]. The yeast phantom was designed by 1) filling the cement-like yeast/gelatin/TiO_2 mixture (15% yeast, 15% gelatin, 0.04% TiO_2) into the carved gelatin/TiO_2 (15% gelatin, and 0.04% TiO_2) solid background; 2) adding yeast powder suspension (15% yeast) into the 60 °C water solution containing 15% gelatin and 0.04% TiO_2. Two different yeast phantoms were prepared for this set of experiments (Experiment II) (please see justification in the *Results and discussion*). The phantoms were imaged after allowing 5 hrs for full solidification.

The phantom was first imaged by a 3D scan mode, which was comprised of 1000 B-frame positions, 16 frame repetitions at each B-frame position, and 400 A-lines in one B-frame, covering a field of view of 3 × 7.5 mm. The subcellular dynamics were detected by using ED only and *en-face* projected through MIP. Additionally, as shown in Figure 6.1(a), BM-mode scanning of 200 A-lines and 1800 frame repetitions, and MB-mode scanning of 600 A-line repetitions and 200 positions, were respectively adopted to image the yeast and gelatin/TiO_2 phantoms. The data

processing flow chat is displayed in Figure 6.1 (b)-(e), and illustrated respectively as following steps (i)-(iv):

(i), Every two complex A-line samples (A_1, A_τ) with time-varying intervals ($\tau = \Delta t, 2\Delta t \ldots (N-1)\Delta t$) were grouped as a cluster (Figure 6.1b).

(ii), A 2 × 2 covariance matrix (R_c) was then obtained via normalized multiplication between the conjugate transposed cluster and the cluster itself:

$$R_c^\tau = \frac{1}{M}\begin{bmatrix}(A_1^*)^T \\ (A_\tau^*)^T\end{bmatrix}[A_1\ A_\tau] = \frac{1}{M}\begin{bmatrix}A_1^* \cdot A_1 & A_1^* \cdot A_\tau \\ A_\tau^* \cdot A_1 & A_\tau^* \cdot A_\tau\end{bmatrix} = \begin{bmatrix}var(A_1) & covar(A_1, A_\tau) \\ covar(A_1, A_\tau) & var(A_\tau)\end{bmatrix} \quad (6.2)$$

in which, * represents the complex conjugate, T represents the transpose, and M is the number of depth samples in each A-line.

(iii), Because the static structure and the pedesis-like random dynamics are linearly uncorrelated, the static and dynamic components can be separated by minimizing the intergroup correlations. In doing so, the ED diagonal transformation was utilized where the covariance matrix (Figure 6.1c) is projected onto orthogonal (linearly uncorrelated) direction that optimizes the difference between the two components as in:

$$R_c^\tau = E^\tau \Lambda (E^\tau)^{*T} = E^\tau \begin{bmatrix}\lambda_1^\tau & 0 \\ 0 & \lambda_2^\tau\end{bmatrix} (E^\tau)^{*T} \quad (6.3)$$

where Λ is the transformed diagonal matrix, in which the first eigen value (λ_1) represents the power of static component since structure information dominates in OCT signals, and the second eigen value (λ_2) represents the power of dynamic component (Figure 6.1d). E is a 2 × 2 matrix of eigen vectors that represents the transformation coefficients.

(iv), Finally, the dynamic motion was evaluated by the ratio of the static power to the total power along time axis. According to the dynamic behavior of Brownian particles in which the fraction of static particles approximately follows exponential decay [165], this static power ratio

(PR^{τ}) should decline exponentially, which thus provides a quantitative assessment of motion signals through the fitted damping coefficient (Γ), as expressed by the following equation [165]:

$$PR^{\tau} = \frac{\lambda_1^{\tau}}{\lambda_1^{\tau}+\lambda_2^{\tau}} = C \cdot \exp(\Gamma \cdot \tau) \tag{6.4}$$

where PR is the power ratio, and C is the peak static power ratio that approximately equals to 1. As a negative decay coefficient, the faster the decay rate, the lower the Γ will be. Figure 6.1(e) shows a decline curve of a representative gelatin/TiO_2 phantom (15% gelatin and 0.04% TiO_2), and an exponentially fitted dash curve with Γ = -0.055 /s, C = 1.04, and coefficient of determination R^2 = 0.98 (Figure 6.1e).

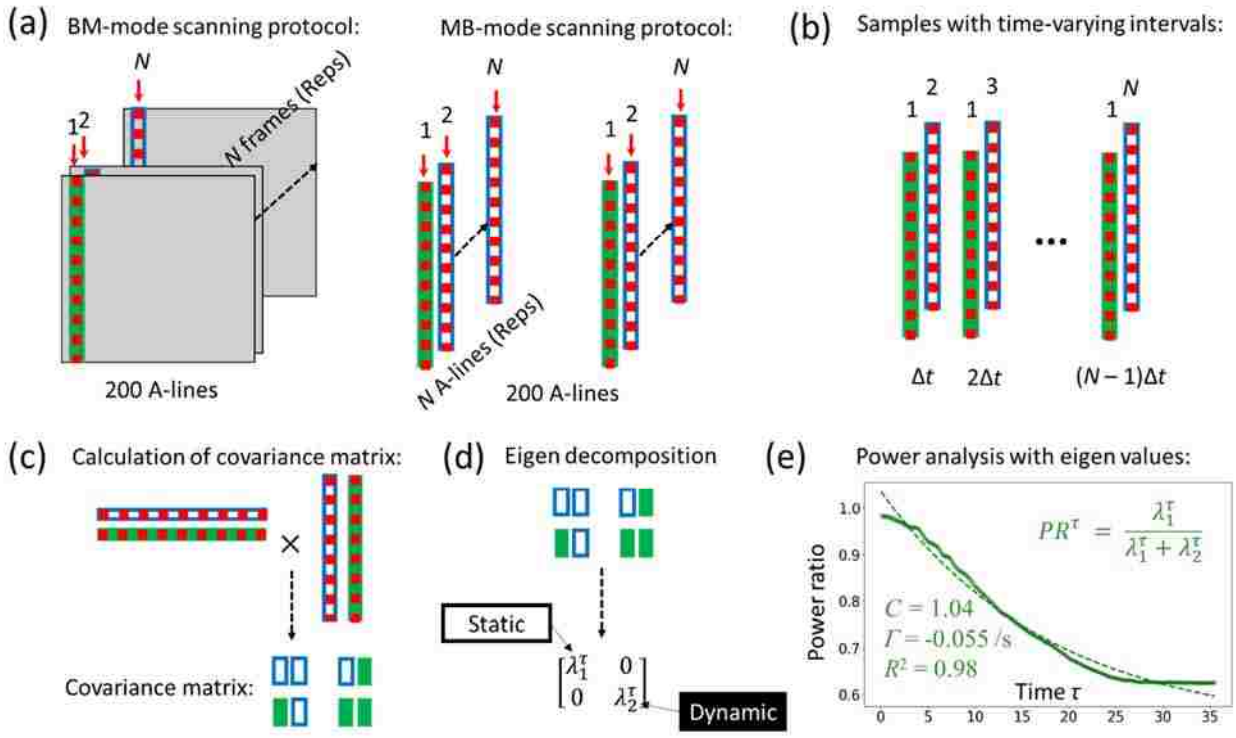

Figure 6.1. Imaging and data processing of power analysis of complex OCT signals. (a) Representative BM-mode scanning protocol where the B-scan (consisting of 200 A-lines) was repeatedly scanned by N times. (b) Every two samples with time-varying intervals are grouped as a cluster. (c) Calculation of correlation matrix between two samples in a cluster. (d) Complex eigen decomposition that optimizes the differentiation between two groups: static and dynamic, in which the eigen value is used to evaluate the power of each group. (e) Power analysis by calculating the ratio of static eigen value to the total power over time from ED processing. Solid curve is the static power ratio evaluated from a representative gelatin/TiO_2 phantom (15% gelatin and 0.04% TiO_2) against the time frames (~ 35 s), and a dash curve shows the exponentially fitted decline of the power ratio. N: temporal sample number; Δt: time interval; τ: time; λ: eigen value; PR: static power ratio; C: fitted peak static power ratio, Γ: fitted damping coefficient, R^2: fitting coefficient of determination.

6.2.2.3 Animal brain imaging in vivo

In Experiment III, a 2-month C57BL/6 mouse subject to ischemic brain injury (i.e., stroke) was used to demonstrate the potential *in vivo* application of the proposed method to cortical tissue integrity. The animal handling follows the same procedures as described in [163], which had been reviewed and approved by the Institutional Animal Care and Use Committee (IACUC) of University of Washington. In short, the mouse was initially prepared through an open-skull cranial surgery above the somatosensory cortex. Then, at the same location, a regional ischemic injury [166] were surgically induced with occlusion of the middle cerebral artery, which subsequently led to cortical cell necrosis due to the inhibition of cell activities caused by the injury.

In this experiment, to balance the spatial-temporal sampling and the total acquisition time for *in vivo* imaging, MB-mode scans at 400 × 400 positions and 50 A-line repetitions at each position were acquired for each 3-D dataset, covering a field of view of 3 × 3 mm. The ED variance analysis of A-lines was the same as in Experiment II. Meanwhile, in order to focus on the neural activity, the blood flow information at each cross-section was removed by taking the OCT angiography cross-section (including all arterioles, venules and capillaries) as a mask [121]. The exclusion of flowing scatters ensures that the detected signals are mainly contributed by cerebral tissue dynamics, which may include those from neuronal or other cell types such as glial cells, astrocytes etc.

6.3. Results and discussions

6.3.1 Complex ED reveals superior sensitivity to dynamics

Figure 6.2(a) shows the photograph of the motion phantoms fabricated for Experiment I. The *en-face* OCT structural images of reservoirs filled with gelatin/intralipid of different gelatin

concentrations are displayed in Figure 6.2(b). The corresponding MIP dynamic images using ED and ID are respectively shown in Figure 6.2(c) and (d). According to equation (6.1), the variations of CNR with respect to gelatin concentrations are plotted and analyzed as in Figure 6.2(e), demonstrating that the sensitivity of complex ED method is close to twice that of the ID method.

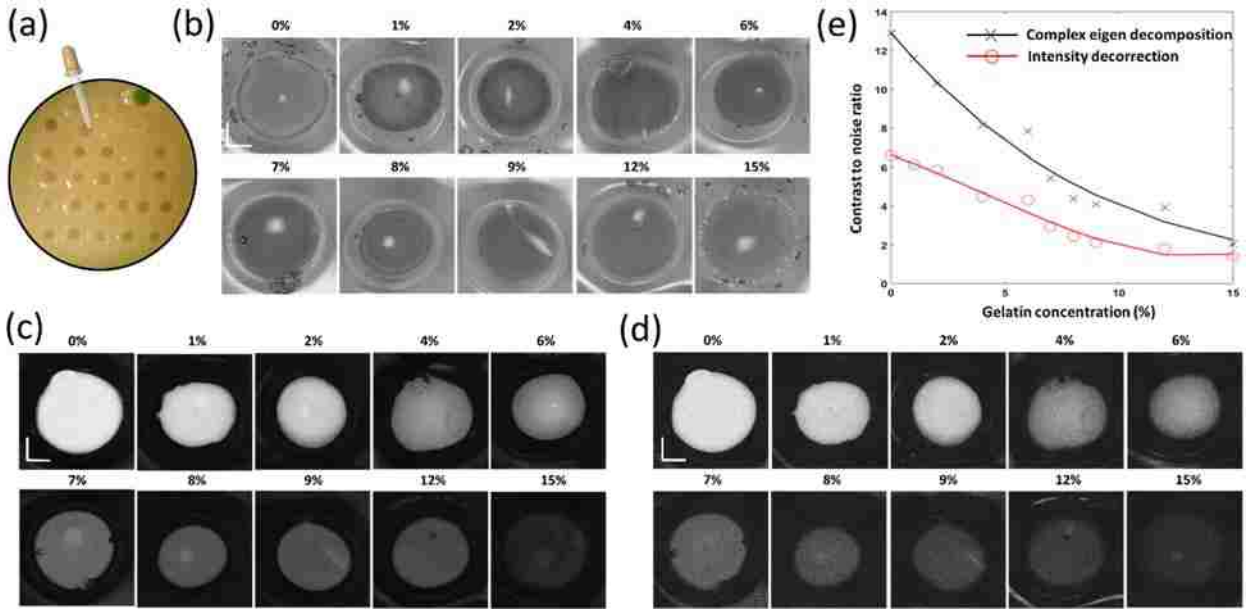

Figure 6.2. The sensitivity to motion of complex eigen decomposition (ED) method is approximately twice that of intensity decorrelation (ID). (a) photograph showing the phantom with motion-particle containing reservoirs arranged side by side. (b) *En-face* OCT structural images of the reservoirs with the gelatin concentrations as shown. (c) and (d) *En-face* dynamic images using ED and ID with respect to different gelatin concentrations, respectively. (e) Descending curves of CNR of two dynamic imaging algorithms with increasing gelatin concentration. Scale bar: 1 mm.

6.3.2 Subcellular dynamics in yeast cells are detected and quantified by ED variance analysis

In Experiment II, the patterned phantoms made by yeast/gelatin/TiO_2 mixture were used to visualize cell dynamics. As schematically shown in the yeast intercellular structure in Figure 6.3(a), the subcellular motions of yeast cells are mainly driven by mitochondrion activities [160]. Figure 6.3(b) shows an "OCT-UW" letter pattern grooved on the gelatin/TiO_2 background that was filled with the yeast mixture, which was contrasted through complex ED as in Figure 6.3(c). Corresponding to the red lines in (b) and (c), the cross-sectional structure image and dynamic image of the yeast/gelatin/TiO_2 mixture are displayed in Figure 6.3(d) and (e). At this location, the

repeated B-scans were acquired and piled up as a time-dependent sequential datum. The power ratio (i.e. percentage ratio of static eigen values) are mapped against the time axis (vertical axis) as in Figure 6.3(f). By averaging across all A-lines, the curve in (g) reveals a rapid decline of the static component of the yeast mixture. In comparison, as marked by green lines in (b) and (c), the structure image, the dynamic image, the map of power ratio decay, and the averaged decay curve of pure gelatin/TiO_2 are shown in Figure 6.4(h)-(k), respectively. As expected, for abiotic elastic materials like gelatin, the decline of static power ratio is approximately linear within 10 s, much slower than that of the yeast cells. In (g) and (k), the time-varying curves within 3 s are zoomed as subfigures, and exponentially fitted, respectively. However, as suggested by the poor fitting in (g) (i.e. $R^2 = 0.60$), the dynamic property of yeast phantom is difficult to quantitatively characterize with current sampling frequency of 180 Hz. Therefore, a higher speed of 20 kHz with M-mode scans is used in the following subsection.

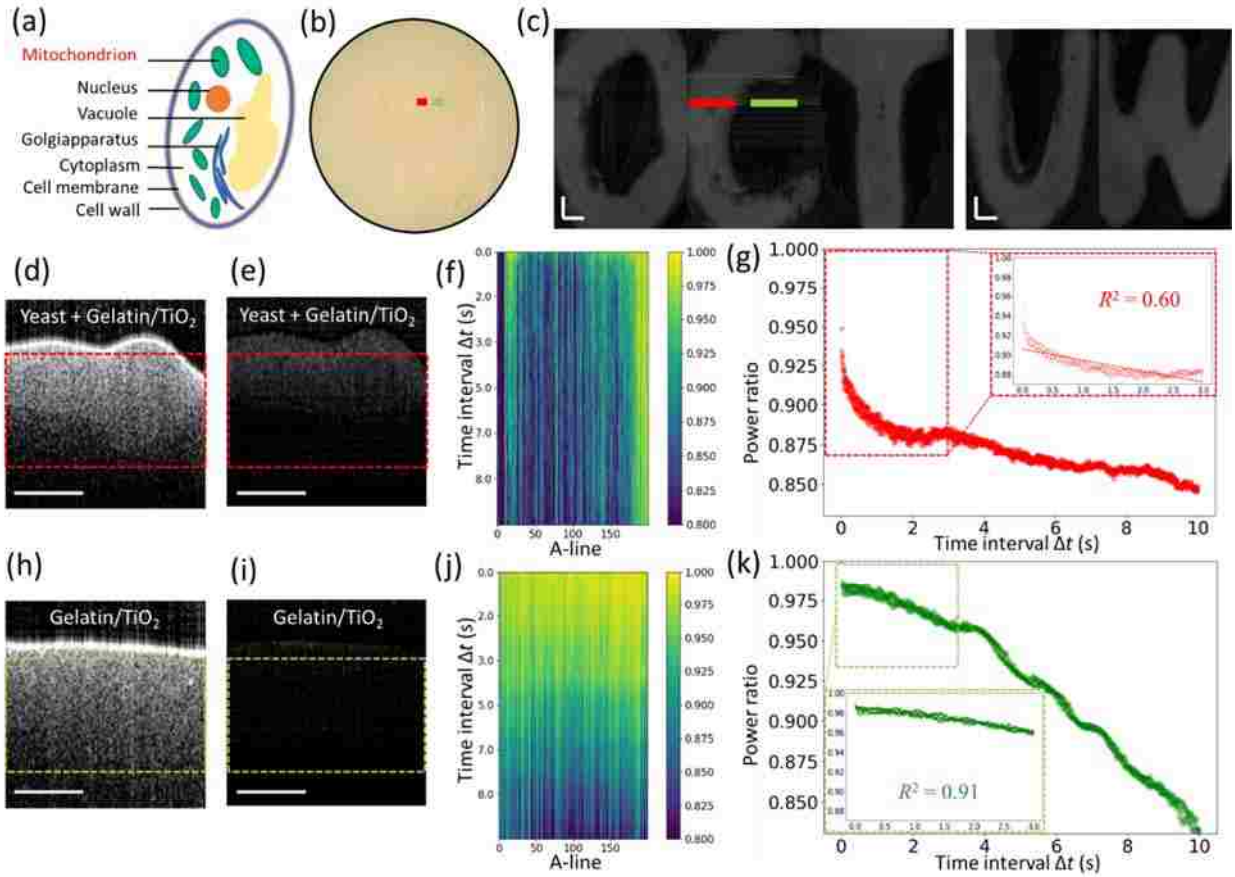

Figure 6.3. Imaging of patterned phantom made of yeast cells and gelatin/TiO_2 (a) Intercellular diagram of a yeast cell. (b) Designed "OCT - UW" letter pattern filled with yeast/gelatin/TiO_2 mixture. (c) *En-face* dynamic images of subcellular motion in yeast/gelatin/TiO_2 mixture against the gelatin/TiO_2 background. (d) and (e) Cross-sectional structure image and subcellular dynamic image of the yeast mixture corresponding to red lines in (b) and (c). (f) Map of the static power ratio against time frames (vertical axis, ~10 s duration) of each A-line (horizontal axis) within the sample window marked as red boxes in (d) and (e). (g) Variation curve of the line-averaged static power ratio of (f). (h)-(k) Structure image, dynamic image, map of static power ratio, and the averaged curve of the pure gelatin/TiO_2 phantom. In (g) and (k), the time-varying curves within 3 s are zoomed and compared between yeast and gelatin. However, the exponential fitting in (g) merely reaches a level of $R^2 = 0.60$, suggesting the limitation of low sampling speed for the investigation of yeast dynamics. Scale bar: 500 μm.

To minimize the effect from rugged yeast-cement surface, another phantom was made in Experiment II by directly dropping 15% yeast suspension into gelatin/TiO_2 water solution before solidification, as shown in Figure 6.4(a), in which the red square indicates a region that was scanned by the OCT system and then processed through complex ED, as displayed in the dynamic image in Figure 6.4(b). The yellow arrows in (b) indicate a few thin-layer yeast clusters peeled off due to surface tension during phantom making, which still provides certain dynamic contrast although having been surrounded by stiff gelatin after coagulation. To avoid the confounding

factor from cell migration, this region was scanned 3 times with a time interval of ~1 min, all of which show the same distribution of yeast clusters. At the cross-section marked by a red line in (b), repeated M-mode scans were acquired at each A-line position and piled up into a time-dependent sequential datum, as representatively shown in the structure of Figure 6.4(c). Corresponding to the regions marked in green and red in (c), the averaged static power ratios are plotted and exponentially fitted as in Figure 6.4(d). The fitted damping coefficients were -0.09 /s (R^2 = 0.96) and -0.22 /s (R^2 = 0.97) for gelatin/TiO_2 and yeast, respectively, suggesting that the subcellular motions in the yeast cells substantially increase signal dynamics within a short period (total acquisition time of 30 ms with a sampling time interval of 50 μs).

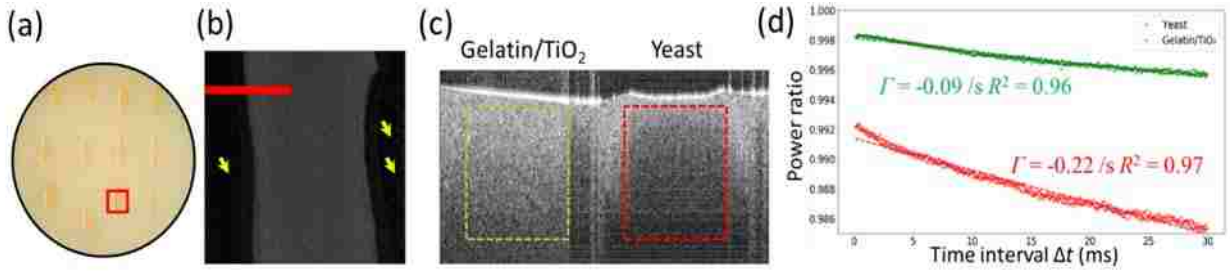

Figure 6.4. (a) Phantom made by adding yeast suspension into gelatin/TiO_2 water solution before solidification. (b) *En-face* OCT dynamic image of the solidified phantom in the red square in (a), in which the yellow arrows indicate thin-layer yeast clusters peeled off due to surface tension. (c) The OCT structure image crossing the boundary between gelatin/TiO_2 and yeast, in which two regions of interest are respectively marked by green and red squares. (d) Corresponding to the regions, the averaged static power ratios are plotted along the time axis, and exponentially fitted in green and red, respectively. The fitted damping coefficient is -0.088 /s (R^2 = 0.96) for the gelatin/TiO_2, and -0.216 /s (R^2 = 0.97) for the yeast.

6.3.3 Quantitative evaluation of cortical cell necrosis after stroke in vivo

In the last experiment, we analyzed the cortical cell activities from *in vivo* OCT datasets, in healthy state and under ischemic stroke. The *en-face* MIP structure image and the blood flow image for the healthy cortex are displayed in Figure 6.5 (a) and (b), respectively. At a representative cross-section marked by red lines in (a) and (b), power ratios of each A-line sample (horizontal axis) are mapped against the time (vertical axis) as in Figure 6.5(c). With respect to each A-line, the variation curve of the static power ratio is further plotted in Figure 6.5(d), in which a black dotted

line denotes the averaged variation. For better visualization of cell dynamics, all cross-sections that are covered by vessels have been removed from analysis in (d). By applying exponential fitting, the averaged damping coefficient (Γ) of entire cross-section is quantified as -5.89 /s. In comparison, the *en-face* structure image, blood flow image, map of static power ratio of a representative cross-section, and corresponding variation curve for the mouse under ischemic stroke are displayed in Figure 6.5 (f)-(i), respectively. The decay rate of the static power ratio in (i) appears to be much slower than that in (d), with an averaged damping coefficient of -3.06 /s. The histogram distributions of the damping coefficient of each A-line in (d) (red) and (i) (green) are displayed as a subfigure in (i), revealing the suppression of cell dynamics in stroke, which suggests the coefficient as a high-sensitive parameter to evaluate neural activities. Accordingly, the damping coefficients (with blood flow information removed) are mapped in Figure 6.5(e) and (j), for the mouse in healthy state and under ischemic stroke, respectively. The faster decay rate (lower coefficients) in (e) is ascribed to the active subcellular dynamics of healthy cortical cells. However, after occlusion of the middle cerebral artery, ischemia-leaded necrosis severely alternated the subcellular properties of those cells, and therefore resulted in a slower decay rate (higher coefficients). For the same reason, a boundary can be visualized between the healthy cortical tissue and the static skull as marked by red arrows in (e), which becomes less defined when the mouse suffered a stroke as in (j).

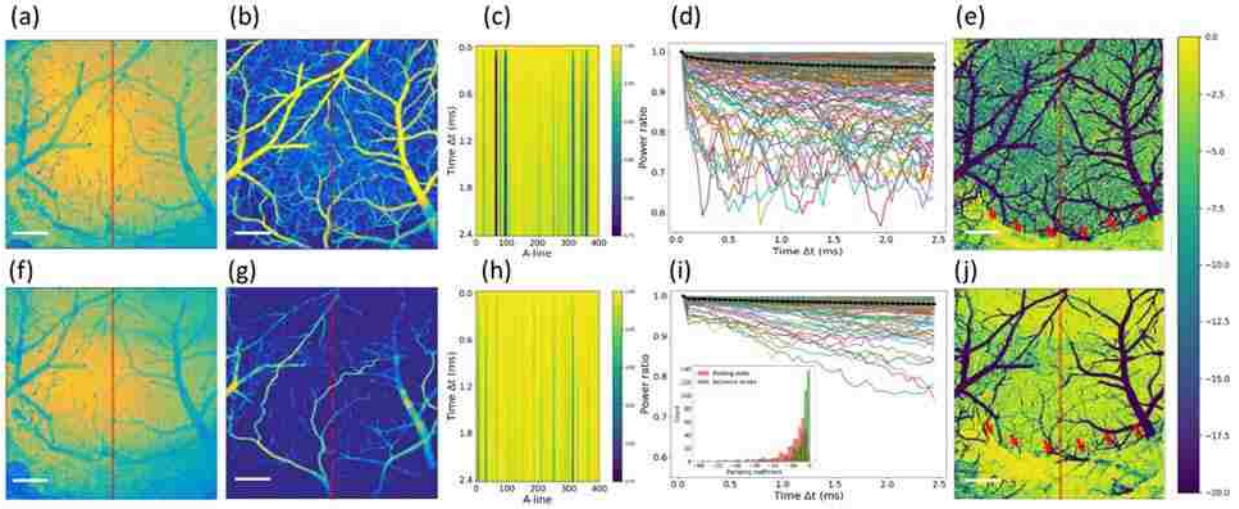

Figure 6.5. Dynamic imaging and ED variance analysis of cortical tissue *in vivo* for a mouse brain subject to ischemic injury. (a) and (b) representative *en-face* OCT structure image and blood flow image of a healthy cortex. (c) Map of the static power ratio against time (vertical axis, 2.5 ms duration) of each A-line (horizontal axis) at the cross-section marked by red lines in (a) and (b). (d) Variation curve of the static power ratio of each A-line in (c), in which the black dotted line denotes the averaged curve with an exponentially fitted damping coefficient of -5.89 /s. (e) Map of the damping coefficients that reveals the subcellular dynamics of healthy cortical cells. (f)-(j) representative *en-face* structure image, blood flow image, map of static power ratio of a cross-section, variation curve of the static power ratio, and map of the damping coefficients for the mouse under ischemic stroke. In (i), the black dotted line denotes the averaged variation curve with a damping coefficient of -3.06 /s. The damping coefficients of each A-line in (d) and (i) are displayed as two histogram distributions in the subfigure of (i) in red and green, respectively. In (e), a clear boundary (denoted by red arrows) is visualized between the cortical tissue and the skull. However, the boundary is less defined in (j). In (e) and (j), all vessels are removed for better visualization of cell activities. Scale bar: 500 μm.

6.4. Discussion and Conclusion

In this study, we have described an innovative quantitative method for the assessment of subcellular dynamics based on eigen decomposition of complex OCT signals. In this method, the differentiation between static and dynamic components is generalized as two main steps: (1) calculation of covariance matrix, and (2) eigen decomposition. Because all A-lines in the 3-D OCT dataset were piled up in the same linear scale, here the covariance matrix is equivalent to its corresponding correlation matrix (correlation coefficient R is calculated by the normalization of covariance against the intra-group standard deviations, i.e. $R = covar(A_1, A_\tau)/(\sqrt{var(A_1)} \cdot \sqrt{var(A_\tau)})$). Therefore, the step (1) shares a similar concept with the well-accepted complex/phase decorrelation theory [161], [167]. However, because of the slow cell-induced signal variation relative to the high sampling speed, apart from the static components, the dynamic

components may also contribute to high correlation, therefore the sensitivity of directly using correlation coefficient can be limited. As the static structure background and the pedesis-like dynamics are linearly uncorrelated, in current approach, we further discriminated the two components through ED in step (2) and calculate the static power ratios by utilizing the eigen values.

In addition, for quantitative analyses, the power ratios are exponentially fitted with the projected *en-face* damping coefficients representing the cell activities. One noticeable phenomenon is that the coefficients of cortical cells in Figure 6.5(e) appear to be around 20 times larger than those of the yeast cells in Figure 6.4(d). This discrepancy may be due to the intrinsic difference in cell types, in the temperatures (body temperature of 36.5° for *in vivo* study compared with room temperature of 20° for *in vitro* study), or even in the cellular motion involvement (e.g. cell migration or reorganization [160], [168]). Also, the stiffness of intercellular media is known to hinder cell migration in the viscoelastic microenvironment, which may compound the observation with possible mechanical origins [169]. However, the migration or reorganization of cells typically cover long timescales [146], [160], [168], way above current sampling interval of 50 μs and total duration of several milliseconds [146]. Other factors may nuance the evaluation of different samples but should be negligible when imaging the same sample in different pathological conditions. In future applications, the experimental conditions need to be carefully monitored and controlled.

Another point to notice is that all samples in the experiments were clustered and processed on a line-by-line basis with no sacrifice of lateral resolution, which is reasonable especially for the spectral domain OCT where the depth information (whole A-line) is acquired at the same time. This is also feasible when studying the responses of cortical cells *in vivo* that usually cover multiple

layers in the cerebral cortex. Further systematic explorations of the layer-dependent responses can be achieved through layer segmentation of the OCT datasets [170] as a pre-processing step.

In conclusion, we proposed an effective ED variance analysis toolkit to achieve dynamic imaging and quantification of subcellular motion. Validation work was successfully performed on various patterned yeasts, gelatin/TiO_2 and intralipid phantoms, suggesting high potential of the toolkit for pharmaceutical engineering. Moreover, the proposed method was employed to indicate cell activities in the mouse cerebral cortex *in situ* and *in vivo*, in normal state and during ischemia stroke. The information of cortical cell metabolism and cerebral blood flow are extracted from the same well co-registered OCT dataset at one time, which may be of great value in future neurovascular coupling studies.

Bibliography

[1] M. E. Raichle and D. A. Gusnard, "Appraising the brain's energy budget.," *Proc. Natl. Acad. Sci. U. S. A.*, vol. 99, no. 16, pp. 10237–9, Aug. 2002.

[2] I. Sack and T. Schaeffter, *Quantification of Biophysical Parameters in Medical Imaging*. 2018.

[3] S. G. Hasselbalch, G. M. Knudsen, J. Jakobsen, L. P. Hageman, S. Holm, and O. B. Paulson, "Brain Metabolism during Short-Term Starvation in Humans," *J. Cereb. Blood Flow Metab.*, vol. 14, no. 1, pp. 125–131, 1994.

[4] S. Hurst, R. K. Wang, S. L. Jacques, A. Gruber, S. R. Hanson, and Z. Ma, "Three dimensional optical angiography," *Opt. Express*, vol. 15, no. 7, p. 4083, 2007.

[5] Z. Zhi, W. Qin, J. Wang, W. Wei, and R. K. Wang, "4D optical coherence tomography-based micro-angiography achieved by 1.6-MHz FDML swept source," *Opt Lett*, vol. 40, no. 8, pp. 1779–1782, 2015.

[6] W. Wei *et al.*, "Intervolume analysis to achieve four-dimensional optical microangiography for observation of dynamic blood flow," *J. Biomed. Opt.*, vol. 21, no. 3, p. 36005, Mar. 2016.

[7] V. J. Srinivasan *et al.*, "OCT methods for capillary velocimetry," *Biomed. Opt. Express*, vol. 3, no. 3, p. 612, Mar. 2012.

[8] V. J. Srinivasan *et al.*, "Micro-Heterogeneity of Flow in a Mouse Model of Chronic Cerebral Hypoperfusion Revealed by Longitudinal Doppler Optical Coherence Tomography and Angiography," *J. Cereb. Blood Flow Metab.*, vol. 35, no. 10, pp. 1552–1560, 2015.

[9] J. Xu, S. Song, W. Wei, and R. K. Wang, "Wide field and highly sensitive angiography based on optical coherence tomography with akinetic swept source," *Biomed. Opt. Express*, vol. 8, no. 1, p. 420, Jan. 2017.

[10] R. K. Wang, Q. Zhang, Y. Li, and S. Song, "Optical coherence tomography angiography-based capillary velocimetry Optical coherence tomography angiography-based capillary velocimetry," *J. Biomed. Opt.*, vol. 22, no. 6, p. 66008, 2017.

[11] Y. Li, W. Wei, and R. K. Wang, "Capillary flow homogenization during functional activation revealed by optical coherence tomography angiography based capillary velocimetry," *Sci. Rep.*, vol. 8, no. 1, p. 4107, 2018.

[12] J. Autio *et al.*, "Spatial Frequency-Based Analysis of Mean Red Blood Cell Speed in Single Microvessels: Investigation of Microvascular Perfusion in Rat Cerebral Cortex," *PLoS One*, vol. 6, no. 8, 2011.

[13] A. Y. Shih, J. D. Driscoll, P. J. Drew, N. Nishimura, C. B. Schaffer, and D. Kleinfeld, "Two-photon microscopy as a tool to study blood flow and neurovascular coupling in the rodent brain," *Journal of Cerebral Blood Flow and Metabolism*, vol. 32, no. 7. pp. 1277–1309, 2012.

[14] S. N. Jespersen and L. Østergaard, "The Roles of Cerebral Blood Flow, Capillary Transit Time Heterogeneity, and Oxygen Tension in Brain Oxygenation and Metabolism," *J. Cereb. Blood Flow Metab.*, vol. 32, no. 2, pp. 264–277, 2012.

[15] E. Gutié Rrez-Jimé Nez *et al.*, "Effect of electrical forepaw stimulation on capillary transit-time heterogeneity (CTH)."

[16] H. Angleys, L. Østergaard, and S. N. Jespersen, "The effects of capillary transit time heterogeneity (CTH) on brain oxygenation.," *J. Cereb. Blood Flow Metab.*, vol. 35, no. 5,

pp. 806–17, May 2015.
[17] D. M. Moody, W. R. Brown, V. R. Challa, H. S. Ghazi-birry, and D. M. Reboussin, “Cerebral Microvascular Alterations in Aging, Leukoaraiosis, and Alzheimer’s Disease,” *Ann. N. Y. Acad. Sci.*, vol. 826, no. 1 Cerebrovascul, pp. 103–116, Sep. 1997.
[18] W. I. Rosenblum and B. W. Zweifach, “Cerebral Microcirculation in the Mouse Brain,” *Arch. Neurol.*, vol. 9, no. 4, p. 414, Oct. 1963.
[19] N. Nishimura, C. B. Schaffer, B. Friedman, P. D. Lyden, and D. Kleinfeld, “Penetrating arterioles are a bottleneck in the perfusion of neocortex,” *Proc. Natl. Acad. Sci.*, vol. 104, no. 1, pp. 365–370, 2007.
[20] J. Nguyen, N. Nishimura, R. N. Fetcho, C. Iadecola, and C. B. Schaffer, “Occlusion of cortical ascending venules causes blood flow decreases, reversals in flow direction, and vessel dilation in upstream capillaries,” *J. Cereb. Blood Flow Metab.*, vol. 31, no. 10, pp. 2243–225495, 2011.
[21] L. Gross, “Redundancy in Cortical Surface Vessels Supports Persistent Blood Flow,” *PLoS Biol.*, vol. 4, no. 2, p. e43, Feb. 2005.
[22] U. Baran *et al.*, “Automated segmentation and enhancement of optical coherence tomography-acquired images of rodent brain.,” *J. Neurosci. Methods*, vol. 270, pp. 132–137, 2016.
[23] W. Drexler and J. G. Fujimoto, *Optical coherence tomography : technology and applications*. .
[24] M. Choma, M. Sarunic, C. Yang, and J. Izatt, “Sensitivity advantage of swept source and Fourier domain optical coherence tomography,” *Opt. Express*, vol. 11, no. 18, p. 2183, Sep. 2003.
[25] T. Feuchter, O. Bang, A. Bradu, N. M. Israelsen, A. G. Podoleanu, and M. Maria, “Resolution dependence on phase extraction by the Hilbert transform in phase calibrated and dispersion compensated ultrahigh resolution spectrometer-based OCT,” in *2nd Canterbury Conference on OCT with Emphasis on Broadband Optical Sources*, 2018, vol. 10591, p. 20.
[26] R. K. Wang, “Optical microangiography: A label-free 3-D imaging technology to visualize and quantify blood circulations within tissue beds in vivo,” *IEEE J. Sel. Top. Quantum Electron.*, vol. 16, no. 3, pp. 545–554, 2010.
[27] A. Mariampillai *et al.*, “Optimized speckle variance OCT imaging of microvasculature,” *Opt. Lett.*, vol. 35, no. 8, pp. 1257–1259, 2010.
[28] J. Fingler, D. Schwartz, C. Yang, and S. E. Fraser, “Mobility and transverse flow visualization using phase variance contrast with spectral domain optical coherence tomography,” *Opt. Express*, vol. 15, no. 20, pp. 12636–12653, 2007.
[29] J. Enfield, E. Jonathan, and M. Leahy, “In vivo imaging of the microcirculation of the volar forearm using correlation mapping optical coherence tomography (cmOCT),” 2011.
[30] L. An, J. Qin, and R. K. Wang, “Ultrahigh sensitive optical microangiography for in vivo imaging of microcirculations within human skin tissue beds,” *Opt. Express*, vol. 18, no. 8, pp. 8220–8228, 2010.
[31] J. Xu, S. Song, Y. Li, and R. K. Wang, “Complex-based OCT angiography algorithm recovers microvascular information better than amplitude- or phase-based algorithms in phase-stable systems,” *Phys. Med. Biol.*, vol. 63, no. 1, p. 15023, Dec. 2017.
[32] S. Yousefi, Z. Zhi, and R. K. Wang, “Eigendecomposition-based clutter filtering technique for optical microangiography,” *IEEE Trans. Biomed. Eng.*, vol. 58, no. 8, pp. 2316–2323,

Aug. 2011.
[33] A. Zhang, Q. Zhang, C.-L. Chen, and R. K. Wang, “Methods and algorithms for optical coherence tomography-based angiography: a review and comparison,” *J. Biomed. Opt.*, vol. 20, no. 10, p. 100901, Oct. 2015.
[34] S. Yousefi, Z. W. Zhi, and R. K. K. Wang, “Eigendecomposition-Based Clutter Filtering Technique for Optical Microangiography,” *Ieee Trans. Biomed. Eng.*, vol. 58, no. 8, 2011.
[35] A. Mishra, J. P. Reynolds, Y. Chen, A. V Gourine, D. A. Rusakov, and D. Attwell, “Astrocytes mediate neurovascular signaling to capillary pericytes but not to arterioles.,” *Nat. Neurosci.*, vol. 19, no. 12, pp. 1619–1627, Dec. 2016.
[36] T. Takano *et al.*, “Astrocyte-mediated control of cerebral blood flow,” *Nat. Neurosci.*, vol. 9, no. 2, pp. 260–267, Feb. 2006.
[37] A. Devor *et al.*, “Suppressed Neuronal Activity and Concurrent Arteriolar Vasoconstriction May Explain Negative Blood Oxygenation Level-Dependent Signal,” *J. Neurosci.*, vol. 27, no. 16, pp. 4452–4459, Apr. 2007.
[38] C. N. Hall *et al.*, “Capillary pericytes regulate cerebral blood flow in health and disease,” *Nature*, vol. 508, 2014.
[39] C. M. Peppiatt, C. Howarth, P. Mobbs, and D. Attwell, “Bidirectional control of CNS capillary diameter by pericytes,” *Nature*, vol. 443, no. 7112, pp. 700–704, Oct. 2006.
[40] R. B. Buxton, K. Uludağ, D. J. Dubowitz, and T. T. Liu, “Modeling the hemodynamic response to brain activation,” *Neuroimage*, vol. 23, pp. S220–S233, Jan. 2004.
[41] Y. Zheng, J. Martindale, D. Johnston, M. Jones, J. Berwick, and J. Mayhew, “A Model of the Hemodynamic Response and Oxygen Delivery to Brain,” *Neuroimage*, vol. 16, no. 3, pp. 617–637, Jul. 2002.
[42] R. B. Buxton, “Interpreting oxygenation-based neuroimaging signals: the importance and the challenge of understanding brain oxygen metabolism,” *Front. Neuroenergetics*, vol. 2, p. 8, 2010.
[43] C. Leithner *et al.*, “Pharmacological Uncoupling of Activation Induced Increases in CBF and CMRO $_2$,” *J. Cereb. Blood Flow Metab.*, vol. 30, no. 2, pp. 311–322, Feb. 2010.
[44] D. C. Poole, S. W. Copp, S. K. Ferguson, and T. I. Musch, “Skeletal muscle capillary function: contemporary observations and novel hypotheses,” *Exp. Physiol.*, vol. 98, no. 12, pp. 1645–1658, 2013.
[45] A. Krogh, “The number and distribution of capillaries in muscles with calculations of the oxygen pressure head necessary for supplying the tissue.,” *J. Physiol.*, vol. 52, no. 6, pp. 409–15, May 1919.
[46] B. C. Fry, T. K. Roy, and T. W. Secomb, “Capillary recruitment in a theoretical model for blood flow regulation in heterogeneous microvessel networks,” *Physiol Rep*, vol. 1, no. 3, 2013.
[47] M. L. Schulte, J. D. Wood, and A. G. Hudetz, “Cortical electrical stimulation alters erythrocyte perfusion pattern in the cerebral capillary network of the rat,” *Brain Res.*, vol. 963, no. 1–2, pp. 81–92, 2003.
[48] S. B. Cox, T. A. Woolsey, and C. M. Rovainen, “Localized Dynamic Changes in Cortical Blood Flow with Whisker Stimulation Corresponds to Matched Vascular and Neuronal Architecture of Rat Barrels,” *J. Cereb. Blood Flow Metab.*, vol. 13, no. 6, pp. 899–913, Nov. 1993.
[49] A. Villringer, A. Them, U. Lindauer, K. Einhäupl, and U. Dirnagl, “Capillary perfusion of the rat brain cortex. An in vivo confocal microscopy study.,” *Circ. Res.*, vol. 75, no. 1, pp.

55–62, Jul. 1994.
[50] J. Vogel and W. Kuschinsky, “Decreased Heterogeneity of Capillary Plasma Flow in the Rat Whisker-Barrel Cortex during Functional Hyperemia,” *J. Cereb. Blood Flow Metab.*, vol. 16, no. 6, pp. 1300–1306, Nov. 1996.
[51] P. L. Leger *et al.*, “Early Recruitment of Cerebral Microcirculation by Neuronal Nitric Oxide Synthase Inhibition in a Juvenile Ischemic Rat Model.,” *Cerebrovasc. Dis.*, vol. 41, no. 1–2, pp. 40–9, 2016.
[52] E. Gutiérrez-Jiménez *et al.*, “Effect of electrical forepaw stimulation on capillary transit-time heterogeneity (CTH),” *J. Cereb. Blood Flow Metab.*, vol. 36, no. 12, pp. 2072–2086, 2016.
[53] D. Obrist, B. Weber, A. Buck, and P. Jenny, “Red blood cell distribution in simplified capillary networks,” *Philos. Trans. R. Soc. London A Math. Phys. Eng. Sci.*, vol. 368, no. 1921, 2010.
[54] V. J. Srinivasan *et al.*, “Quantitative cerebral blood flow with Optical Coherence Tomography,” *Opt. Express*, vol. 18, no. 3, p. 2477, Feb. 2010.
[55] V. J. Srinivasan *et al.*, “OCT methods for capillary velocimetry,” *Biomed. Opt. Express*, vol. 3, no. 3, p. 612, Mar. 2012.
[56] J. Lee, W. Wu, F. Lesage, and D. A. Boas, “Multiple-capillary measurement of RBC speed, flux, and density with optical coherence tomography.,” *J. Cereb. Blood Flow Metab.*, vol. 33, no. 11, pp. 1707–10, Nov. 2013.
[57] J. Tang, S. E. Erdener, B. Fu, and D. A. Boas, “Capillary red blood cell velocimetry by phase-resolved optical coherence tomography,” *Opt. Lett.*, vol. 42, no. 19, p. 3976, Oct. 2017.
[58] J. You, C. Du, N. D. Volkow, and Y. Pan, “Optical coherence Doppler tomography for quantitative cerebral blood flow imaging.,” *Biomed. Opt. Express*, vol. 5, no. 9, pp. 3217–30, Sep. 2014.
[59] B. Li, J. Lee, D. A. Boas, and F. Lesage, “Contribution of low- and high-flux capillaries to slow hemodynamic fluctuations in the cerebral cortex of mice,” *J. Cereb. Blood Flow Metab.*, vol. 36, no. 8, pp. 1351–1356, 2016.
[60] R. K. Wang, L. An, P. Francis, and D. J. Wilson, “Depth-resolved imaging of capillary networks in retina and choroid using ultrahigh sensitive optical microangiography,” *Opt. Lett.*, vol. 35, no. 9, p. 1467, May 2010.
[61] Z. Chu *et al.*, “Quantitative assessment of the retinal microvasculature using optical coherence tomography angiography,” *J. Biomed. Opt.*, vol. 21, no. 6, p. 66008, Jun. 2016.
[62] J. D. Briers, “Laser Doppler and time-varying speckle: a reconciliation,” *JOSA A, Vol. 13, Issue 2, pp. 345-350*, vol. 13, no. 2, pp. 345–350, Feb. 1996.
[63] U. Göbel, B. Klein, H. Schröck, and W. Kuschinsky, “Lack of Capillary Recruitment in the Brains of Awake Rats during Hypercapnia,” *J. Cereb. Blood Flow Metab.*, vol. 9, no. 4, pp. 491–499, Aug. 1989.
[64] R. F. Bonner and R. Nossal, “Principles of Laser-Doppler Flowmetry,” Springer, Boston, MA, 1990, pp. 17–45.
[65] D. Kleinfeld, P. P. Mitra, F. Helmchen, and W. Denk, “Fluctuations and stimulus-induced changes in blood flow observed in individual capillaries in layers 2 through 4 of rat neocortex,” *Proc. Natl. Acad. Sci.*, vol. 95, no. 26, pp. 15741–15746, 1998.
[66] E. Chaigneau, M. Oheim, E. Audinat, and S. Charpak, “Two-photon imaging of capillary blood flow in olfactory bulb glomeruli.,” *Proc. Natl. Acad. Sci. U. S. A.*, vol. 100, no. 22,

pp. 13081–6, 2003.
[67] D. Kleinfeld, “Cortical blood flow through individual capillaries in rat vibrissa S1 cortex: Stimulus-induced changes in flow are comparable to the underlying fluctuations in flow,” *Int. Congr. Ser.*, vol. 1235, no. C, pp. 115–122, 2002.
[68] P. J. Drew, A. Y. Shih, and D. Kleinfeld, “Fluctuating and sensory-induced vasodynamics in rodent cortex extend arteriole capacity,” *Proc. Natl. Acad. Sci.*, vol. 108, no. 20, pp. 8473–8478, 2011.
[69] B. Stefanovic *et al.*, “Functional Reactivity of Cerebral Capillaries,” *J. Cereb. Blood Flow Metab.*, vol. 28, no. 5, pp. 961–972, May 2008.
[70] W. J. Choi *et al.*, “Characterizing relationship between optical microangiography signals and capillary flow using microfluidic channels,” *Biomed. Opt. Express*, vol. 7, no. 7, p. 2709, Jul. 2016.
[71] M. Haugh, “Overview of Monte Carlo Simulation , Probability Review and Introduction to Matlab,” *Monte Carlo Simul.*, pp. 1–11, 2004.
[72] L. Entz *et al.*, “Evoked effective connectivity of the human neocortex.,” *Hum. Brain Mapp.*, vol. 35, no. 12, pp. 5736–53, Dec. 2014.
[73] T. Kunieda, Y. Yamao, T. Kikuchi, and R. Matsumoto, “New Approach for Exploring Cerebral Functional Connectivity: Review of Cortico-cortical Evoked Potential.,” *Neurol. Med. Chir. (Tokyo).*, vol. 55, no. 5, pp. 374–82, 2015.
[74] X. Liang, Q. Zou, Y. He, and Y. Yang, “Coupling of functional connectivity and regional cerebral blood flow reveals a physiological basis for network hubs of the human brain.,” *Proc. Natl. Acad. Sci. U. S. A.*, vol. 110, no. 5, pp. 1929–34, Jan. 2013.
[75] L. Vutskits and Z. Xie, “Lasting impact of general anaesthesia on the brain: mechanisms and relevance,” *Nat. Rev. Neurosci.*, vol. 17, no. 11, pp. 705–717, 2016.
[76] A. . Fallis, *Neurovascular Imaging*, vol. 53, no. 9. 2013.
[77] M. J. Cipolla, “Anatomy and Ultrastructure,” 2009.
[78] P. Blinder, A. Y. Shih, C. Rafie, and D. Kleinfeld, “Topological basis for the robust distribution of blood to rodent neocortex,” *Proc. Natl. Acad. Sci.*, vol. 107, no. 28, pp. 12670–12675, 2010.
[79] P. J. Drew *et al.*, “Chronic optical access through a polished and reinforced thinned skull,” *Nat. Methods*, vol. 7, no. 12, pp. 981–984, 2010.
[80] A. Y. Shih *et al.*, “The smallest stroke: occlusion of one penetrating vessel leads to infarction and a cognitive deficit,” *Nat. Neurosci.*, vol. 16, no. 1, pp. 55–63, 2012.
[81] P. W. Pires, W. F. Jackson, and A. M. Dorrance, “Regulation of myogenic tone and structure of parenchymal arterioles by hypertension and the mineralocorticoid receptor.,” *Am. J. Physiol. Heart Circ. Physiol.*, vol. 309, no. 1, pp. H127-36, Jul. 2015.
[82] R. Prakash, M. Johnson, S. C. Fagan, and A. Ergul, “Cerebral neovascularization and remodeling patterns in two different models of type 2 diabetes.,” *PLoS One*, vol. 8, no. 2, p. e56264, 2013.
[83] J. F. Poduslo *et al.*, “Targeting vascular amyloid in arterioles of Alzheimer disease transgenic mice with amyloid β protein antibody-coated nanoparticles.,” *J. Neuropathol. Exp. Neurol.*, vol. 70, no. 8, pp. 653–61, Aug. 2011.
[84] I. L. Joo *et al.*, “Early neurovascular dysfunction in a transgenic rat model of Alzheimer’s disease,” *Sci. Rep.*, vol. 7, 2017.
[85] A. Charidimou, L. Pantoni, and S. Love, “The concept of sporadic cerebral small vessel disease: A road map on key definitions and current concepts,” *Int. J. Stroke*, vol. 11, no. 1,

pp. 6–18, Jan. 2016.
[86] L. R. Caplan, “Lacunar infarction and small vessel disease: pathology and pathophysiology.,” *J. stroke*, vol. 17, no. 1, pp. 2–6, Jan. 2015.
[87] C. S. Bjornsson *et al.*, “Effects of insertion conditions on tissue strain and vascular damage during neuroprosthetic device insertion,” *J. Neural Eng.*, vol. 3, no. 3, pp. 196–207, Sep. 2006.
[88] D. Kleinfeld *et al.*, “Large-Scale Automated Histology in the Pursuit of Connectomes,” *J. Neurosci.*, vol. 31, no. 45, pp. 16125–16138, 2011.
[89] P. Blinder, P. S. Tsai, J. P. Kaufhold, P. M. Knutsen, H. Suhl, and D. Kleinfeld, “The cortical angiome: an interconnected vascular network with noncolumnar patterns of blood flow,” *Nat. Neurosci.*, vol. 16, no. 7, pp. 889–897, 2013.
[90] D. L. Adams, V. Piserchia, J. R. Economides, and J. C. Horton, “Vascular Supply of the Cerebral Cortex is Specialized for Cell Layers but Not Columns.,” *Cereb. Cortex*, vol. 25, no. 10, pp. 3673–81, Oct. 2015.
[91] J. Wu *et al.*, “Direct 3D Analyses Reveal Barrel-Specific Vascular Distribution and Cross-Barrel Branching in the Mouse Barrel Cortex,” *Cereb. Cortex*, vol. 26, no. 1, pp. 23–31, 2016.
[92] A. Li *et al.*, “Micro-optical sectioning tomography to obtain a high-resolution atlas of the mouse brain.,” *Science*, vol. 330, no. 6009, pp. 1404–8, Dec. 2010.
[93] Y. Chen and B. Kateb, *Neurophotonics and Brain Mapping*. CRC Press, 2017.
[94] H. Bridge and S. Clare, “High-resolution MRI: in vivo histology?,” *Philos. Trans. R. Soc. Lond. B. Biol. Sci.*, vol. 361, no. 1465, pp. 137–46, Jan. 2006.
[95] A. Deistung, A. Schäfer, F. Schweser, U. Biedermann, R. Turner, and J. R. Reichenbach, “Toward in vivo histology: A comparison of quantitative susceptibility mapping (QSM) with magnitude-, phase-, and R2*-imaging at ultra-high magnetic field strength,” *Neuroimage*, vol. 65, pp. 299–314, Jan. 2013.
[96] X. Yu *et al.*, “Sensory and optogenetically driven single-vessel fMRI,” *Nat. Methods*, vol. 13, no. 4, pp. 337–340, 2016.
[97] P. J. Bolan, E. Yacoub, M. Garwood, K. Ugurbil, and N. Harel, “In vivo micro-MRI of intracortical neurovasculature,” *Neuroimage*, vol. 32, no. 1, pp. 62–69, 2006.
[98] L. Gagnon, A. F. Smith, D. A. Boas, A. Devor, T. W. Secomb, and S. Sakadžić, “Modeling of Cerebral Oxygen Transport Based on In vivo Microscopic Imaging of Microvascular Network Structure, Blood Flow, and Oxygenation,” *Front. Comput. Neurosci.*, vol. 10, no. August, 2016.
[99] T. P. Santisakultarm *et al.*, “In vivo two-photon excited fluorescence microscopy reveals cardiac- and respiration-dependent pulsatile blood flow in cortical blood vessels in mice,” *AJP Hear. Circ. Physiol.*, vol. 302, no. 7, pp. H1367–H1377, 2012.
[100] L. Wang, W. Xu, M. Bachman, G. P. Li, and Z. Chen, “Phase-resolved optical doppler tomography for imaging flow dynamics in microfluidic channels,” *Appl. Phys. Lett.*, vol. 85, no. 10, pp. 1855–1857, 2004.
[101] L. Gagnon *et al.*, “Multimodal reconstruction of microvascular-flow distributions using combined two-photon microscopy and Doppler optical coherence tomography,” *Neurophotonics*, vol. 2, no. 1, p. 15008, 2015.
[102] R. K. Wang and Z. Ma, “Real-time flow imaging by removing texture pattern artifacts in spectral-domain optical Doppler tomography.,” *Opt. Lett.*, vol. 31, no. 20, pp. 3001–3003, 2006.

[103] B. J. Vakoc, S. H. Yun, J. F. de Boer, G. J. Tearney, and B. E. Bouma, "Phase-resolved optical frequency domain imaging," *Opt. Express*, vol. 13, no. 14, p. 5483, Jul. 2005.
[104] R. K. Wang and L. An, "Doppler optical micro-angiography for volumetric imaging of vascular perfusion in vivo," *Opt. Express*, vol. 17, no. 11, p. 8926, May 2009.
[105] G. Liu, A. J. Lin, B. J. Tromberg, and Z. Chen, "A comparison of Doppler optical coherence tomography methods.," *Biomed. Opt. Express*, vol. 3, no. 10, pp. 2669–80, Oct. 2012.
[106] L. Shi, J. Qin, R. Reif, and R. K. Wang, "Wide velocity range Doppler optical microangiography using optimized step-scanning protocol with phase variance mask.," *J. Biomed. Opt.*, vol. 18, no. 10, p. 106015, 2013.
[107] A. Bouwens, D. Szlag, M. Szkulmowski, T. Bolmont, M. Wojtkowski, and T. Lasser, "Quantitative lateral and axial flow imaging with optical coherence microscopy and tomography," *Opt. Express*, vol. 21, no. 15, p. 17711, Jul. 2013.
[108] Y. Nishijima *et al.*, "Impaired Collateral Flow Compensation During Chronic Cerebral Hypoperfusion in the Type 2 Diabetic Mice," *Stroke*, vol. 47, no. 12, p. 3014 LP-3021, Dec. 2016.
[109] A. Zhang, Q. Zhang, and R. K. Wang, "Minimizing projection artifacts for accurate presentation of choroidal neovascularization in OCT micro-angiography," *Biomed. Opt. Express*, vol. 6, no. 10, pp. 369–380, 2015.
[110] Y. Wang *et al.*, "A comprehensive analysis of gait impairment after experimental stroke and the therapeutic effect of environmental enrichment in rats," *J. Cereb. Blood Flow Metab.*, vol. 2882, 2008.
[111] W. Wei, W. J. Choi, and R. K. Wang, "Microvascular imaging and monitoring of human oral cavity lesions in vivo by swept-source OCT-based angiography," *Lasers Med. Sci.*, vol. 33, no. 1, pp. 123–134, Jan. 2018.
[112] C. Iadecola, "Neurovascular regulation in the normal brain and in Alzheimer's disease," *Nat. Rev. Neurosci.*, vol. 5, no. 5, pp. 347–360, May 2004.
[113] D. W. Wei, A. J. Deegan, and R. K. Wang, "Automatic motion correction for *in vivo* human skin optical coherence tomography angiography through combined rigid and nonrigid registration," *J. Biomed. Opt.*, vol. 22, no. 6, p. 66013, 2017.
[114] J. You, A. Li, C. Du, and Y. Pan, "Volumetric Doppler angle correction for ultrahigh-resolution optical coherence Doppler tomography.," *Appl. Phys. Lett.*, vol. 110, no. 1, p. 11102, Jan. 2017.
[115] T. D. Y. Kozai *et al.*, "Reduction of neurovascular damage resulting from microelectrode insertion into the cerebral cortex using in vivo two-photon mapping," *J. Neural Eng*, vol. 7, pp. 46011–12, 2010.
[116] D. A. Greenberg and K. Jin, "From angiogenesis to neuropathology," 2005.
[117] R. F. Gariano and T. W. Gardner, "Retinal angiogenesis in development and disease," 2005.
[118] B. J. Vakoc *et al.*, "Three-dimensional microscopy of the tumor microenvironment in vivo using optical frequency domain imaging," *Nat. Med.*, vol. 15, no. 10, pp. 1219–1223, Oct. 2009.
[119] A. F. Fercher, W. Drexler, C. K. Hitzenberger, and T. Lasser, "Optical coherence tomography - principles and applications," *Reports Prog. Phys.*, vol. 66, no. 2, pp. 239–303, Feb. 2003.
[120] Y. Jia *et al.*, "Quantitative optical coherence tomography angiography of vascular abnormalities in the living human eye."

[121] W. Wei, Y. Li, Z. Xie, A. Deegan, and R. K. Wang, "Spatial and temporal heterogeneities of capillary hemodynamics and its functional coupling during neural activation," *IEEE Trans. Med. Imaging*, pp. 1–1, 2018.
[122] S. Yousefi, T. Liu, and R. K. Wang, "Segmentation and quantification of blood vessels for OCT-based micro-angiograms using hybrid shape/intensity compounding," *Microvasc. Res.*, vol. 97, pp. 37–46, Jan. 2015.
[123] D. Goldenberg, U. Soiberman, A. Loewenstein, and M. Goldstein, "Heidelberg spectral-domain optical coherence tomographic findings in retinal artery macroaneurysm," *Retina*, vol. 32, no. 5, pp. 990–995, 2012.
[124] T. Luo, T. J. Gast, T. J. Vermeer, and S. A. Burns, "Retinal Vascular Branching in Healthy and Diabetic Subjects," *Investig. Opthalmology Vis. Sci.*, vol. 58, no. 5, p. 2685, May 2017.
[125] Y. Li *et al.*, "Aging-associated changes in cerebral vasculature and blood flow as determined by quantitative optical coherence tomography angiography," *Neurobiol. Aging*, vol. 70, pp. 148–159, 2018.
[126] H. C. Han, "Twisted blood vessels: Symptoms, etiology and biomechanical mechanisms," *Journal of Vascular Research*, vol. 49, no. 3. pp. 185–197, 2012.
[127] E. Bullitt *et al.*, "Vessel Tortuosity and Brain Tumor Malignancy: A Blinded Study."
[128] G. M. Hutchins, M. M. Miner, and J. K. Boitnott, "Vessel caliber and branch-angle of human coronary artery branch-points," *Circ Res*, vol. 38, no. 6, pp. 572–576, 1976.
[129] M. Pilch *et al.*, "Automated segmentation of retinal blood vessels in spectral domain optical coherence tomography scans.," *Biomed. Opt. Express*, vol. 3, no. 7, pp. 1478–91, 2012.
[130] L. Duan *et al.*, "Automated segmentation and characterization of choroidal vessels in high-penetration optical coherence tomography," *Ophthalmol. Vis. Sci. Prog. Retin. Eye Res. Arch. Ophthalmol. Ophthalmol. Rep. Prog. Phys. J. Ophthalmol. R. Margolis R. F. Spaide Ophthalmol. Vis. Sci. Retin.*, vol. 100, no. 13, pp. 3117–3123, 2960.
[131] C. D. Murray, "The physiological principle of minimum work applied to the angle of branching of arteries," *J. Gen. Physiol.*, vol. 9, no. 6, pp. 835–841, 1926.
[132] B. A. Sather, D. Hageman, and J. E. Wagenseil, "Murray's Law in Elastin Haploinsufficient (*Eln*+/−) and Wild-Type (WT) Mice," *J. Biomech. Eng.*, vol. 134, no. 12, p. 124504, 2012.
[133] S. Rossitti and J. Jjfgren, "Vascular Dimensions of the Cerebral Arteries Follow the Principle of Minimum Work," pp. 371–377.
[134] Y. Zheng *et al.*, "In vitro microvessels for the study of angiogenesis and thrombosis," *Proc. Natl. Acad. Sci.*, vol. 109, no. 24, pp. 9342–9347, Jun. 2012.
[135] S. G. Rayner *et al.*, "Reconstructing the Human Renal Vascular-Tubular Unit In Vitro," *Adv. Healthc. Mater.*, vol. 7, no. 23, p. 1801120, Dec. 2018.
[136] W. Wei, Y. Li, A. J. Deegan, and R. K. Wang, "Mapping and Quantitating Penetrating Vessels in Cortical Brain Using Eigen-Decomposition of OCT Signals and Subsequent Principal Component Analysis," *IEEE J. Sel. Top. Quantum Electron.*, vol. 25, no. 1, pp. 1–9, Jan. 2019.
[137] P. Hart, N. Nilsson, and B. Raphael, "A Formal Basis for the Heuristic Determination of Minimum Cost Paths," *IEEE Trans. Syst. Sci. Cybern.*, vol. 4, no. 2, pp. 100–107, 1968.
[138] P. Chiewvit, S. Piyapittayanan, and N. Poungvarin, "Cerebral venous thrombosis: diagnosis dilemma.," *Neurol. Int.*, vol. 3, no. 3, p. e13, Nov. 2011.
[139] A. N. Pavlov *et al.*, "Multiresolution analysis of pathological changes in cerebral venous dynamics in newborn mice with intracranial hemorrhage: adrenorelated vasorelaxation,"

Physiol. Meas., vol. 35, no. 10, pp. 1983–1999, Oct. 2014.
[140] H. N. Mayrovitz and J. Roy, "Microvascular blood flow: evidence indicating a cubic dependence on arteriolar diameter.," *Am. J. Physiol.*, vol. 245, no. 6, pp. H1031-8, Dec. 1983.
[141] M. Kobari, F. Gotoh, Y. Fukuuchi, K. Tanaka, N. Suzuki, and D. Uematsu, "Blood Flow Velocity in the Pial Arteries of Cats, with Particular Reference to the Vessel Diameter," *J. Cereb. Blood Flow Metab.*, vol. 4, no. 1, pp. 110–114, Mar. 1984.
[142] T. F. Sherman, "On connecting large vessels to small. The meaning of Murray's law.," *J. Gen. Physiol.*, vol. 78, no. 4, pp. 431–53, Oct. 1981.
[143] R. Reif, J. Qin, L. An, Z. Zhi, S. Dziennis, and R. Wang, "Quantifying optical microangiography images obtained from a spectral domain optical coherence tomography system," *Int. J. Biomed. Imaging*, vol. 2012, 2012.
[144] V. J. Srinivasan *et al.*, "Optical coherence microscopy for deep tissue imaging of the cerebral cortex with intrinsic contrast."
[145] M. Pircher and R. J. Zawadzki, "Review of adaptive optics OCT (AO-OCT): principles and applications for retinal imaging [Invited].," *Biomed. Opt. Express*, vol. 8, no. 5, pp. 2536–2562, May 2017.
[146] C. Apelian, F. Harms, O. Thouvenin, and A. C. Boccara, "Dynamic full field optical coherence tomography: subcellular metabolic contrast revealed in tissues by temporal analysis of interferometric signals."
[147] B. A. Boghigian, G. Seth, and B. A. Pfeifer, "Metabolic flux analysis and pharmaceutical production," *Metab. Eng.*, vol. 12, no. 2, pp. 81–95, Mar. 2010.
[148] D. J. Stephens and V. J. Allan, "Light microscopy techniques for live cell imaging," *Science*, vol. 300, no. 5616. American Association for the Advancement of Science, pp. 82–86, 04-Apr-2003.
[149] E. L. Elson, "Fluorescence Correlation Spectroscopy: Past, Present, Future," 2011.
[150] G. Popescu and Y. Park, "Optical imaging of cell mass and growth dynamics," ... *Physiol. ...*, vol. 2114, pp. 538–544, 2008.
[151] S. Huh, D. F. E. Ker, R. Bise, M. Chen, and T. Kanade, "Automated mitosis detection of stem cell populations in phase-contrast microscopy images," *IEEE Trans. Med. Imaging*, vol. 30, no. 3, pp. 586–596, 2011.
[152] C. Joo, T. Akkin, B. Cense, B. H. Park, and J. F. de Boer, "Spectral-domain optical coherence phase microscopy for quantitative phase-contrast imaging," *Opt. Lett.*, vol. 30, no. 16, pp. 2131–2133, 2005.
[153] P. H. Tomlins and R. K. Wang, "Theory, developments and applications of optical coherence tomography," *J. Phys. D. Appl. Phys.*, vol. 38, no. 15, pp. 2519–2535, 2005.
[154] A. L. Oldenburg, X. Yu, T. Gilliss, O. Alabi, R. M. Taylor, and M. A. Troester, "Inverse-power-law behavior of cellular motility reveals stromal–epithelial cell interactions in 3D co-culture by OCT fluctuation spectroscopy," *Optica*, vol. 2, no. 10, p. 877, 2015.
[155] Z. Zhi, W. Qin, J. Wang, W. Wei, and R. K. Wang, "4D optical coherence tomography-based micro-angiography achieved by 1.6-MHz FDML swept source."
[156] Y. Jia *et al.*, "Split-spectrum amplitude-decorrelation angiography with optical coherence tomography," *Opt. Express*, vol. 20, no. 4, pp. 4710–4725, 2012.
[157] E. Jonathan, J. Enfield, and M. J. Leahy, "Correlation mapping method for generating microcirculation morphology from optical coherence tomography (OCT) intensity images," *J Biophotonics*, vol. 4, no. 9, pp. 583–587, 2011.

[158] J. Lee, W. Wu, J. Y. Jiang, B. Zhu, and D. A. Boas, "Dynamic light scattering optical coherence tomography," *Opt. Express*, vol. 20, no. 20, p. 22262, Sep. 2012.
[159] J. Tang *et al.*, "Shear-induced diffusion of red blood cells measured with dynamic light scattering-optical coherence tomography," *J. Biophotonics*, no. July, p. e201700070, 2017.
[160] G. Farhat, A. Mariampillai, V. X. D. Yang, G. J. Czarnota, and M. C. Kolios, "Detecting apoptosis using dynamic light scattering with optical coherence tomography," *J. Biomed. Opt.*, vol. 16, no. 7, p. 70505, 2011.
[161] L. Thrane, S. Gu, B. J. Blackburn, K. V. Damodaran, A. M. Rollins, and M. W. Jenkins, "Complex decorrelation averaging in optical coherence tomography: a way to reduce the effect of multiple scattering and improve image contrast in a dynamic scattering medium," *Opt. Lett.*, vol. 42, no. 14, p. 2738, 2017.
[162] B. Blackburn *et al.*, "Noninvasive Assessment of Corneal Crosslinking with Phase-Decorrelation OCT," *Manuscr. Prep.*, vol. 60, no. 1, p. 41, Jan. 2018.
[163] W. Wei, Y. Li, A. J. Deegan, and R. K. Wang, "Mapping and quantitating penetrating vessels in cortical brain using Eigen-decomposition of OCT signals and subsequent principal component analysis," *IEEE J. Sel. Top. Quantum Electron.*, vol. 25, no. 1, pp. 1–1, 2018.
[164] R. L. Frederick and J. M. Shaw, "Moving Mitochondria: Establishing Distribution of an Essential Organelle," *Traffic*, vol. 8, no. 12, pp. 1668–1675, 2007.
[165] P. N. Pusey, "The dynamics of interacting Brownian particles," *J. Phys. A. Math. Gen.*, vol. 8, no. 9, pp. 1433–1440, 1975.
[166] J. M. Lee, M. C. Grabb, G. J. Zipfel, and D. W. Choi, "Brain tissue responses to ischemia," *Journal of Clinical Investigation*, vol. 106, no. 6. American Society for Clinical Investigation, pp. 723–731, Sep-2000.
[167] B. J. Blackburn, M. R. Ford, S. Gu, M. W. Jenkins, W. J. Dupps, and A. M. Rollins, "Monitoring corneal crosslinking with phase-decorrelation OCT (Conference Presentation)," in *Ophthalmic Technologies XXVIII*, 2018, vol. 10474, p. 23.
[168] W. Tan, A. L. Oldenburg, J. J. Norman, T. A. Desai, and S. A. Boppart, "Optical coherence tomography of cell dynamics in three-dimensional tissue models," *Opt. Express*, vol. 14, no. 16, p. 7159, 2006.
[169] C. H. D. L. Eroux, F. A. B. Ertillot, and O. L. T. Houvenin, "Intracellular dynamics measurements with full field optical coherence tomography suggest hindering effect of actomyosin contractility on organelle transport," vol. 7, no. 11, pp. 14057–14064, 2016.
[170] A. Li, J. You, C. Du, and Y. Pan, "Automated segmentation and quantification of OCT angiography for tracking angiogenesis progression," *Biomed. Opt. Express*, vol. 8, no. 12, p. 5604, Dec. 2017.